Diese Dissertation haben begutachtet:

[redacted] [redacted]

Prof. Dr. Nathal Severijns | Prof. Dr. Kai-Thomas Brinkmann

DISSERTATION

Investigation of Detector Related Systematic Effects for the RxB Spectrometer NoMoS

Ausgeführt zum Zwecke der Erlangung des akademischen Grades eines Doktors der technischen Wissenschaften unter Leitung von

Prof. Dr. Johann Marton
Atominstitut, TU Wien
Dr. Gertrud Konrad
Daily Supervisor
Atominstitut, TU Wien

eingereicht an der Technischen Universität Wien Fakultät für Physik von

Waleed Khalid
Matrikelnummer 11901918

Vienna, 25/08/2023 [redacted]

Ort, Datum | Unterschrift

In the loving memory of my Father

Abstract

The Standard Model of Particle Physics encompasses our current understanding of particle physics. However, due to its limitations, one of the goals of modern experimental physics is to probe the model further and look for physics beyond the Standard Model. One approach is to conduct precision physics experiments in free neutron beta decay. Precise measurements of the decay parameters from the decay provide a complementary approach to high energy searches. They can be used to validate the Standard Model and search for physics beyond it.

NoMoS is an $R \times B \not{v}$ momentum spectrometer designed for momentum spectroscopy of the charged decay products from the free neutron beta decay using a spatially resolving detector. As the spatially resolved detection of protons with high efficiency from the decay is quite challenging due to their small kinetic energies (<800 eV, 15 keV after post-acceleration), a novel silicon detector to detect low-penetrating particles (<5 µm) with spatial resolution, called the pLGAD, is introduced within this thesis. Furthermore, detailed studies of the detection system for NoMoS and the associated systematic uncertainties are studied within this work. Within that context, the previously unconsidered detection related systematic effect of channeling within the neutron beta decay community is also introduced and discussed in detail. Finally, recommendations are provided for the reduction of the systematic uncertainties arising from the detection system of the experiment to ensure that the final accuracy goal for the decay parameters of our interest can be achieved from the measured spectra.

Zussamenfassung

Das Standardmodell der Teilchenphysik umfasst unser derzeitiges Verständnis der Teilchenphysik. Aufgrund seiner Grenzen ist es jedoch ein Ziel der modernen experimentellen Physik, das Modell weiter zu erforschen und nach Physik jenseits des Standardmodells zu suchen. Ein Ansatz besteht darin, Präzisionsexperimente im freien Neutronen-Beta-Zerfall durchzuführen. Präzise Messungen der Zerfallseigenschaften liefern einen ergänzenden Ansatz zu Hochenergiesuchen. Sie können verwendet werden, um das Standardmodell zu validieren und nach Physik jenseits davon zu suchen.

NoMoS ist ein $R\not{\psi}\times B$-Impulsspektrometer, das für die Impulsspektroskopie der geladenen Zerfallsprodukte aus dem freien Neutronen-Betazerfall unter Verwendung eines räumlich auflösenden Detektors entwickelt wurde. Da die räumlich aufgelöste Detektion von Protonen mit hoher Effizienz aus dem Zerfall aufgrund ihrer geringen kinetischen Energien (<800 eV, 15 keV nach der Nachbeschleunigung) herausfordernd ist, wird in dieser Arbeit ein neuartiger Siliziumdetektor zur Detektion von schwach durchdringenden Partikeln (<5 µm) mit räumlicher Auflösung, namens pLGAD, vorgestellt. Darüber hinaus werden detaillierte Untersuchungen des Detektionssystems für NoMoS und der damit verbundenen systematischen Unsicherheiten in dieser Arbeit durchgeführt. Im Rahmen dessen wird auch der zuvor unbeachtete systematische Effekt der Kanalisierung innerhalb der Neutronen-Betazerfallgemeinschaft eingeführt und ausführlich diskutiert. Schließlich werden Empfehlungen zur Reduzierung der systematischen Unsicherheiten, die aus dem Detektionssystem des Experiments resultieren, gegeben, um sicherzustellen, dass das endgültige Genauigkeitsziel für die interessierenden Zerfallsparameter aus den gemessenen Spektren erreicht werden kann.

Contents

List of Acronyms

ALD Atomic Layer Deposition

APD Avalanche Photodiodes

BCA Binary Collision Algorithm

BSE Backscattered Electrons

BSM Beyond the Standard Model

CCE Charge Collection Efficiency

CKM Cabibbo–Kobayashi–Maskawa Matrix

DAQ Digital Acquisition

DEPFET Depleted p-channel Field Effect Transistor

DV Decay Volume

ECCI Electron Channeling Contrast Imaging

ENC Equivalent Noise Charge

ENF Excess Noise Factor

e-h-pairs Electron-hole Pairs

E×B $\vec{E} \times \vec{B}$ Drift

HLL Halbleiterlabor

IAEA International Atomic Energy Agency

IEL Ionization Energy Loss

ILL Institut Laue-Langevin

IMB-CNM-CSIC Institute of Microelectronics of Barcelona

IMSIL Implant and Sputter Simulator

IR Infrared

LHT Left Handed Tensor

LHS Left Handed Scalar

LGAD Low Gain Avalanche Diode

MCP Multichannel Plates

MD Molecular Dynamics

MIP Minimum Ionizing Particles

MPG-HLL Max Planck Halbleiterlabor

Nab The Neutron "a" and "b" experiment

NC Normal Conducting

NoMoS Neutron Momentum Decay Products Spectrometer (Apparatus)

PDG Particle Data Group

PCB Printed Circuit Board

pLGAD Proton Low Gain Avalanche Detector

PIN Positive Intrinsic Negative Diode

PMMA Polymethyl methacrylate

PMT Photo Multiplier Tubes

RHS Right Handed Scalar

RHT Right Handed Tensor

R×B $\vec{R} \times \vec{B}$ Drift

SC Superconducting

SEM Scanning Electron Microscope

SIMS Secondary Ion Mass Spectrometery

SBE Second Backscattered Electrons

SiPM Silicon Photomultipliers

SDD Silicon Drift Detector

SM The Standard Model of Physics

SNR Signal to Noise Ratio

SRIM Stopping Range of Ions in Matter

SUSY Super Symmetry

TCT Transient Charge Technique

TEM Tunneling Electron Microscope

TOF Time of Flight

TOF PET Time of Flight Position Emission Tomography

UHV Ultra High Vacuum

UV Ultraviolet

WF2 Weightfield 2

Chapter 1

Introduction

Our current best understanding of particle physics comes from the Standard Model (SM). The model describes three of the four fundamental forces of nature with the exclusion of gravity, and classifies all known particles in existence. It has successfully predicted the existence of previously unknown particles such as Higgs, W and Z Bosons, gluons, and top and charm quarks, along with their properties, most of which still hold under our modern and precise scrutiny. However, the SM is inherently an incomplete theory with its limitations. Apart from the obvious exclusion of gravity within its Lagrangian, it fails to explain the existence of neutrino mass, dark matter and energy, the CP problem, or the baryon asymmetry. Theories and extensions beyond the SM exist to explain these shortcomings through super symmetry (SUSY) or the existence of extra dimensions.

One of the major motivations behind modern experimental physics is to probe the SM further, in attempts to either find deviations from the model or to test the validity of these newer theories. Results obtained from these experiments apart from testing the models also provide new input for theorists to further streamline existing frameworks in attempts to provide solutions to long standing problems in physics. One interesting avenue in this regime is the study of the weak interaction. By precisely measuring its many observables through its decay products, it can provide an independent, and complementary alternative to test the limits of the SM further as well as search for physics Beyond the Standard Model (BSM).

An attractive candidate for the study of the weak interaction is the study of free neutron beta decay compared to the superallowed $0^+ \rightarrow 0^+$ decays or Pion decays. This is because experiments in neutron beta decay have relatively small errors and are not subject to theoretical nuclear structure corrections, which is the case for for the superallowed $0^+ \rightarrow 0^+$, and Pion decays respectively. A free neutron (n) decays as:

$$n\psi \xrightarrow{\tau_n} p^{+}\psi + e^{-}\psi + \bar{\nu}_e + Q\psi \tag{1.1}$$

with a neutron lifetime τ_n of 878.4(5) s and released energy [1]

$$Q = (m_n - m_p - m_e - m_\nu) \cdot c^2 = 782.332(46)\,\mathrm{keV}.$$

On the quark level, this decay entails the decay of a down quark to an up quark with the emission of a W boson. The W boson further decays into an electron and an anti-electron neutrino.

The decay rate of the neutron can be given by [2, 3]:

$$\begin{aligned} \mathrm{d}^3\Gamma &= \frac{1}{(2\pi)^5} \frac{G_F^2 |V_{ud}|^2}{5} p_e E_e (E_0 - E_e)^2 \mathrm{d}E_e \mathrm{d}\Omega_e \mathrm{d}\Omega_\nu \\ &\times \xi \left[\left(1 + a \frac{\mathbf{p}_e \cdot \mathbf{p}_\nu c^2}{E_e E_\nu} + b \frac{m_e}{E_e} + \frac{\langle \mathbf{s}_n \rangle}{s_n} \left(A \frac{\mathbf{p}_e c}{E_e} + B \frac{\mathbf{p}_\nu c}{E_\nu} + D \frac{\mathbf{p}_e \times \mathbf{p}_\nu c^2}{E_e E_\nu} \right) \right) \right] \end{aligned} \tag{1.2}$$

Here G_F is the Fermi weak coupling constant, V_{ud} is the first element of the CKM matrix, $\mathbf{p}_e$, $\mathbf{p}_\nu$, E_e, and E_ν are the momenta and total energies of the electron and the neutrino respectively, E_0 is the maximum energy of the electron, m_e the mass of the electron, $\mathbf{s}_n$ the spin of the neutron, Ω_i are the solid angles, and c is the speed of light. Lastly, ξ is proportional to the decay rate and contains the coupling constants (left and right handed scalar, tensor, axial, and vector couplings). a, A, B, and D are angular correlation coefficients in the neutron beta decay (for a better understanding, see Fig. 2.2), and b is the Fierz interference term. The electron-antineutrino coefficient a and the Fierz term b can be measured using unpolarized neutrons, whereas the rest of the angular correlation coefficients in Eq. (1.2) require a beam of polarized neutrons.

Currently, the Particle Data Group (PDG) states the CKM unitarity condition of the first row to have a 2.2σ discrepancy [1], however, depending on the theoretical calculations of the nuclear structure corrections to superallowed $0^+ \to 0^+$ decays this discrepancy can be much higher [4, 5, 6, 7, 8]. These deviations can be up to 4σ according to QCD Lattice calculations. While V_{ud} is generally determined from the average Ft-value of the $0^+ \to 0^+$ pure Fermi beta decays, free neutron beta decay is an attractive alternative as this is not subject to nuclear structure corrections. In free neutron beta decay, τ_n is inversely proportional to $|V_{ud}|^2(1+3\lambda^2)$ [9]. Therefore, one possibility of determining V_{ud} with the free neutron beta decay is to conduct an independent measurement of τ_n, and a, that is related to λ as

$$a = \frac{1 - |\lambda|^2}{1 + 3|\lambda|^2}. \tag{1.3}$$

Alternatively, the more prevalent approach of measuring the angular correlation coefficient A can also be utilized, however it requires precise knowledge of the neutron beam polarization. Furthermore, precise measurements of a will not only help answer questions regarding the CKM unitarity, but also shed some light within the field of cosmology by an accurate determination of λ[38]. Recently, the neutron decay spectrometer aSPECT [10] and aCORN experiment [11] have contributed to the world average of λ by the measurement of a (see Sec. 2.2.1), and in the future "The neutron 'a' and 'b' (Nab)" experiment aims to conduct more precise measurements of a with an ultimate goal of $\Delta a/a \approx 0.1\%$[12]. Measurements of a in this regime are a factor of 8 improvement over the current most precise measurement of a from aSPECT and provide an independent approach for the determination of λ from A with the same precision.

Currently free neutron beta decay is not competitive with the superallowed $0^+ \rightarrow 0^+$ decays due to the neutron lifetime puzzle (discussed further in Sec. 2.2.1) and the lack of precision in determination of λ.

Apart from the test of the CKM unitarity within the SM, the free neutron beta decay can be used to probe and provide limits on BSM couplings as well. The Fierz interference term b is an attractive candidate for this purpose, as it is sensitive to first order Left-Handed Scalar and Tensor couplings [13], and has a value of 0 within the SM. The Fierz interference term can be given as:

$$b \approx 2\frac{L_S + 3\lambda L_T}{1 + 3\lambda^2}, \tag{1.4}$$

where L_S, and L_T are the scalar and tensor coupling coefficients respectively.

The Neutron decay prOducts Momentum Spectrometer (NoMoS) plans to use a spatially resolving detector to measure the drift spectrum of the charged decay particles in neutron beta decay by having the particles experience an additional drift proportional to their momentum and the curvature of the magnetic field. This so called $R \times B$ drift is also why NoMoS is referred to as an $R \times B$ spectrometer [19]. The primary goals of NoMoS is to measure the electron-antineutrino correlation coefficient a by the measurement of the proton drift spectrum, and the Fierz Interference term b by the measurement of the electron drift spectrum from the decay of unpolarized neutrons. The experimental concept aims to have an accuracy of $\Delta a/a \leq 1\%$ and $\Delta b \leq 6 \times 10^{-3}$ in the short term, and in the longer term an ultimate accuracy of $\Delta a/a < 0.3\%$ and $\Delta b < 10^{-3}$. The experiment also aims to determine additional parameters such as weak magnetism form factor κ, once it has achieved its ultimate accuracy.

As NoMoS is a precision physics experiment, all systematic effects along with their uncertainties need to be well understood for the experiment to achieve its accuracy goal. Therefore, this thesis deals with an in depth study of the detector-related systematic effects and their associated uncertainties present within the experiment. Consequently, recommendations to help minimize the systematic error budget of the experiment from the detection side are provided. Furthermore, a new detector technology specifically designed for low-penetrating particles (that only penetrate silicon < 5 µm) called the proton Low Gain Avalanche Detector (pLGAD) is introduced, which has subsequently been patented [20]. The thesis also introduces a new detector-related systematic effect called "channeling", which has generally been ignored within Neutron beta decay experiments up till now.

The thesis is structured as follows: Chapter 2 starts with the theory and motivation behind the experiment as well as information of state of the art measurements. It also provides a basic foundation behind the physics of the experiment and the simulation methods used to investigate various systematic effects. Chapter 3 formally introduces the NoMoS experiment. It goes on to provide preliminary investigations and recommendations for the secondary detection systems for the experiment apart from the main drift detector. Chapter 4 goes into detail about the main drift detector for NoMoS, and introduces the pLGAD. It also provides a first proof of principle obtained from Transient Current Technique (TCT) measurements of the prototypes of the pLGAD. Chapter 5 continues the discussion of pLGAD and provides a simulation based efficiency for the detection technology within NoMoS after introduction and an in-depth investigation of channeling effects. Chapter 6 reintroduces the so called Transfer Function, which is an analytic description of NoMoS to be used for fitting the drift energy spectrum and has been used here as a tool to investigate the magnitude of the systematic effects and their uncertainties on the observables a and b within NoMoS. Using the transfer function, an in-depth investigation of detector-related systematic effects is presented. The chapter concludes with recommendations on the tolerances and accuracies required for different detector-related aspects of the experiment in order to reach its ultimate accuracy goal. Finally, the thesis concludes with Chapter 7, where a summary of my investigations is provided alongside a list for other minor detection related systematic effects, which still need to be incorporated within the Transfer Function and subsequently investigated in more detail. The list also details further steps required to ensure that NoMoS is able to reach its final accuracy goal such as the inclusion of the final electrode design, and optimization of the superconducting setup of NoMoS.

Chapter 2

Theoretical Background

The neutron beta decay is well described within the framework of the Standard Model (SM) of elementary particle physics. The process of a neutral particle consisting of two down and one up quark decaying by the emission of a virtual W boson, which further decays into an electron and anti-electron neutrino has been studied and modelled in detail, both theoretically and experimentally, over the past few decades.

Neutron Momentum Decay Products Spectrometer (NoMoS) is an experimental concept which plans to partake in both the searches for BSM physics as well as probe the SM by the determination of the Fierz interference term b from the electron momentum spectrum and the Electron-antielectron neutrino correlation coefficient a from the proton momentum spectrum. a can be used to determine λ which, when combined with independent measurements of the neutron lifetime τ_n can be used to determine V_{ud} and help check the unitarity of the first row of the CKM matrix. Alternatively, b can be used to look for physics beyond the Standard model as it contains Left-handed Scalar and Tensor couplings within the neutron beta decay. These physics motivations are discussed in detail in Sec. 2.1.1, and Sec. 2.2. Sec. 2.2 also provides the current status of the decay parameters a and b in order to compare the final planned accuracy of NoMoS with the state of the art. For details regarding the other correlation coefficient parameters it is recommended to refer to standard textbooks [21, 22] or a review [23, 24].

Furthermore, this chapter also discusses the physics concepts behind the experiment, such as the motion of charged decay particles in electromagnetic fields, and the $R \times B$ drift effect, which the experiment plans to utilize to measure a drift distance spectrum of electrons and protons from the decay momentum spectrum of the two charged particles. Lastly, the simulation algorithms utilized within the context of this thesis are also briefly introduced in Sec. 2.4.

2.1 Free Neutron Beta Decay

The process of free neutron beta decay, in which a neutron decays into a proton, and a $W\not\psi$ boson which further decays into an electron and electron antineutrino ($d\not\psi\mapsto ue^{-}\bar{\nu}_e$), is well defined in the V-A model [25]. This purely left-handed, weak interaction within the Standard Model (SM) can be used to determine the CKM matrix element V_{ud} through increasingly precise measurements of the neutron lifetime, with a current mean lifetime of $\tau_{\mathrm{n}} = 878.4 \pm 0.5$ [1], and a decay correlation coefficient. The CKM matrix is a unitary mixing matrix that shows the strength of quark flavour mixing within the weak interaction. As the CKM matrix is unitary by design, its unitarity can be probed to search for hints of physics beyond the Standard Model (BSM). The unitarity test of the first row of the matrix is given by:

$$|V_{ud}|^2 + |V_{us}|^2 + |V_{ub}|^2 = 1 \tag{2.1}$$

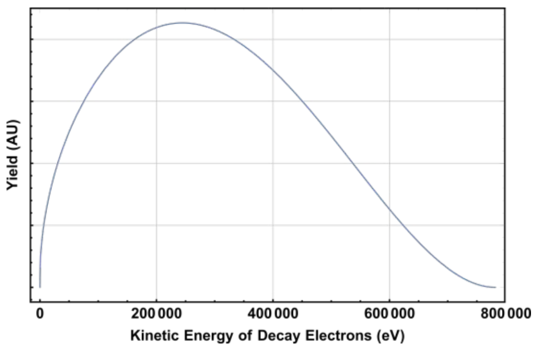

(a) Decay electrons

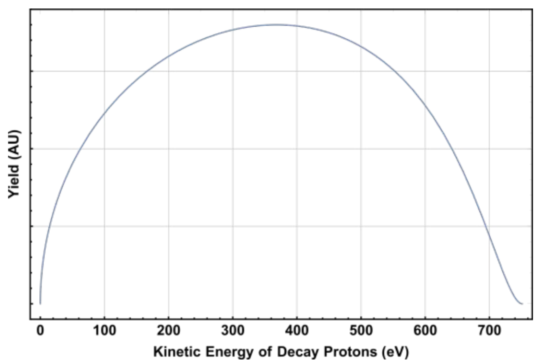

(b) Decay Protons

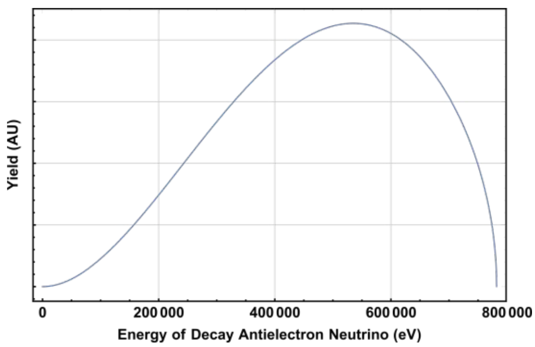

(c) Decay Antielectron Neutrino

Figure 2.1: The distribution of kinetic energy of decay particles emanating from free neutron beta decay.

Due to the three body nature of the beta decay, the energy of the decaying particle is distributed among the decay particles where the kinematics of the decay process is governed by the physical properties of the particles. Figure 2.1 shows the kinetic energy distribution of the three decay particles, where the protons have the lowest energy due to their heavier mass compared to the electron, and the anti-electron neutrino.

2.1.1 Measurable Parameters in Neutron Beta Decay

Neutron beta decay has a myriad of decay parameters, which can be derived rather model independently by using Fermi's Golden Rule, as stated already in Eq. (1.2) (neutrino masses and spin of outgoing particles are neglected) [2, 3]:

$$\begin{aligned} \mathrm{d}^3\Gamma &= \frac{1}{(2\pi)^5}\frac{G_F^2|V_{ud}|^2}{2} p_e E_e (E_0 - E_e)^2 \mathrm{d}E_e \mathrm{d}\ {}_e \mathrm{d}\ {}_\nu \\ &\times \xi \left[\left(1 + a \frac{\mathbf{p}_e \cdot \mathbf{p}_\nu c^2}{E_e E_\nu} + b \frac{m_e}{E_e} + \frac{\langle \mathbf{s}_n \rangle}{s_n} \quad A \frac{\mathbf{p}_e c}{E_e} + B \frac{\mathbf{p}_\nu c}{E_\nu} + D \frac{\mathbf{p}_e \times \mathbf{p}_\nu c^2}{E_e E_\nu} \right) \right] \end{aligned} \tag{2.2}$$

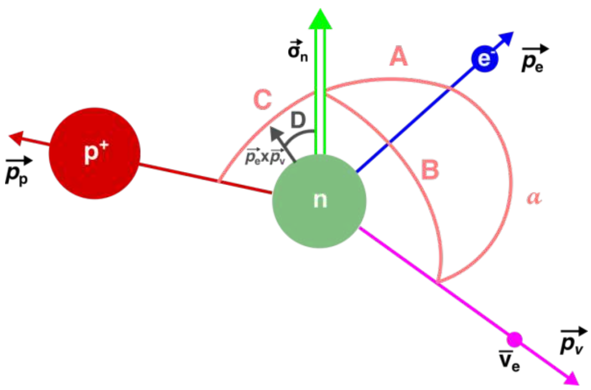

Figure 2.2: An illustrative view of the angular correlation coefficients of the decay products: a, A, B, C, and D, in the neutron beta decay drawn in relation to the neutron spin σ_n. Adapted from [26] and [27].

To better understand the angular correlation coefficients one can refer to Figure 2.2, which shows an illustration of the angular correlations. ξ is a factor that is reciprocally proportional to the neutron decay rate and its expression as well as that of the correlation coefficients in Eq. (2.2 is given as [28]:

$$\xi = |L_\mathrm{V}|^2 + 3|L_\mathrm{A}|^2 + |L_\mathrm{S}|^2 + 3|L_\mathrm{T}|^2 + |R_\mathrm{V}|^2 + 3|R_\mathrm{A}|^2 + |R_\mathrm{S}|^2 + 3|R_\mathrm{T}|^2 \tag{2.3a}$$

$$\xi a = |L_\mathrm{V}|^2 - |L_\mathrm{A}|^2 - |L_\mathrm{S}|^2 + |L_\mathrm{T}|^2 + |R_\mathrm{V}|^2 - |R_\mathrm{A}|^2 - |R_\mathrm{S}|^2 + |R_\mathrm{T}|^2 \tag{2.3b}$$

$$\xi b = 2\mathrm{Re}(L_\mathrm{S}L_\mathrm{V}^* + 3L_\mathrm{A}L_\mathrm{T}^* + R_\mathrm{S}R_\mathrm{V}^* + R_\mathrm{A}R_\mathrm{T}^*) \tag{2.3c}$$

$$\xi A = 2\mathrm{Re}(-|L_\mathrm{A}|^2 - L_\mathrm{V}L_\mathrm{A}^* + |L_\mathrm{T}|^2 + L_\mathrm{S}L_\mathrm{T}^* + |R_\mathrm{A}|^2 + R_\mathrm{V}R_\mathrm{A}^* - |R_\mathrm{T}|^2 - R_\mathrm{S}R_\mathrm{T}^*) \tag{2.3d}$$

$$B = B_0 + b_\nu \frac{m_e}{E_e}, \quad \text{with} \tag{2.3e}$$

$$\xi B_0 = 2\mathrm{Re}(|L_\mathrm{A}|^2 - L_\mathrm{V}L_\mathrm{A}^* + |L_\mathrm{T}|^2 - L_\mathrm{S}L_\mathrm{T}^* - |R_\mathrm{A}|^2 + R_\mathrm{V}R_\mathrm{A}^* - |R_\mathrm{T}|^2 + R_\mathrm{S}R_\mathrm{T}^*) \tag{2.3f}$$

$$\xi b_\nu = 2\mathrm{Re}(-L_\mathrm{S}L_\mathrm{A}^* - L_\mathrm{V}L_\mathrm{T}^* + 2L_\mathrm{A}L_\mathrm{T}^* + R_\mathrm{S}R_\mathrm{A}^* + R_\mathrm{V}R_\mathrm{T}^* - 2R_\mathrm{A}R_\mathrm{T}^*) \tag{2.3g}$$

$$\xi D = 2\mathrm{Im}(L_\mathrm{S}L_\mathrm{T}^* - L_\mathrm{V}L_\mathrm{A}^* + R_\mathrm{S}R_\mathrm{T}^* - R_\mathrm{V}R_\mathrm{A}^*), \tag{2.3h}$$

where b_ν is another Fierz-like parameter, similar to b, and both depend on the non-SM couplings in the first order compared to the other parameters. The notation of L_j and R_j is used the same as in Ref. [28], and represent the weak coupling constants for the participating V, A, S, T currents and are connected to the C_j and C'_j weak coupling constants in Ref. [29] as:

$$C_j = \frac{G_\mathrm{F}V_\mathrm{ud}}{2}(L_j + R_j), \; C'_j = \frac{G_\mathrm{F}V_\mathrm{ud}}{2}(L_j - R_j), \quad \text{for } j = \mathrm{V, A, S, T} \tag{2.4}$$

Furthermore, if the spin of the decay electrons is also considered, more correlation coefficients appear in the equation.

Angular Correlation Coefficients in the Standard Model

The neutron beta decay is a purely left-handed, V-A interaction within the confines of the SM. Therefore, the Fierz term $b = 0$ as there are no left handed scalar (S) and tensor (T) couplings within the SM. The rest of the angular correlation coefficients can be given by having them depend solely on $\lambda = L_A/L_V$, the ratio of the weak axial-vector to the vector coupling constant.

$$a = \frac{1-|\lambda|^2}{1+3|\lambda|^2} \tag{2.5a}$$

$$A = -2\frac{|\lambda|^2+|\lambda|\cos\phi}{1+3|\lambda|^2} \tag{2.5b}$$

$$B = 2\frac{|\lambda|^2-|\lambda|\cos\phi}{1+3|\lambda|^2} \tag{2.5c}$$

$$C = 4x_c\frac{|\lambda|\cos\phi}{1+3|\lambda|^2} \tag{2.5d}$$

$$D = 2\frac{|\lambda|\sin\phi}{1+3|\lambda|^2}, \tag{2.5e}$$

here C is the proton asymmetry relative to the neutron spin, ϕ is the phase angle between the weak axial-vector and vector coupling constants, and x_c is a kinematical factor. It should also be noted that if $\mathcal{T}$ time-reversal invariance is assumed, then $D = 0$.

For NoMoS, the correlation coefficient chosen for optimization purposes within the SM is the electron anti-neutrino correlation coefficient a. Measurement of this coefficient, along with independent measurements of τ_n, V_{us}, and V_{ub} (the last two being obtained from experiments performed with particles containing s and b quarks) can be used to test the SM by verifying the unitarity of the CKM matrix (using Eq. (2.1)) V_{ud}. If Eq. (2.2) is integrated over the solid angles and the electron energy, and the conservation of vector currents is assumed within the SM (i.e. L_V=1), then the following equation can be obtained [9]:

$$|V_{ud}|^2\tau_n(1+3L_A^2) = \text{const.}, \tag{2.6}$$

where the constant contains calculations from theory of radiative corrections.

To understand the dependence of the proton energy spectrum w_p on a, multiple approaches could be adopted. The simplest approach is the Nachtmann approximation of the proton energy spectrum [30],

$$w_p(T_p) \propto g_1(T_p) + a\, g_2(T_p) \tag{2.7}$$

where g_1 and g_2 are two proton kinetic energy T_p dependent functions. Alternatively, another approach is given by Glück [31] (or an improved one in [32]), in which the proton energy spectrum is described in terms of both a and b. For a first approximation for NoMoS, the Nachtmann approach is utilized in this work as I dealt with the study of the overall uncertainty introduced within the experiment by uncertainties in various detection-related systematic effects and not the final fitting routine for an accurate value of the decay correlation parameter. However, for the final data analysis of the experiment, it is recommended to use the more comprehensive approach by Glück as previously mentioned.

Figure 2.3 shows the influence of the electron-antielectron neutrino correlation coefficient a on the observable proton energy spectrum (see Eq. 2.7) from the free neutron beta decay along with the corresponding residual spectrum.

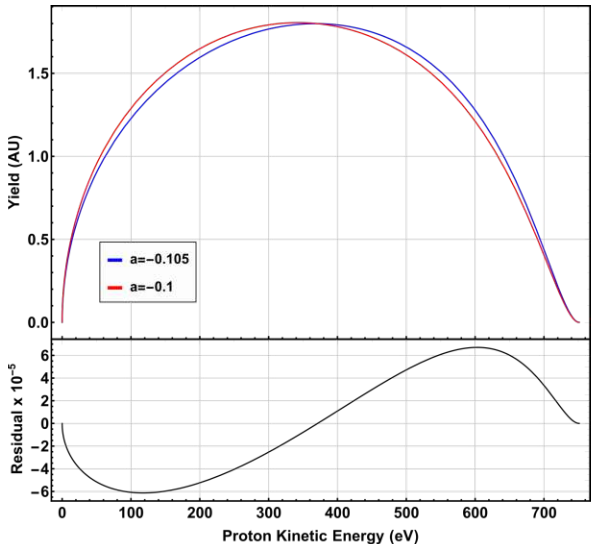

Figure 2.3: Influence of the Electron-Antielectron neutrino correlation coefficient a on the observable proton energy spectrum from free neutron beta decay. The black line shows the residuals between both spectra shown. The values of a are chosen to make the spectra distinguishable by eye.

2.1.2 Parameter Representation Beyond the Standard Model

The SM of particle physics has quite a few shortcomings, and consequently there are many proposed theories and extensions in attempts to address them [33, 34, 23]. One possible extension to the SM is the presence of Left-Handed Scalar and Tensor (LHS, and LHT) couplings. The presence of these hypothetical couplings within the neutron beta decay can be given linearly by the Fierz interference term b as [23]:

$$b \approx 2\frac{L_S + 3\lambda L_T}{1 + 3\lambda^2} \tag{2.8}$$

Where L_S, and L_T are the scalar and tensor coupling constants respectively.

As neutron beta decays are sensitive to the scalar and tensor couplings in the first order, they are more sensitive towards tensor currents, as can be seen from Eq. (2.8).

The Fierz interference term can be probed by observing the electron energy spectrum, where the electron energy spectrum is given, after the BSM modification by:

$$w_e(E_e) = \left(1 + b\frac{m_e}{E_e}\right)\left(\frac{(4\pi)^2}{(2\pi\hbar)^6} F(Z, E_e)\sqrt{E_e^2 - m_e^2}\, E_e (E_0 - E_e)^2 [1 + \delta_R(E_e)][1 + R_0(E_e)]\right) \tag{2.9}$$

where $F(Z, E_e)$ is the Columb correction by the Fermi function [35], $\delta_R(E_e)$ is the outer radiative correction [36], and $R_0(E_e)$ is the recoil correction [31, 35] (also see [26]). The influence of the Fierz interference term on the electron energy spectrum is shown in Fig. 2.4, where energy spectra of the electrons from free neutron beta decay are plotted for 2 different b values along with the corresponding residuals.

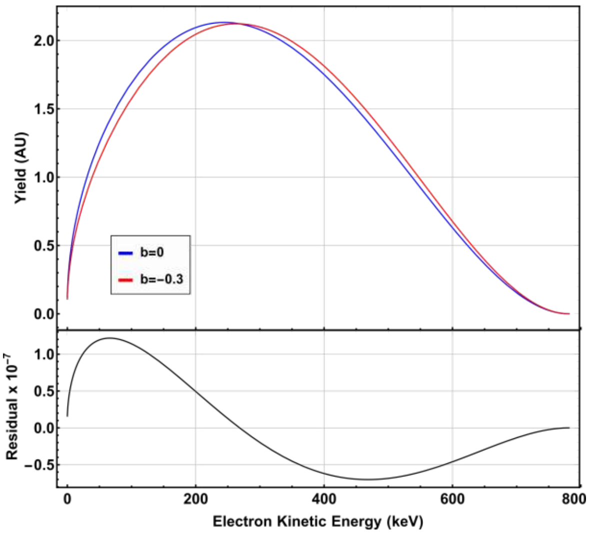

Figure 2.4: Influence of the Fierz Interference term b on the observable electron energy spectrum from free neutron beta decay. The black line shows the residuals between the shown spectrum. The values of b are chosen to make the spectra distinguishable by eye.

2.2 Physics Motivation and State of the Art

2.2.1 Standard Model Motivation

For the SM part, NoMoS intends to shed light on the CKM unitarity by determination of V_{ud}. Currently there is a $> 2\sigma$ discrepancy in the CKM unitarity of the first row, shown by various independent investigations [4, 5, 6, 7]. One possible explanation for the deviation may stem from the precise determination of V_{ud}, which is obtained from $0^+ \rightarrow 0^+$ nuclear decay experiments, where the majority of the uncertainty on the value comes from the theoretical nuclear structure corrections. The current determined value of V_{ud} according to PDG 2022 is [1]:

$$|V_{ud}| = 0.97373 \pm 0.00031.\psi \tag{2.10}$$

Alternative approaches to the superallowed $0^+ \rightarrow 0^+$ nuclear decays are, neutron beta decay, mirror decays, and pion decays. Out of all these, pion decays are the "cleanest" theoretically as they are pure vector transitions and have no nuclear structure corrections. However, the experimental uncertainties in the case of pion decays are quite high as it requires the precise measurement of a branching ratio of the order of 10^{-8}. Neutron beta decays on the other hand are not only "clean" as they do not have nuclear structure corrections, but also have significantly lower experimental uncertainties. Consequently, a value of V_{ud} to shed light on the CKM unitarity is alternatively obtained from nuclear beta decay, as shown in Eq. 2.6, by the measurement of the neutron lifetime τ_n and, the determination of the axial to vector coupling constants ratio λ.

Status of $\lambda\psi$

The value of $\lambda\psi$ within PDG2022 is:

$$\lambda\psi = -1.2754 \pm 0.0013,\psi \tag{2.11}$$

which is mostly determined from the measurements of $A\psi$ in neutron beta decay. Recently, there has been the addition of two $a\psi$ values within the world average, namely from aSPECT [10] and aCORN [11]. aSPECT measured $a\psi$ by the measurement of the proton energy spectrum utilizing energy cuts from an electrode, whereas aCORN utilized the "wishbone asymetry" by measuring the electron energy spectrum and the proton Time of Flight (TOF) looking for coincidence events. Currently, there is more than a $2\sigma\psi$ tension within the two values obtained from aSPECT and aCORN. It should be noted that a reanalysis of the aSPECT data is underway and the preliminary studies show that the value of $a\psi$ from aSPECT will change and the discrepancy will lessen [37]. The current average from PDG 2022 [1] is:

$$a\psi = -0.1049 \pm 0.0013 \tag{2.12}$$

Nonetheless, this does illustrate the importance of conducting further measurements of a. NoMoS aims to measure $a\psi$ by the measurement of the proton energy spectrum with an ultimate precision of $\Delta a/a\psi < \psi 0.3\%$.

Neutron Lifetime

The discrepancy in the experimentally determined neutron lifetime has been a long standing puzzle within physics. It stems from the two different techniques used to measure the lifetime. The bottle experiments measure the lifetime of neutrons by trapping ultracold neutrons within a vessel using magnetic or material traps, and counting the surviving neutrons after set time intervals [39, 40]. Whereas the beam experiments count the charged decay products from neutron beta decay [41, 42] that decay from a beam of neutrons passing through a decay volume. Currently the two methods have a discrepancy of more than 8 seconds, which corresponds to a difference of $\approx 4\sigma$.

There are multiple possible explanations for this discrepancy, which range from experimental errors to exotic decays, such as [43, 44, 45, 46] to name just a few.

Multiple experiments are underway in attempts to explain this discrepancy, with the most recent results being from UCNτ [47] for the bottle and JPARC [41] for the beam experiments. Similarly, there are other experiments which are working on the determination of the lifetime e.g. see [48, 49].

2.2.2 Beyond the Standard Model Motivation

As explained in Sec. 2.1.2, neutron beta decays can be sensitive to LHS and LHT couplings in BSM models with the introduction of a non-vanishing Fierz interference term b.

Currently, the best and only limits on b are provided by the Perkeo III and the UCNA experiments, both of which provide a limit on b from a measurement of the beta asymmetry spectrum $A(\mathrm{E}_e)$ in polarized neutron decay. The value of b provided by Perkeo III is $b = 0.017(21)$, whereas it is $b = 0.066(65)$ from the UCNA experiment [14], both of which are consistent with the SM assumption of $b = 0$. Furthermore, the aSPECT collaboration will also publish newer constraints on the Fierz Interference term, with preliminary results also being consistent with 0 [37]. However, more accurate measurements of b will provide tighter constraints on L_S, and L_T [23]. NoMoS intends to measure b with an ultimate accuracy of $\Delta b \lesssim 10^{-3}$ by the measurement of the electron energy spectrum.

It should be mentioned that the Nab collaboration [12] in the USA also aims to reach a similar accuracy by measuring the electron energy and the proton time of flight from unpolarized neutron beta decay to determine a and b. Whereas other experiments such as the abBA experiment [50] and PERC [18] plan to improve the accuracy of a and b even further. Constraints on the scalar and tensor coupling constants from neutron beta decay are competitive to those from high energy searches at the LHC [23].

Within the context of this work, we will often refer to the Fierz Interference term

b and the Electron-Antielectron Neutrino Correlation Coefficient a as the observables in lieu of the electron and proton drift spectrum, which is what will be observed in the actual experiment, for ease.

2.3 Motion of Charged Particles in Electromagnetic Fields

As NoMoS intends to use the so called $R \times B$ principle to conduct its measurements, in this section some of the basic principles of how charged particles interact with electromagnetic fields will be discussed.

2.3.1 Adiabatic Invariance

Suppose there is a dynamical system described by a Hamiltonion $H(\mathbf{q}, \mathbf{p}, \lambda)$, where $\mathbf{q}$ are generalized coordinates, $\mathbf{p}$ denotes the canonically conjugate momenta of $\mathbf{q}$, and $\lambda = \lambda(t)$ are the system's parameters. If the timescale of changes in λ are much greater than the oscillation period of the system, then the action integrals J_i

$$J_i(E, \lambda) = J_i(E(t), \lambda(t)) = \oint p_i \mathrm{d}q_i, \qquad i = 1, 2, 3, \tag{2.13}$$

are the adiabatic invariants of the system, where the integrals are evaluated for a total Energy E and λ [51].

For a charged particle passing through an electromagnetic field, an example of an adiabatic invariant quantity is its magnetic moment μ

$$\mu = \frac{T_\perp}{B}, \tag{2.14}$$

provided the change in electromagnetic field is small over a period of the particle's gyration, i.e. $\Delta E/E \ll 1$ and $\Delta B/B \ll 1$.

2.3.2 Motion of Charged Particles in Magnetic Fields

A charged particle in motion interacts with an electromagnetic field under the influence of the Lorentz force [51]:

$$\vec{F_L} = q(\vec{E} + \vec{v} \times \vec{B}), \tag{2.15}$$

where q is the charge of the particle, $\vec{v}$ is the velocity, $\vec{E}$ the electric field, and $\vec{B}$ the magnetic flux density (which will be referred to as the magnetic field).

In the absence of an electric field, this force is reduced to a simple cross product where the charged particle performs a helical motion along a magnetic field line. The helical movement can be broken down into a transversal and a perpendicular component relative to the magnetic field. The transversal velocity remains unaltered and defines the motion of the "gyration center" of the particle. The perpendicular part is responsible for the gyration of the particle around its gyration center. The gyration radius r_G is given by:

$$r_G = \frac{p \sin\theta}{qB}, \tag{2.16}$$

where p is the relativistic momentum, and θ is the pitch angle. For the case of NoMoS's superconducting setup, with a magnetic field of 0.976 T and a maximum angle of 45° within the main spectrometer region, referred to as the $R \times B$ region, the maximum gyration radii of both the electrons and protons, corresponding to the maximum momentum of the particles $r_{G,max}$ will be:

$$r_{G,\mathrm{max}} \approx 2.9\,\mathrm{mm} \tag{2.17}$$

The frequency ω_G with which a particle performs its gyrations and pitch h are consequently given by [51]

$$\omega_G = \frac{qB}{m} \tag{2.18a}$$

$$h = \frac{2\pi p}{B} \cos\theta \tag{2.18b}$$

Where is the relativistic factor and m is the particle's mass.

Magnetic Mirror Effect

Supposing an adiabatic change of magnetic field, Eq. (2.16) along with the conservation of the magnetic flux (as there are no monopoles within the SM), the change of the local pitch angle θ due to a change in the magnetic field can be given by [51]:

$$\frac{\sin^2\theta_0}{\sin^2\theta_1} = \frac{B_0}{B_1}. \tag{2.19}$$

This relation leads to the conclusion that an increase in the magnetic field will lead to an increase of the pitch angle until the magnetic field simply reflects a particle. This is known as the magnetic mirror effect. This effect therefore can be used to design filter coils in order to prevent particles with an angle greater than the desired angle θ from passing through.

2.3.3 Motion of Charged Particles in Curved Magnetic Fields

When a particle enters a circularly curved magnetic field, it experiences an additional drift perpendicular to the curvature radius $\vec{R}$ and the magnetic field $\vec{B}$. The drift velocity in the first order of this additional drift can be expressed as [51, 52]:

$$\vec{v}_{R\times B} = \frac{mv^2\cos\theta}{qRB}f(\theta)\frac{\vec{R}\times\vec{B}}{RB} + \frac{m}{qB^2}\left(\dot{\vec{v}}_{R\times B}\times\vec{B}\right), \tag{2.20}$$

Where R and B are norms of their respective quantities, and $f(\theta)$ is an angle-dependent factor given by:

$$f(\theta) = \frac{1}{2}\left(\cos\theta + \frac{1}{\cos\theta}\right). \tag{2.21}$$

Eq. (2.20) can be integrated over a time period T to obtain the drift distance D, assuming a uniformly curved magnetic field and all other quantities being constant with respect to T:

$$D_x^{1st} = \frac{pv_{\parallel}T}{qRB}f(\theta), \qquad D_{y,z}^{1st} = 0. \tag{2.22}$$

Eq. (2.22) can alternatively be written as:

$$D_x^{1st} = \frac{p\alpha}{qB}f(\theta), \tag{2.23}$$

where is the curvature angle the particle went over in the time period T, given by:

$$= v_{\parallel}\frac{T}{R}. \tag{2.24}$$

Therefore, by using Eq. (2.22), the momenta of charged particles p can be mapped spatially on a detector, where the particles will experience a drift based on the curvature angle , the strength of the magnetic field B, their pitch angle θ and their charge q (electrons and protons will experience drifts in opposite directions).

For the purpose of NoMoS, we will confine ourselves to the first order terms as the second order drift is already suppressed to 10^{-4} level, which is an order of magnitude lower than the desired precision of the experiment.

2.3.4 Drift of Charged Particles in Electromagnetic Fields

As explained earlier, the motion of a charged particle within an electromagneitc field is governed by the Lorentz force (see Eq. 2.15). A charged particle will therefore experience an additional acceleration or deceleration in the direction of $\vec{E}$ on top of the helical motion within an electromagnetic field. Within the adiabatic invariance limit the parallel to B kinetic energy component $T_{\parallel}^{ad}(z)$ is given as:

$$T_{\parallel}^{ad}(z) = T_0 - q(U(z) - U_0) - \frac{B(z)}{B_0}T_0\sin^2\theta_0, \tag{2.25}$$

where T_0 is the initial kinetic energy of the particle, $U\psi$is the electric potential at a specific point z, U_0 is the initial electric potential, and $B(z)$ is the magnetic field at a point z. The local pitch angle change can then be given as [26]:

$$\sin^2\theta(z) = \frac{B(z)}{B_0}\frac{T_0\sin^2\theta_0}{T_0 - q(U(z) - U_0)}.\psi \tag{2.26}$$

Therefore a particle will experience a decrease in their local pitch angle dependent on $B(z)$ as they are accelerated within a magnetic field $\vec{B}\psi$with the help of an electric field $\vec{E}$. This is an important relation for the calculation of the pitch angle of protons at the drift detector within NoMoS.

The particles can experience additional drifts within an electromagnetic field if the electric field $\vec{E}\psi$is not aligned parallel to the magnetic field $\vec{B}$. This effect introduces an additional so-called $E\psi\times B\psi$drift on the particle, that is given by [51]:

$$\vec{v}_{E\times B} = c\frac{\vec{E}\psi\times\vec{B}\psi}{B^2}.\psi \tag{2.27}$$

2.4 Simulation Algorithms

For the investigation of systematic effects introduced by the detection system of NoMoS, a myriad of simulation algorithms had to be utilized. While most of the algorithms will be mentioned whenever they are utilized, in this section the general principle behind them is discussed.

2.4.1 Charged Particle Tracking in NoMoS

Before any particle tracking can be done, the magnetic coil setup of NoMoS has to be simulated. For this purpose, a software called *magfield3* written by Ferenc Glück [53] is employed. The software essentially calculates the contribution of current carrying domains in a system by first segmenting the coils and then summing up the contributions using the Biot-Savart's law. A full description of the magnetic coils that were fed into the software can be seen in the appendix of the work of D. Moser [27]. Assuming enough segmentation of the coils is provided to the software, it can provide a magnetic field map by the coils faster than the finite element method without loss of any accuracy.

Using the magnetic field map provided by the coil data of NoMoS when fed into *magfield3*, a software for particle tracking based on the work from Ferenc Glück [54] was used. The advantage of using this particular software was the built-in integration of *magfield3*, which meant that at any point within the experiment the magnetic field could be evaluated dynamically instead of using an interpolated magnetic field map, thus increasing the speed of the results without loss of accuracy.

Within the context of this work, all particle tracking simulations of particles within the magnetic field setup of NoMoS were performed using this software package and will be referred to as “Monte Carlo simulations".

2.4.2 Interaction of Particles with Matter

The majority of this work focuses on the detection system for NoMoS, where particles' interaction with matter needed to be studied in detail. As a consequence, separate software to study particle-matter interaction were utilized for study of various systematic effects e.g. backscattering, or detector efficiency.

Binary Collision Algorithm

The Binary Collision Algorithm (BCA) approach is used for modelling collisions between an incoming ion and a target atom. The underlying assumptions for BCA is that the interactions of the impinging ion can be separated into a series of two body encounters and any changes in the relative energy of the interacting atoms is confined to the immediate vicinity of the target atoms [55]. The BCA can be further classified into either a "Monte Carlo" BCA or a crystal-BCA. The classification is based upon the selection criterion for the next interaction of the impinging ion with the target material. In a "Monte Carlo" approach, the impact parameter as well as the distance between the collision is chosen randomly from a probability distribution based on the mean free path length of the material. Whereas in a crystal-BCA, the next interaction of the impinging ion with the material is determined in relation to the crystalline lattice of the material. The latter approach is useful in modelling crystalline-specific effects such as "Channeling" (discussed in detail in Sec. 5.1) within simulations. It should be noted that all BCA software starts to "breakdown" at a certain threshold energy of the incoming ion and stops being accurate when the assumption of independent collision between atoms is no longer valid. This energy threshold differs between software and depends on a multitude of factors that can range from the validity of the energy loss theory within the energy regime, to the ability to solve multiple collision integrals. Nonetheless, due to this breaking down of the BCA, at lower energies (in the order of eV), Molecular Dynamics-based software are used instead [56].

Molecular Dynamics Software

Molecular Dynamics (MD) software employ numerical methods to model the interaction of particles with matter. These software instead of simulating one interaction at a time, simulate a large bulk of the system at a time and are able to provide a dynamical evolution of the system as the impinging particle interacts with the matter. However, due to the fact that MD simulates a vast number of atoms at a time, these software are generally quite slower than the software that employ the BCA approach.

While MD-based software are not used within the context of this work, their results were however utilized to check the validity of the BCA software (see Sec. 5.1.2).

It should be noted that the majority of the simulations for this work were performed using the CLIP Scientific Cluster [57].

Chapter 3

The NoMoS Measurement Concept

NoMoS is a precision physics experiment that aims to do momentum spectroscopy of charged decay products from neutron beta decay. Systematic effects within the experiment have to be studied in detail to ensure the final precision goal is met. Consequently, the study of detection-related systematic effects, and their corresponding corrections and uncertainties is of utmost important. This includes an introduction to each area of the experiment and the secondary and primary detection systems. While systematic effects and corrections for the main drift detector are discussed in its own chapter, this chapter focuses on the secondary detection system of the experiment and makes relevant detector technology recommendations based on backscattering studies. After comparison of different detector materials, it is recommended to use scintillators coupled to silicon photomultipliers (SiPMs) for the secondary detectors in the NoMoS apparatus. This recommendation is based on the lower cost of SiPMs compared to silicon sensors, as well as a smaller backscattering rate.

3.1 Measurement Principle of NoMoS

NoMoS is a momentum spectrometer that utilizes the so called $\vec{R} \times \vec{B}$ drift introduced due to curvature of a magnetic field as explained in Sect. 2.3.3. Charged particles with a momentum p will drift perpendicular to the curvature radius $\vec{R}$ of the B-field and the $\vec{B}$ in the direction determined by their charge, thus mapping the momentum of the particles in a spatial "Drift Distance Spectrum" instead. Using a spatially resolving detector, this drift distance spectrum can then be detected and fitted to obtain the observables. The drift distance further depends on the pitch angle θ and the curvature of the magnetic field , as shown in Eq. (2.22). It should be noted that this dependency on the pitch angle is at least one order lower for NoMoS for angles up to 30° than for a conventional magnetic spectrometer and surpasses it after 70°. Therefore, NoMoS is designed with magnetic filter coils that will only allow θ less than

45° into the $R \times B$ region of the experiment when the experiment is used in a stand alone configuration.

While the NoMoS apparatus is fine tuned towards the detection of protons and electrons emanating from free neutron beta decay, the measurement principle in theory can be utilized for almost any beta decay measurement by either adjusting the applied magnetic field to fit the drift distance spectrum onto the detector, or using a detector which can fit the entire drift spectrum of the decaying isotopes i.e. the maximum drift the particles may experience in the field plus two gyration radii r_G at the maximum momentum and θ in the drift direction.

3.1.1 Conductor Technology

In essence NoMoS could be constructed using either normal conducting copper coils or with superconducting coils made from material such as NbTi. While both technologies have their pros and cons, that are extensively discussed in the thesis of D. Moser [27], this work will focus mainly on the superconducting setup for the experiment. This is due to the fact that the superconducting setup not only should lower the uncertainties related to different systematic effects within the experiment [27], but also because it is recommended to be used in order to suppress the $E \times B$ effects that will arise from the post-acceleration of the protons to 15 keV in order to make them detectable [58], as is discussed in Sec. 3.2. Therefore, for the measurement of the electron-antineutrino correlation coefficient a to a relative precision of 10^{-3} the superconducting setup is the obvious choice.

3.2 Main Regions of NoMoS

The NoMoS apparatus, as shown in Fig. 3.1, can essentially be used as a stand alone system where a neutron beam can be fed into it for study of beta decay, or in tandem with a facility such as PERC [59, 60, 61], where a beam of decay products is fed into NoMoS instead. Depending upon which configuration NoMoS is used in, the regions/features of the experiment may change. Nonetheless, the main regions of the system include:

- Decay Volume (Stand alone)
- Back detector (Stand alone)
- Filter Region (Stand alone)
- Aperture
- $R \times B$ Region

- Post Acceleration Region (applicable for protons only)
- Main Drift Detector
- DAQ Region

where stand alone represents the regions which essentially serve a role when NoMoS is used in a neutron beam line.

The Decay Volume

The decay volume is the region capable of magnetically gathering any charged particles which might be generated while a beam of neutrons passes through NoMoS. In the stand alone configuration, decay particles will be directed towards either the $R \times B$ region or the back detector, depending upon the hemisphere they decay in.

The Back Detector

The back detector is a feature of the stand alone version of NoMoS which enables the detection of any particles that are either reflected by the magnetic filter, or decay into the lower hemisphere of the decay volume, consequently drifting away from the $R \times B$ region of the experiment. This region of NoMoS will be discussed in a bit more detail in Sec. 3.3.

The Magnetic Filter Region

The filter region uses the magnetic mirror effect to reflect particles that have an angle higher than a critical angle which depends on the B-field ratios between two points and can be given by extending Eq. (2.19) as:

$$\sin\theta_{\max} = \sqrt{\frac{B_0}{B_{\max}}} \tag{3.1}$$

where a particle with an angle greater than $\theta_{\max}$ is not able to overcome a magnetic field maximum $B_{\max}$ anymore. In the case of NoMoS, the filter coils are designed with a magnetic field ratio between the decay volume and the filter coils of 2.036. As a consequence, the critical angle comes out to to be approximately 45°, leading to the reflection of all particles with a higher θ. In essence, this feature can also be performed externally by a facility such as PERC as well.

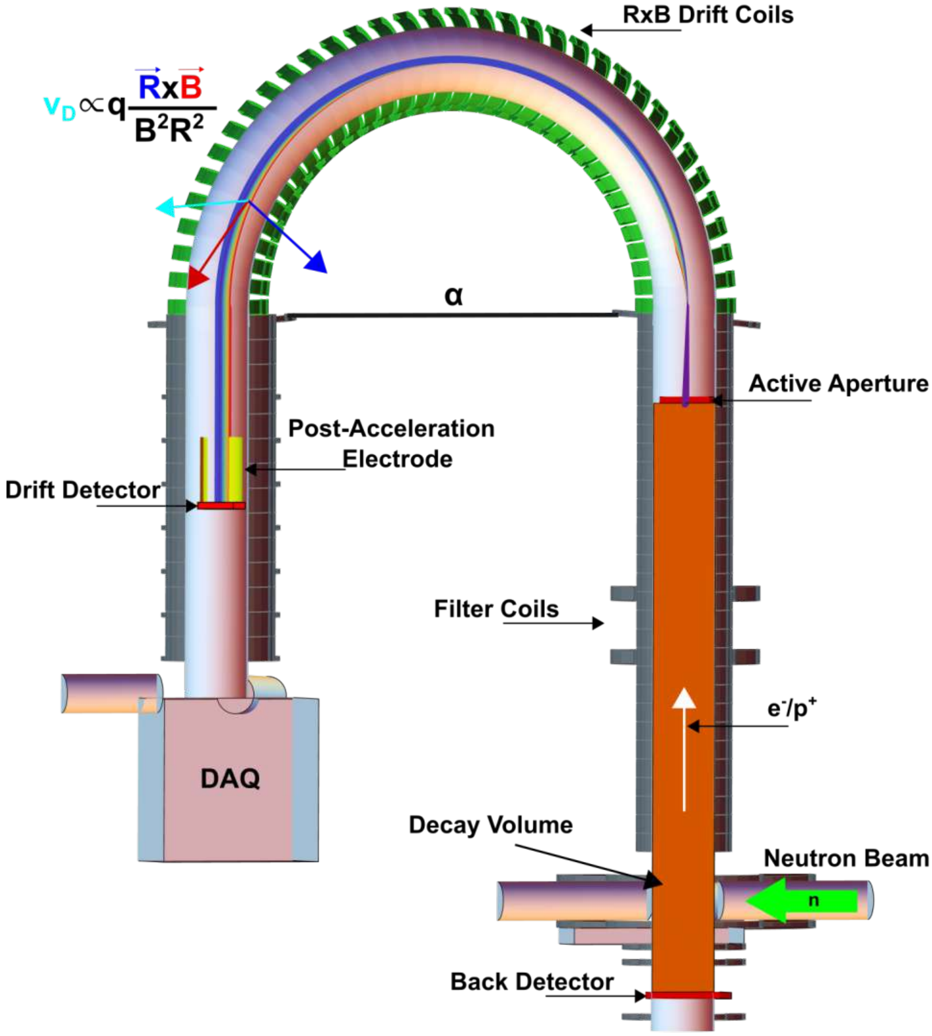

Figure 3.1: Systematic drawing of NoMoS in the stand alone configuration, where the $R \times B$ coils are coloured green. The neutrons enter the system from the right hand side into the decay volume, where any charged decay particles are guided towards either the active aperture or the back detector. Particles with a critical angle smaller than the one defined by the magnetic field at the filter pass through the aperture, enter the $R \times B$ region and experience a drift proportional to their momentum before finally hitting the drift detector. For connection with PERC, NoMoS will not have a back detector so that the beam of charged decay products can pass through towards the $R \times B$ region.

The Aperture

The aperture is designed to not only geometrically shape the beam of decay particles but also function as a backscattering detector for electrons backscattered from the main drift detector of the experiment, as discussed further in Sec. 3.3.2. As the aperture cuts the beam, it introduces an energy- and angle-dependent edge effect that additionally depends upon the homogeneity of the magnetic field within the region. The edge effect and its influence on the beam, along with the detection aspect of the aperture, are further discussed in Chapter 6.

$\vec{R} \times \vec{B}$ Drift Region

After passing through the aperture, the particle beam enters the $\vec{R} \times \vec{B}$ region, where the particles experience a drift due to the curvature of the magnetic field. This curvature is defined by the curvature angle (see Eq. (2.24)), which comes out to be 180.03°, and the bending radius of the coils R. The magnetic field within this region for the superconducting case is 0.976 T. A radial magnetic field gradient $\Delta_r \vec{B} = \frac{\delta}{\delta_r}\vec{B}$ is additionally introduced due to the design of the coils, as they are more densely packed in the inner regions compared to the outer ones. As this behaviour can not be suppressed, it is slightly modified and taken into account [27].

Post-Acceleration Region

To make the protons in the particle beam detectable, they need to be post-accelerated due to their low kinetic energy at decay. This is the region where the post-acceleration electrode will be placed. Details on the electrode design studies can be found in the thesis of R. Jiglau [58], where different electrode designs, its placement within the experiment, the adiabaticity of the electric field, and the additional $\vec{E} \times \vec{B}$ effects introduced are studied in detail. In summary, it is recommended to keep the magnetic field high (≈ 1 T) while having a low post-acceleration electric field (15 keV) to ensure adiabatic acceleration of the protons and to suppress additional $\vec{E} \times \vec{B}$ drift effects. It was also recommended to measure only one species of impinging particles i.e. either protons or electrons at a time, so that the detector can be placed in the centre of the electrode where the electric field is the most homogenous for measurement of the electron anti-neutrino correlation coefficient a [58].

The Main Drift Detector and the DAQ

Finally the particle beam hits the spatially resolving main drift detector, which is further discussed in Chapter 4, together with the Digital Acquisition (DAQ) system and the constraints. In principle, a spatially resolving detector coupled to a DAQ capable of handling a signal rate of 1.5 kHz, which is the number of statistics expected at PERC, is required. This constraint falls to a value of approximately 1.1 kHz for the case of the PF1B beam line at the Institute Laue-Langevin (ILL) [62, 63], situated in Grenoble France.

3.3 Secondary Detection System of NoMoS

While the main drift detector is discussed in far more detail in the next chapter as it requires detailed studies, this section will focus on the secondary detection system within NoMoS and provide appropriate recommendations for data corrections and detector technologies. This includes the active aperture, the backscattering detector and the back detector of NoMoS.

3.3.1 Back Detector

As explained before, the purpose of the back detector is to act as a systematics check monitor for decay particles which are either reflected from the $R \times B$ hemisphere or just simply decay into the hemisphere opposite to the $R \times B$ region when NoMoS is used in a stand alone configuration. As the detection of protons requires post-acceleration, this detector is only meant to function for electrons, to study and correct for various systematic effects. The signal on the detector can originate from:

- Particles which decay into the non $R \times B$ hemisphere
- Particles reflected from the filter
- Particles reflected from the aperture
- Electrons which are reflected from the main drift detector, pass through the aperture and are not reflected back towards the drift detector by the magnetic filter

Simulation studies in conjunction with the data collected from the detector will be used for the correction and systematic studies for electrons arriving at the back detector from the main drift detector, as well as for statistical purposes due to the isotropic nature of the free neutron beta decay. The back detector will also serve a role in systematic studies of the backscattered electrons which may re-enter the $R \times B$ region after backscattering from it.

Since scintillator-based detectors are comparatively cheaper to silicon pixel sensors, and have a smaller backscattering rate due to their lower material density compared to that of an off the shelf silicon-based detector, it is recommended to use scintillators optically coupled to silicon photomultipliers (SiPMs). SiPMs are the ideal detector for this case as not only can they function in high magnetic field environments but their small sizes also makes them quite suitable to be used in small spaces. It should also be noted that depending upon the thickness of the scintillator, calorimetric readings could also be performed. For a PMMA-based scintillator, this leads to a thickness of $\approx 3\,\mathrm{mm}$ in order to stop electrons with $800\,\mathrm{keV}$ kinetic energy [64]. As NoMoS will operate in ultra high vacuum (UHV) of $1 \times 10^{-4}\,\mathrm{Pa}$, some effort will have to be made to ensure limited outgassing of the scintillation material and the electronics on which the SiPMs will be mounted.

Backscattering from the Back Detector

As electrons or protons that backscatter from the back detector may have a chance of re-entering the $R\not\times B\not\;$region with modified angles and energies, this effect was studied in detail to provide appropriate recommendations towards data correction.

Table 3.1: Energy-dependent fit coefficients for the backscattering percentage. For details see text and Eq. (3.2)

Incident Energy (keV)	A_0	A_1	A_2
60	0.02	0.0029	0.0627
120	0.0177	0.0024	0.0647
180	0.0171	0.002	0.067
240	0.0159	0.002	0.0668
300	0.0153	0.0017	0.0688
360	0.0151	0.0014	0.0707
420	0.0147	0.0014	0.0706
480	0.0136	0.0013	0.0713
540	0.0135	0.0012	0.0722
600	0.0136	0.001	0.0743
660	0.0127	0.0011	0.0737
720	0.0121	0.001	0.0744
780	0.0119	0.0009	0.0756

For the choice of detector material, a study of the backscattering behaviour was performed using CASINO [65] for electrons and SRIM [66] for protons on a PMMA-based scintillator material (Lucite, ICRU-223). The backscattering rates of both electrons and protons on the back detector can be seen in Fig. 3.2. Due to the low energy of protons in neutron beta decay, a higher percentage of protons is backscattered, even at lower angles, compared to the electrons which show a very high backscattering rate at higher angles. Therefore, it is recommended to have an electrostatic barrier of roughly $-1\,\mathrm{keV}$ by applying a electric field on the detector to stop the protons (with maximum kinetic energy of about 800 keV) from going towards the $R \times B$ region, especially when protons are being measured at the drift detector, as already discussed in [67].

Corrections will have to be made for the case of electrons that are backscattered from the back detector and deposit a signal on the main drift detector with modified energy and angles. The probability distribution of the electrons that are backscattered can be modelled in terms of the incident polar angle θ_{inc} as a function of incoming energy T_e by [68]:

$$\eta(\theta_{\mathrm{inc}}, T_e) = A_0(T_e) + A_1(T_e) + \exp(A_2(T_e)\theta_{\mathrm{inc}}), \qquad (3.2)$$

where θ_{inc} is in degrees and A_0, A_1, A_2 are energy-dependent coefficients whose values are given in Table 3.1 as obtained by fitting the data for a PMMA-based scintillator. The fit results are shown in Fig. 3.3 along with the simulated points for three different energies of the impinging electrons. Fig. 3.4 shows the angular distribution of the backscattered electrons for different angles of incidence with an incident kinetic energy of 300 keV. For angles $< 45°$, it can be seen that the angular probability distribution of the backscattered electrons has a peak at 45°. This means from the overall backscattered electrons only a small number of them make it through the filter and towards the aperture. It should be noted that the back detector will be placed in an area of lower magnetic field than the decay volume, therefore backscattered electrons will have their angles further widened when travelling back to the decay volume in accordance with Eq. (2.19).

Figures 3.5a and 3.5b show the energy and polar angle histograms of decay electrons within the decay volume of the experiment. Using these histograms a Monte Carlo investigation with 1×10^6 particles was performed to ascertain how the drop in the magnetic field from the decay volume to the back detector changes the polar angular distribution of the electrons. For a back detector placed 50 cm from the decay volume, where the magnetic field is reduced by approximately a factor of 8.5, the impinging electrons have their angular distributions reduced to a maximum of 28° from as shown in Fig. 3.6 (see Eq. (2.19). As expected there are fewer electrons at lower angles as angles less than $\approx 45°$ make it through the aperture, whereas higher angles are either reflected back (for angles between 45° and 90°) from the magnetic filter, or they decay towards the back detector (angles $> 90°$).

Using these facts, and the principle of conversation of magnetic flux, it is recommended to have a back detector with an area of $150 \times 150\,\mathrm{mm}^2$ in the superconducting version of the experiment. Due to the relatively large area for the back detector to cover, this further motivates the choice of a scintallator based detector coupled to SiPMs as they are relatively cheaper compared to other detector types.

A more detailed analysis of the effect on the Fierz interference term b for backscattered particles reaching the drift detector is presented in Chapter 6 in Sec. 6.4.5.

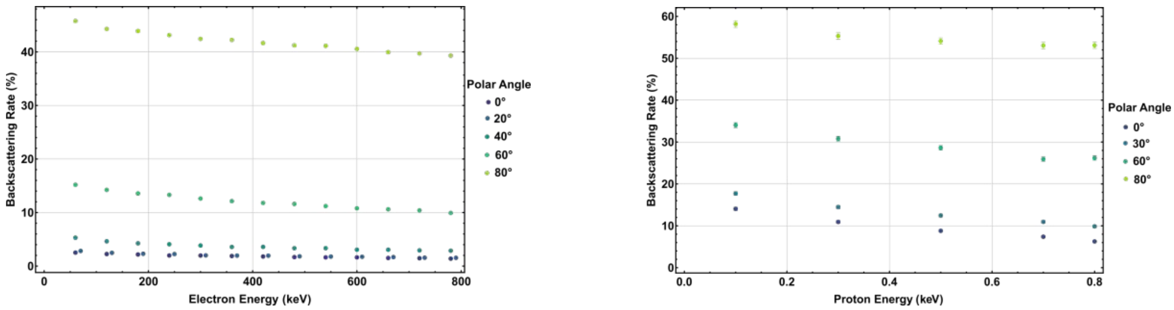

(a) Backscattering rate of electrons (b) Backscattering rate of protons

Figure 3.2: Backscattering yield of the charged decay products from a PMMA-based scintillator back detector. Please note that for the case of electrons at 20° in Fig. 3.2a, the energies are shifted by 10 keV for the sake of clarity. Also, it should be noted that in most cases the error bars are smaller than the plot points. A total of 100,000 electrons in Casino and 50,000 protons in SRIM for each energy and angle combination were simulated.

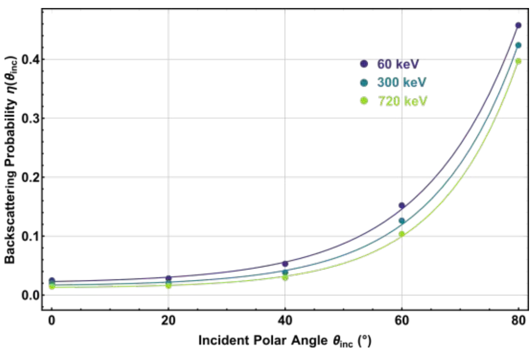

Figure 3.3: Fit results for the percentage of backscattered electrons from PMMA for three different energies according to Eq. (3.2).

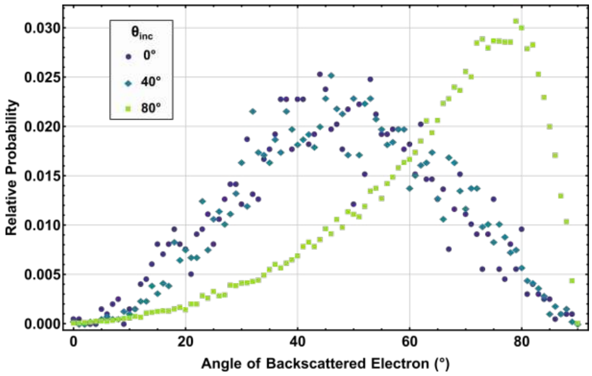

Figure 3.4: The polar angular distribution of backscattered electrons at different angles of incidence for an incident kinetic energy of 300 keV, simulated using Casino for 100,000 electrons.

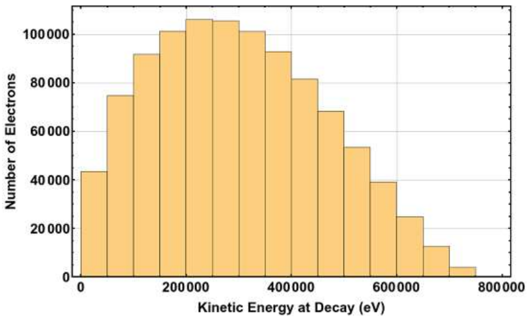

(a) Kinetic energy histogram of the electrons at decay within the decay volume

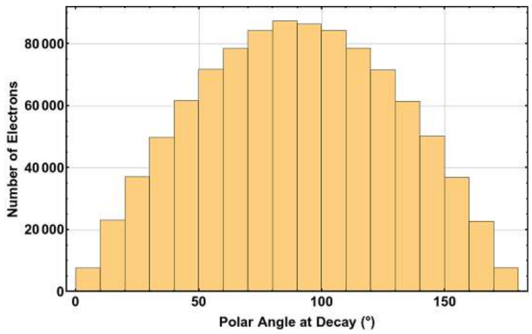

(b) Polar angule histogram of the decay electrons within the decay volume.

Figure 3.5: The energy and angular histograms of decay electrons at the time of decay. It should be noted that electrons with angles greater than 90° travel towards the back detector whereas smaller-angled electrons propagate towards the magnetic filter. Simulated with the Monte Carlo code for 1×10^6 particles.

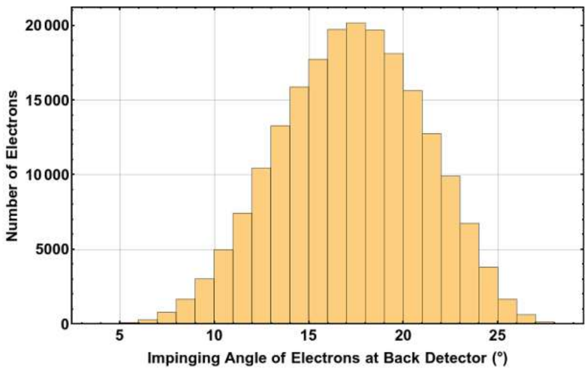

Figure 3.6: Histogram of the angular distribution of decay electrons at the Back Detector placed 50 cm away from the decay volume. Simulated with the Monte Carlo code for 1×10^6 particles.

3.3.2 Active Aperture

The design of the active aperture is a complicated task on its own. As not only does the aperture introduce edge effects by shaping the beam, it will also alter the energy and angular distribution of the particles which scatter off on its inner edges [69]. To consider the latter effect, it is recommended to have the aperture "active" on its inner surfaces as well as on the side which faces towards the $R \times B$ region. The recommended detection technology for this purpose is also scintillator-based with the scintillators additionally being coated with a highly reflective material towards the edges which touch other scintillators. The purpose of the additional coating is to prevent cross talk effects of the generated scintillation light. Figure 3.7 shows an illustration of the concept where the red part is the backscattering detector facing towards the $R \times B$ region in order to detect backscattered electrons from the main drift detector. The green part is the active aperture surface to detect electrons scattering off on the inner surfaces of the aperture. It is recommended to use SiPMs with scintillators due to their size, and ability to operate in high magnetic field environments. Due to the low energy of the protons, they can not be detected at the aperture and therefore the proton drift distance spectrum will have to be corrected additionally with the help of MC simulations once the active aperture is fully designed. However, for the case of the electron drift distance spectrum, it is recommended to use the active aperture surfaces as they will help to veto electrons scattered off on the aperture's inner surfaces while the backscattering detector will help veto signals in the main drift detector left by electrons that backscatter after depositing enough energy for a detectable signal (see Sec. 6.4.4).

As it can be seen just from the simple illustration that there are many factors to consider when designing the aperture. The most important things to consider during this endeavour are to:

- Choose a scintillator material with as little outgassing as possible due to UHV conditions of NoMoS.
- Careful manufacturing of the PCBs on which the SiPMs will be mounted to reduce outgassing. Alternatively, the SiPMs can also be placed outside the vacuum tube using waveguides.
- Ensuring the non-scintillator end is properly grounded to prevent charging of the aperture.
- Ensuring the geometrical tolerances of the scintillator and aperture are in accordance to those recommended in Chapter 6.
- Study and correction of the work function differences to that of the DV introduced by the additional materials and how they may influence the particle beam,

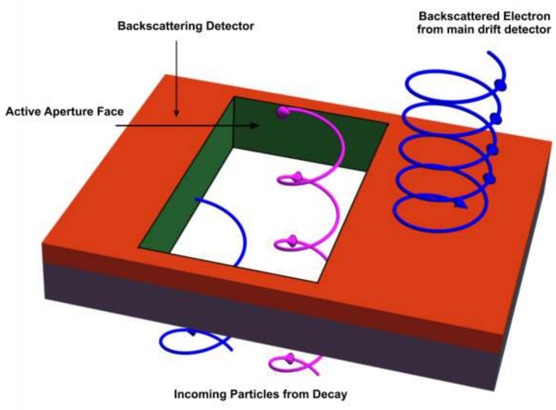

Figure 3.7: Illustration of the active aperture. The green and red colours represent two different scintillator detectors. The majority of particles backscattered from the drift detector will be detected by the backscattering detector part of the aperture whereas particles scattering off on the inner faces of the aperture will be detected by the active aperture face.

especially the low energy protons.

It should be noted that backscattered electrons will have an additional probability of being backscattering on the backscattering detector and being detected at the main drift detector once again, such as in the case of the back detector. However, this can be easily corrected for in the post analysis of the data with the help of Monte Carlo studies or by introducing cuts based on the time of flight of the backscattered electrons and is further discussed in Sec. 6.4.4.

Chapter 4

NoMoS Drift Detector

As NoMoS aims to measure both electrons and protons by employing the $\vec{R} \times \vec{B}$ effect, it consequently requires a spatially resolving detector, capable of submillimeter resolution, which is also efficient at low energies in the order of 10 keV and covers an area of 4 cm × 5 cm for the superconducting case of NoMoS. Furthermore, as both electrons and protons have different energy ranges, the detector needs to be compatible with a varying energy scale from the order of 10 keV to 100 keV. These requirements put stringent constraints on detector choice and demand a robust detector technology, that is capable of reading out both particle types in different energy ranges without having to switch the detector by breaking the ultra-high vacuum of the experiment.

While, for the case of electrons a silicon strip detector can be used, it presents a considerable challenge for the case of the protons. In order to tackle this challenge, a new silicon based sensor design based on existing silicon sensors with linear internal gain and thin entrance windows was proposed and consequently patented [20]. The pLGAD is based on the already existing iLGAD technology and is designed for the detection of low-penetrating particles, i.e. particles with a penetration range of < 1 µm in silicon. The proof of principle prototypes from the first production run of the sensor were tested and showed excellent internal gain for low-penetrating particles. Furthermore, the measured waveforms carried a distinctive shape due to the gain experienced by low-penetrating laser light similar to that obtained by simulations of the detector, thus providing evidence that the detector worked as intended.

4.1 RxB Drift Detector

As protons emanating from free neutron beta decay have a maximum kinetic energy of 751 eV [24], they need to be post-accelerated to be made detectable. NoMoS is an apparatus that uses the $R \times B$ drift concept to transform the momentum of the charged decay particles into spatial dependence. Therefore, for the measurement of this drift distance spectrum, a spatially resolving detector is required. Furthermore, this detector should also offer good signal to noise separation for low-energy particles. This is because protons, even after post-acceleration will only be accelerated to a potential of $-15\,\text{keV}$ to avoid complications such as additional $\vec{E} \times \vec{B}$ drifts, and far reach of the electric field of the electrode into the $R \times B$ region, as discussed in the thesis of R. Jiglau [58].

The requirements of the drift detector in NoMoS are as follows:

- High spatial resolution in the drift direction in the order of $< 1\,\text{mm}$
- High efficiency at the low energy of $\approx$15 keV, for the case of post-accelerated protons, emanating from free neutron beta decay.
- coverage of a detection area of $10\,\text{cm} \times 7\,\text{cm}$ for the normal conducting and of $4\,\text{cm} \times 5\,\text{cm}$ for the superconducting configuration in order to detect the entire drift distance spectrum of a decay electron or a proton.
- Compatible with a signal rate of 1 kHz
- Internal signal amplification
- Low noise
- Homogenous, thin entrance window, with a dead layer thickness in the order of 10 nm
- Low backscattering rate of electrons and protons from the dead layer
- Operation in ultra-high vacuum and in a magnetic field

4.1.1 Choice of Detection Technology

There were some detection technologies that match the above stated criterion, such as multichannel plates (MCPs) attached to positional readouts, silicon detectors, and scintillators coupled to silicon photomultipliers (SIPMs).

While MCPs offer an absolute efficiency of $\approx 86\%$ or perhaps even a bit more [70], issues such as spatial-response uniformity, or deterioration of uniformity [71] made them an unappealing choice for the main drift detector. Alternatively, SIPMs coupled with scintillators, scintillator fibers or conversion foils were also not promising due to the low light output for protons in the 15 keV energy range [72].

Although in theory, silicon detectors offered the best signal to noise ratio and efficiency of all the technologies that were considered, they still could not be used off the shelf. This was due to the fact that most silicon technologies available on the market are made for high-energy physics applications where the particles pass through the

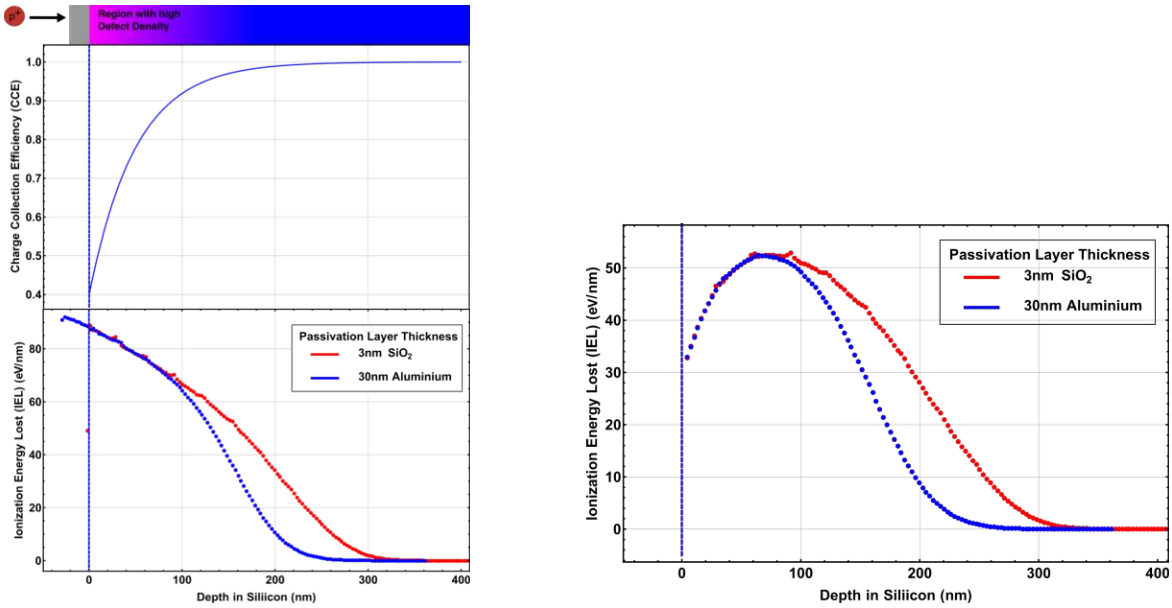

(a) Top: CCE of a DEPFET sensor [73, 74]. Bottom: Ionization energy lost per nanometer

(b) CCE convoluted with the ionization energy lost per nm

Figure 4.1: Simulation of ionization energy lost per nanometer by 15 keV protons impinging on silicon detectors with different passivation layers at 0° relative to the surface normal, convoluted with Charge Collection Efficiency (CCE) of DEPFET sensors for the estimation of detectable e-h-pairs. For details see text.

entire sensor. Most of these detectors use non-active passivation layers or conduction layers in the range of µm to protect the surface of the detector from environmental damage. Any signal deposited by impinging particles in this area is lost. Furthermore, the wafer surface underneath the passivation layer has a higher defect density than the bulk and is heavily doped to form a field stop. Any electron hole pairs (e-h-pairs) liberated within this region face a higher probability for recombination, leading to a further reduced measurable signal. Results of self-performed simulations in SRIM and IMSIL show that 15 keV protons impinging on pure silicon at 0°, from the normal of the wafer, have a mean penetration depth of about 300 nm. Therefore any signal lost in the non-active layer or region of the detector where the charge collection efficiency (CCE) of less than 1 can cause significant loss of signal. This effect is illustrated in Fig. 4.1, which shows the simulated Ionization Energy Loss (IEL), that is the energy of a proton lost in detectors with different thicknesses of passivation layers on top.

Figure 4.1a (top) shows the measured charge collection efficiency of thin windowed DEPFET silicon sensors [73] (courtesy of P. Lechner [74]). Due to recombination, more e-h-pairs generated near the surface are lost. The CCE describes the probability that an e-h-pair survives recombination and can be measured. In this specific case, it starts at 0.4 at the interface between the non-active layer and the sensor material and reaches 1 at a depth of 250 nm. This probability is then convoluted with simulations of the IEL as a function of depth of 15 keV protons at 0° performed using IMSIL [75][76] for silicon detectors with different passivation layers, as shown in Fig. 4.1a(Bottom). The choice of passivation layers was made from already existing detector technologies, where 30 nm of aluminium was the conduction layer thickness of the *a*SPECT detector [10] and 3 nm of SiO_2 is the passivation layer thickness of N$ab\psi$[77]. As can be seen from Fig. 4.1a (bottom), the thicker non-active layer in front of the detector not only leads to less ionization energy being lost within the active area of the detector, but also a shallower range within the sensor. When the number of e-h-pairs are then combined with the aforementioned recombination of e-h-pairs near the detector surface, it leads to a further reduction of the ioniziation energy lost by the particle, as shown in Fig. 4.1b. The convoluted IEL is then integrated over all the depth bins in the figure to obtain the total number of measurable e-h-pairs. For the 3 nm SiO_2 case, a total of 3350 e-h-pairs are detectable whereas for the 30 nm aluminium case, that number is reduced to 2600 e-h-pairs. The number of e-h-pairs is an order of magnitude less than what is usually expected in high-energy physics case for minimum ionizing particles (MIPs).

From this information, it was deduced that the needs of the experiment could be met by the use of a planar silicon sensor if it had an interior multiplication layer, a very thin entrance window, and used electrons as its majority charge carriers. As no such planar sensor incorporating the three technologies existed, a custom development was required.

4.2 A new silicon sensor concept

4.2.1 Silicon Sensors

Silicon sensors at their very core are simple P-N junctions that are made by combining two extrinsic semiconductors with trivalent (P-type) and pentavalent (N-type) dopants. These devices are operated in reverse bias mode and a signal is generated whenever an incident particle deposits enough energy to liberate an e-h-pair. For the case of protons impinging on silicon, this energy is equal to 3.6 eV. The liberated e-h-pairs drift in opposite directions of each other towards their respective attracting electrodes. This drift of the e-h-pairs generates a current signal on the readout. The instantaneous current i generated on a specific electrode is given by the Shockley-Ramo theorem as [78]:

$$i\psi= E_v q v,\psi \tag{4.1}$$

where q is the particle's charge, v is its instantaneous velocity and E_v is the so called weighting field which is basically the electric field in the direction of v at the charge's instantaneous position under the conditions that the charge is removed, the electrode of interest is raised to unit potential and all other electrodes are grounded.

Avalanche Photo Diodes (APDs)

An avalanche photodiode (APD) is a semiconductor based photodiode with an internal gain mechanism for the generated e-h-pair. It accomplishes this by introducing two heavily doped and two lightly doped regions. In keeping with the nomenclature, this work will show heavily doped regions with a "+" sign e.g. a P+ region will denote an extrinsic semiconductor doped heavily with electron accepting elements. Particles impinging on the APD create e-h-pairs which after reaching the strongly doped P-N junction go through the process of impact ionization due to an increase in the electric field generating more e-h-pairs. This results in an avalanche-like multiplication of the initial charge carriers and consequently a larger signal is observed.

4.2.2 Linear Gain Avalanche Diodes

The Linear Gain Avalanche Diodes (LGADs) and inverse Linear Gain Avalanche Diodes (iLGADs) [79] are relatively new silicon sensor developments and are an evolution of the classic APD by having a reduced gain factor. Unlike APDs, LGADs operate in the region of linear gain (in the order of 10-30) instead of the Geiger mode observed in APDs. While the incoming signal in LGADs is still multiplied by having a region of high electric field, their usage in the linear gain mode leads to a reduction of the excess noise factor, which is additional noise associated with the multiplication process [80]. Additionally, the electric field within LGADs only allows electrons to reach the critical velocity for impact ionization due to their higher saturation velocity, compared to that of holes, within silicon.

The bias voltage and the rate of change of the doping concentration defines the electric field within a semiconductor. The doping concentration changes quite drastically at the p-n junction, where the polarity of the doping changes. Within an LGAD sensor, this is further enhanced by introducing an additional doping layer at the p-n-junction: the so called multiplication layer. The multiplication layer always has the same polarity as the substrate, and for the case of LGADs is put below the electrode implant that is used to couple the sensor to the readout, as shown in Fig. 4.2 (left).

However, as it can be seen from Fig. 4.2 (left), this only offers spatially inhomogeneous gain due to segmentation of the electrodes for achieving a position-sensitive readout. Consequently, this reduction of fill factor leads to regions within the sensor with smaller or no gain. To avoid this problem, iLGADs were invented. The iLGADs proposed to segment the ohmic side of the sensor, keeping the multiplication side with

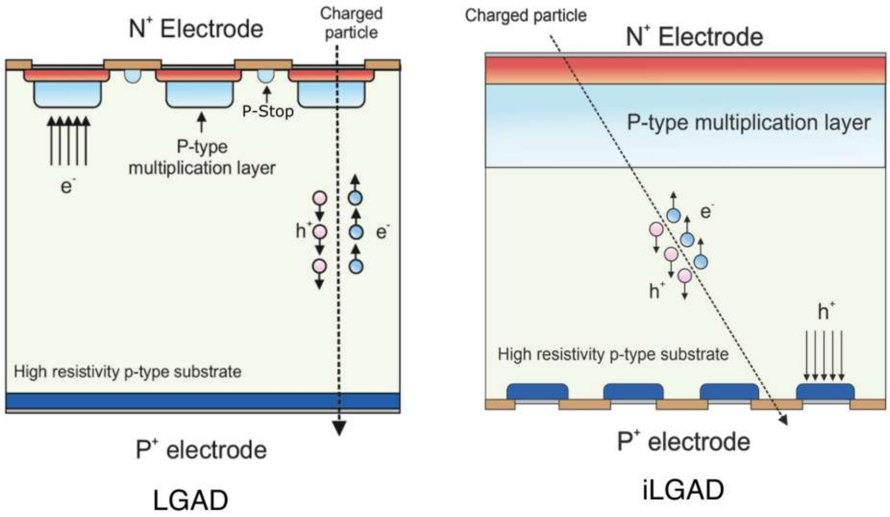

Figure 4.2: Schematic drawings of the Low Gain Avalanche Diode (LGAD) and the inverse Low Gain Avalanche Diode (iLGAD) detectors. A traversing particle is indicated by a dashed line. Darker colours mean higher doping concentration.

a single and wide multiplication area while achieving the same spatial sensitivity for the impinging particles on the ohmic face of the sensor as shown in Fig. 4.2 (right). In both of these cases, the main contribution to the signal comes from secondary holes, which are created by the multiplication of primary electrons from the e-h-pairs generated within the bulk of the sensor by the impinging particles.

4.2.3 The pLGAD Concept

Based on the iLGAD concept [79], and the results of the backscattering and efficiency simulations (see Chapter 5) conducted by me, a new sensor concept was envisioned within the group in collaboration with the Institut de Microelectrònica de Barcelona (IMB-CNM-CSIC) for NoMoS in particular and for experiments with low-penetrating particles in general. Here low-penetrating particles refer to any particles which have a penetration depth of $<1\,\mu m$ within silicon. The proposed proton Low Gain Avalanche Diode (pLGAD) sensor concept [20] is designed with inverted doping compared to a traditional iLGAD, and takes matters two steps further: the pLGAD is equipped with a very thin, unstructured passivation layer of 2 nm of aluminium oxide deposited via the atomic layer deposition technique (ALD) (or desirably in the future: a thin 15 nm aluminium conduction layer) and a thin field stop in the order of 10 nm. The sensor concept furthermore introduces a collection region by having the p-n-junction and the multiplication layer deeper in the bulk, away from the entrance window. Lastly,

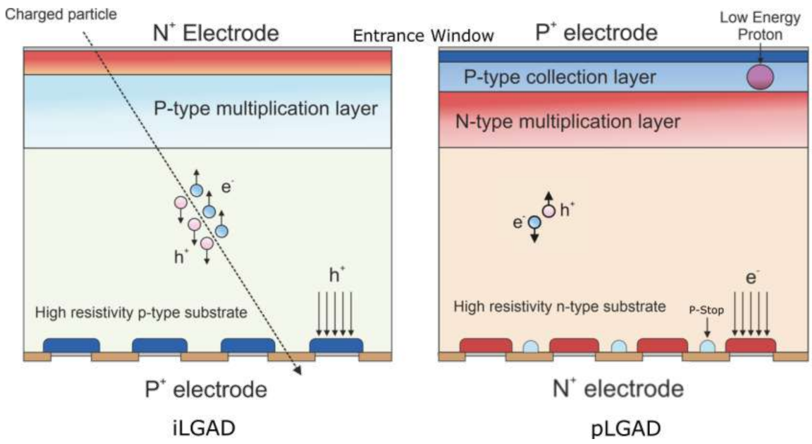

Figure 4.3: In contrast to the iLGAD concept, the pLGAD concept uses inverted implantation polarity. This way, only signal electrons created in the collection region are amplified, directly next to the entrance window. The main contribution to the signal stems from the secondary electrons. Darker colours represent higher doping concentration.

the polarity of the signal-collecting electrode is chosen to be an N-type, so that the signal electrons drift to the readout sensor side and cross the multiplication layer, as illustrated in Fig. 4.3 (right). This also has the added benefit that thermal e-h-pairs produced within the bulk of the sensor are not multiplied as holes do not cause impact ionization when crossing the N-type multiplication layer.

A low-energy proton impinging upon the sensor will deposit the bulk of its energy in the collection layer of the sensor. This will liberate e-h-pairs, where the holes will drift towards the entrance window and the electrons will drift towards the N^+ electrode. The electrons will undergo impact ionization once they arrive at the multiplication layer due to increase in the electric field at the p-n-junction. This will liberate more e-h-pairs within the sensor and cause the initial signal to see a gain at the readout side, as illustrated in Fig. 4.3. The P-stops are there to stop accumulation of charge at the electrodes and prevent sensor breakdown and are a consequence of the chosen polarity of the sensor. Alternatively, when a MIP passes through the sensor, it will deposit the majority of its signal within the bulk of the sensor, but nonetheless a very small amount of the deposited signal (within the first 5 µm before the multiplication layer) from the impinging MIP will see a gain. That being stated, for high energy physics applications the pLGAD will work as a normal silicon sensor and as a result may not be interesting in high energy environments.

In principle, the collection region defines the uniformity of the gain seen by any particle. Its depth can be adjusted by placing the gain region deeper into the sensor (via epitaxial growth) or near the unstructured entrance window (via ion implantation) during the production stage. This gives the pLGAD concept an additional advantage of being flexible for low-energy, high precision experiments.

Simulation Results of Doping Concentration and Breakdown Voltage

In order to obtain the appropriate breakdown voltage, V_{bd}, and the expected gain in the pLGAD, numerical simulations using Technology Computer Aided Design (TCAD) Sentaurus [81] were performed at IMB-CNM-CSIC [82]. TCAD simulations are simulations that model the semiconductor fabrication and operation. The results of the simulations are shown here for the sake of completeness.

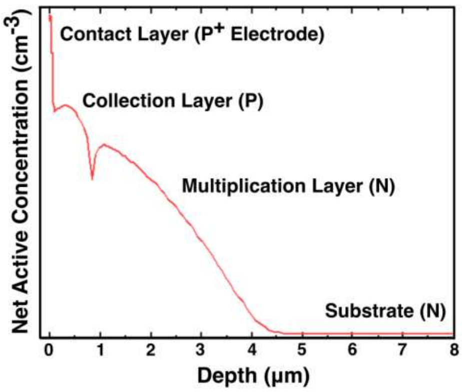

(a) Doping profile of the pLGAD sensor concept

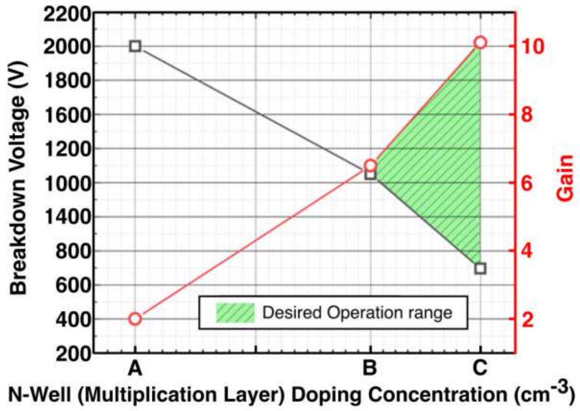

(b) Expected gain and the breakdown voltage of a pLGAD sensor as a function of three different doping concentrations of the multiplication layer (n-type), represented by A, B, and C. The operating range refers to the desired breakdown voltage and gain offered by a specific doping concentration.

Figure 4.4: Technology Computer Aided Design (TCAD) simulations for the pLGAD sensor concept. Images courtesy of A. Doblas [82]

Figure 4.4a shows the doping profile of the various layers of the pLGAD structure on the proposed N substrate. The key quantity for fine-tuning the operation of the sensor is the doping concentration of the multiplication layer (N-Well) as shown in Fig. 4.4b. The green area in the plot represents the operating range of interest for the sensor. This area was chosen to have the lowest V_{bd} while obtaining an acceptable gain for the detection of the low-energy protons.

From the TCAD simulations (Fig. 4.4b), it could be concluded that a pLGAD with a gain of 10 and a V_{bd} of 700 V can be fabricated by using an N-well doping concentration, that is represented by point C in the figure.

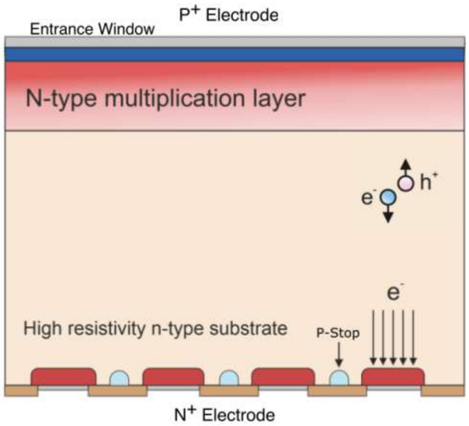

Figure 4.5: Schematic drawing of the first prototypes of pLGAD, without a collection region and a thicker entrance window.

From these simulations, the doping concentrations for the different layers of the sensor were calculated so a first prototype of the pLGAD could be manufactured. It should be noted that the numbers for the net active doping concentrations in Fig. 4.4 can not be shown as they are a manufacturing secret of IMB-CNM-CSIC.

4.3 First Prototypes of pLGAD Sensors

In order to verify that the proposed sensor concept is feasible, a first production run of pLGAD sensors without a P-type collection region, a standard passivation layer of silicon nitride Si_3N_4 albeit with a thin backplane, and shallow multiplication implant was conducted at IMB-CNM-CSIC on a 6-inch silicon wafer, as shown in Fig. 4.5 and 4.6a [83]. A total of six wafers with varying doses of phosphorus for the n-type multiplication layers were manufactured. Unfortunately as this was the first attempt to manufacture a silicon sensor based on the iLGAD concept with a n-type substrate and a n-type multiplication layer as opposed to the commonly used p-type substrate in high energy physics, only one functioning wafer with the correct amount of phosphorus dose was found.

From the manufactured wafer, four $5.3 \times 5.3\,\mathrm{mm}^2$ diodes were chosen based on their measured current-voltage (I-V) and capacitance-voltage (C-V) curves, as shown in Fig. 4.6.

From Fig. 4.6b, it can be seen that the chosen diodes have an operational working range $V \leq 100\,$V. Furthermore from Fig. 4.6c, it was found that the diodes are fully depleted at $V \approx 30\,$V. This meant that the sensors could be operated at a voltage $V \gtrsim 30\,$V with a linear gain before breaking down at $V > 100\,$V

Using the data from Fig. 4.6c, the depletion width of the sensor as a function of

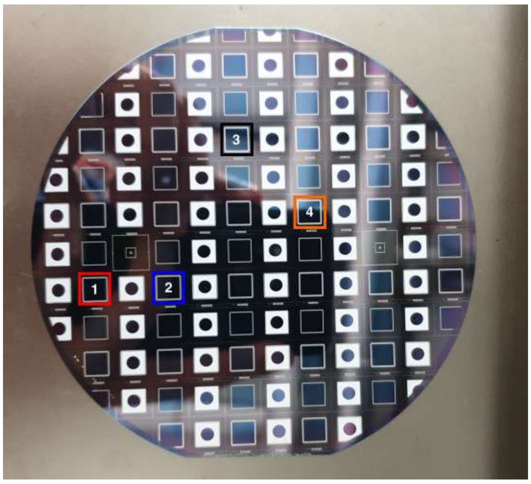

(a) The chosen diodes' position on the silicon wafer

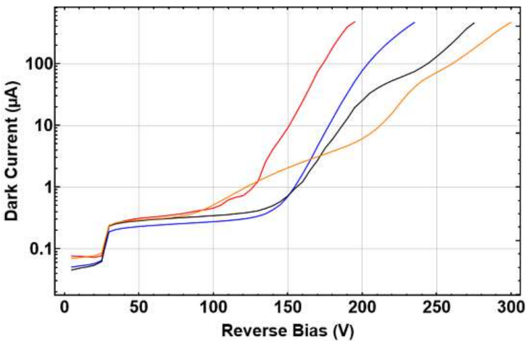

(b) Current-Voltage (I-V) curves of the first prototypes.

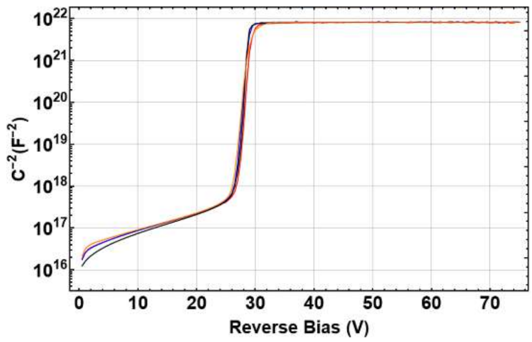

(c) Inverse capacitance Squared-Voltage curves of the first prototypes

Figure 4.6: Measured I-V and C-V curves of the first prototypes. Different colours represent a different diode as shown on the picture of the wafer.

the applied voltage was calculated using:

$$d = \frac{\epsilon A}{C(V_{FD})} = \frac{11.68\epsilon_0 A}{C(V_{FD})} = 262\,\mu\mathrm{m}, \tag{4.2}$$

where A is the area of the sensor, C is the measured capacitance as a function of the full depletion voltage V_{FD}, and ϵ is the relative permittivity of silicon. Using Eq. (4.2), and Fig. 4.7 a mean thickness of 262 µm for all four diodes was calculated. This is in agreement with the TCAD simulations of the diodes performed by IMB-CNM-CSIC.

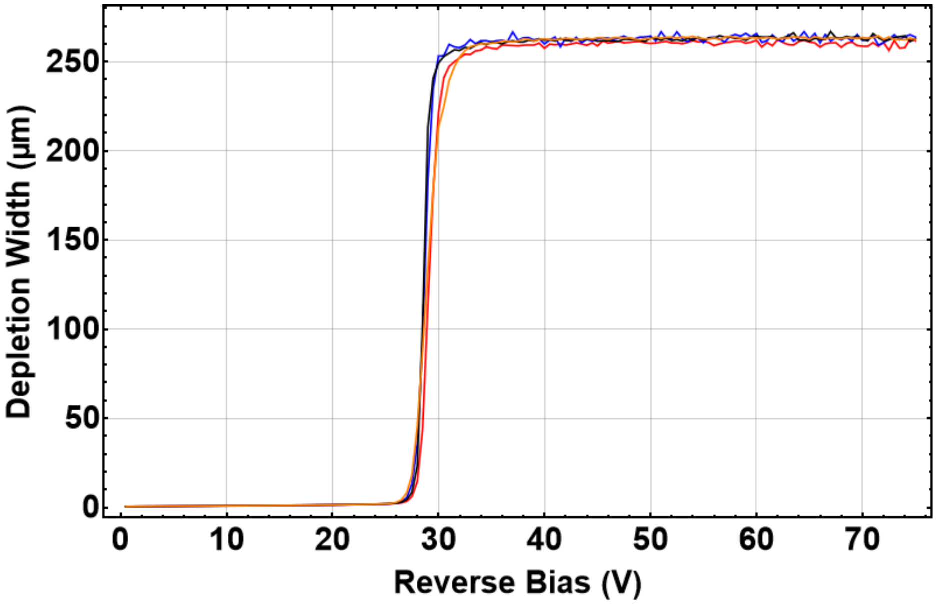

Figure 4.7: Depletion width of the first prototypes calculated using Eq. (4.2). Mean sensor thickness comes out to be 262 µm

4.3.1 Transient Current Technique Measurements

Once it was established that the diodes were functional, the next step was to perform Transient Current Technique (TCT) measurements to determine the gain and charge collection uniformity of the diodes. For this purpose three of the four diodes were chosen, as the fourth diode was used for quantum efficiency measurements with a laser of varying wavelengths (see Appendix A).

The TCT measurement setup can be seen in Fig. 4.8. The diodes were wire bonded to the readout printed circuit board (PCBs) as seen in the top of the figure. Two lasers, a near ultraviolet (UV) laser of 404 nm, and an infrared (IR) laser of 1064 nm were used in conjunction with the laser optics setup to control the optical properties of the laser for the measurement. The respective diode was connected to a CIVIDEC amplifier [84] and the PCB was placed on top of a thermoelectric cooler to regulate the diode temperature. The whole setup was located inside an airtight, dark metal container and flushed with nitrogen gas to avoid condensation when measurements at lower temperatures were conducted.

Firstly the uniformity of the charge deposited on the diodes was investigated by moving the near UV laser along the surface of the diodes in steps of a few µm to form a 2D map of the deposited charge. This was done to find a spot for subsequent measurements on each diode where the deposited charge is uniform. The laser configurations used for the TCT measurements are presented in Table 4.1.

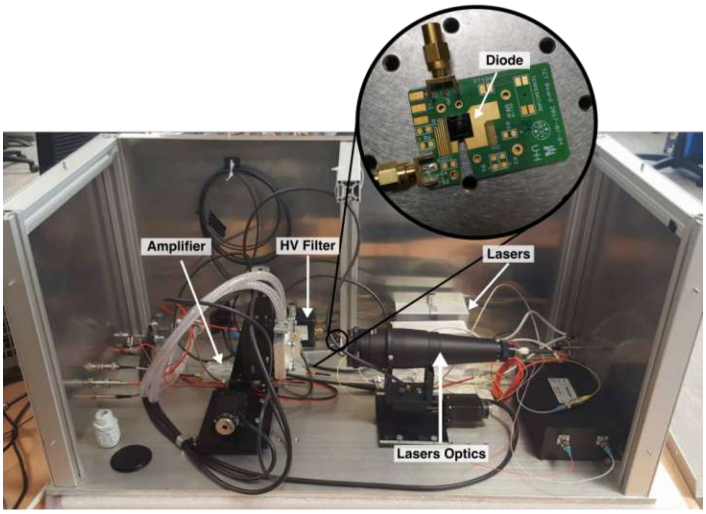

Figure 4.8: TCT measurement setup

Table 4.1: Properties of the lasers used for the TCT measurements

Laser Wavelength	Frequency	Pulse Width	FWHM	Diode No.
1064 nm	1 kHz	3.2 ns	250 µm	1
1064 nm	1 kHz	2.2 ns	250 µm	2, 3
404 nm	1 kHz	3.92 ns	250 µm	1, 2, 3

The distribution of the deposited charge as a function of a specific point on the sensor can be seen in Fig. 4.9. The areas where the diodes were wire bonded to the PCB are the ones where the diodes show a higher charge deposition. However, that is to be expected as wire bonding the diode to the PCB causes surface damage to the diodes. Another fact to note is that for diode 1, as shown in Fig. 4.9a, there are two “hot spots”. This may be due to that fact that this specific diode was close to the corner of the silicon wafer and consequently may not have received uniform ion deposition. In any case, for all three diodes, voltage scans for the determination of the gain of the diodes compared to that of a PIN diode were done in regions where the deposited charge is uniform as marked by circles in Fig. 4.9. It should be noted that the PIN diode was manufactured on a wafer from the same silicon crystal as the diodes, and had the same entrance window as the prototypes. However, the PIN diode was not subjected to ion implantation for the introduction of a gain layer.

Determination of Gain

A sample of the average deposited charge, average rise and collection time at room temperature (20 °C) for diode 1 are shown in Fig. 4.10. As the IR laser has an ab-

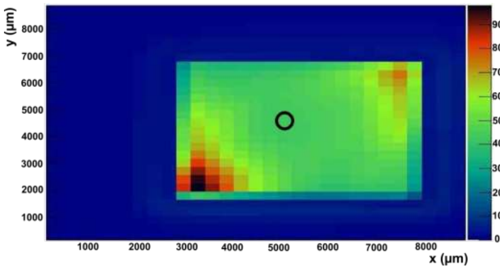

(a) Diode 1

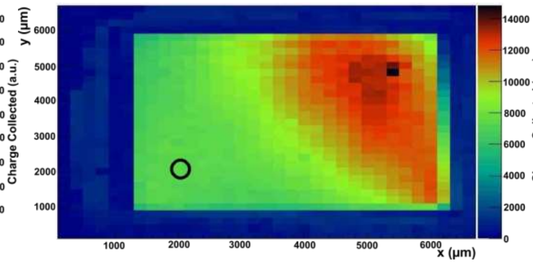

(b) Diode 2

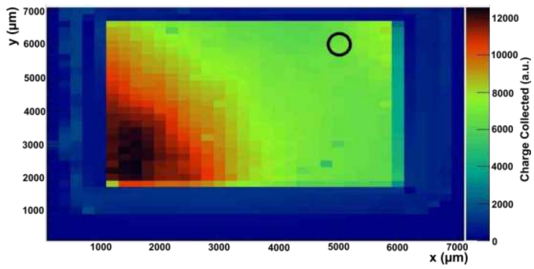

(c) Diode 3

Figure 4.9: 2D Maps of charge deposited on the diodes using a laser with 404 nm wavelength. The colours represent the integrated charge in a specific area of the detector. The black circles represent the points where voltage scans for determination of the gain of the diodes was conducted.

sorption length of ≈ 1000 µm in silicon, it passes through the sensor and consequently deposits more charge as compared to the near UV laser which has an absorption length of ≈ 120 nm, as depicted in Fig. 4.11 [85]. Furthermore, it can be seen in Fig. 4.10a that the signal induced by the near UV laser has a shorter rise time than that of the IR laser after the diode has been fully depleted (V_{Dep} = 30 V). This is because the majority of the e-h-pairs are generated near the surface of the diode and consequently have wider electrostatic flux lines to induce signal on the readout, as per the Shockley-Ramo Theorem [78], and drift slower at lower reverse bias voltages. Alternatively, the signal induced by the IR laser has a longer rise time as it has e-h-pairs that are generated throughout the sensor. For the average collection time, the signal for the near UV laser induces a smaller collection time than the IR as holes that are generated are absorbed quickly near the surface of the detector, whereas for the IR case, the holes (with their slower drift velocity) have to drift from the bulk of the sensor to the multiplication side of the sensor.

To determine the gain of the diodes, the average charge deposited values, similar to the ones shown in Fig. 4.10c, were compared to that of a PIN diode to determine the relative gain of the diodes compared to the PIN.

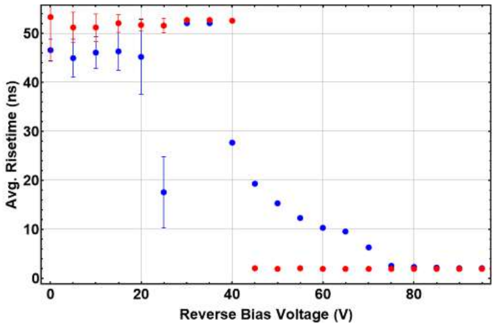

(a) Average Rise time for different applied voltages

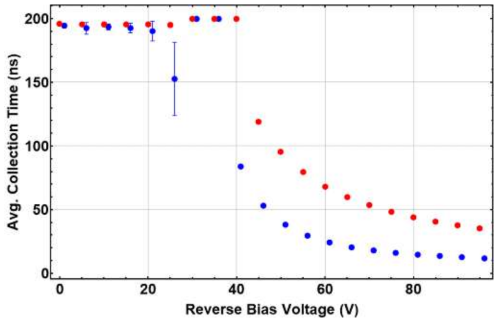

(b) Average Collection time for different applied voltages

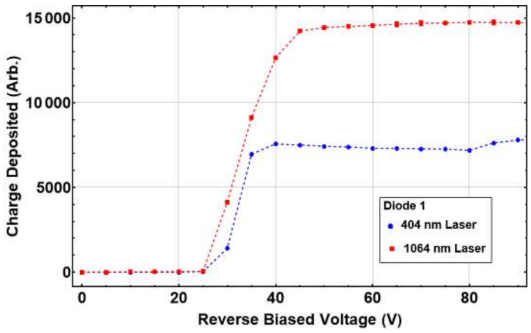

(c) Average charge deposited at different applied voltages

Figure 4.10: The averages of 20 readings of risetime, collection time and charge deposited for diode 1 at different applied reverse bias voltages taken at 20 °C. The colours represent the two different lasers used, blue for the near UV and red for the IR laser.

The measured relative gains for the three diodes are shown in Fig. 4.12. As expected, the near UV laser shows more gain compared to the IR laser because it is absorbed within the multiplication layer. Whereas, the IR laser only deposits a small part of its signal within the multiplication layer while the rest of it is deposited in the bulk of the sensor, as explained earlier. All three diodes show a relatively stable gain in the range of $11 - 19$ within error bars independent of the voltage for the near UV laser. This independence from voltage was expected as after reaching full depletion, the applied voltage only effects the drift time of the e-h-pairs, as shown in Fig. 4.10b. For the case of the IR laser, a gain of approximately $0.5 - 2$ was observed.

Temperature Dependence of Gain

The temperature dependence of the gain of the prototypes was also studied and measurements were conducted for diode 1 and the PIN diode. These measurements were done by reducing the temperature of the diode using a Peltier cooler first to 14 °C and

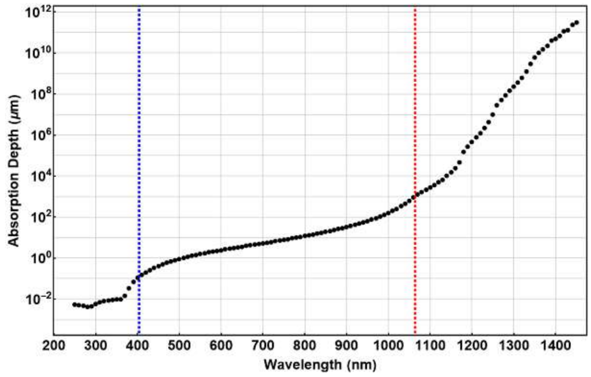

Figure 4.11: Absorption depth of different wavelenghts of light in silicon. The blue and red line represent the wavelengths of the used near UV and IR lasers respectively. Data taken from Ref. [85].

then to 10 °C while keeping all other measurement aspects the same.

Figure 4.13 shows the temperature dependence of the gain for diode 1. While the gain is constant for the IR laser, its behaviour varies for the near UV laser, where for lower temperatures the gain values are higher. This behaviour of gain dependence on temperature is expected as low temperatures cause an increase in the saturation velocities of the majority charge carries while also increasing the mean free path of the carriers and the impact ionization rate coefficient . describes the e-h-pairs generated by a solitary carrier between two collisions per unit distance travelled. This increase in coupled with the increased saturation velocities results in an increase in the gain of the sensor [**?**, 86].

One thing to note for both Figs. 4.12 and 4.13 is that for the case of the near UV laser, the error bars are significant. This is because of a lower Signal to Noise Ratio (SNR), and possible reflections from the passivation layer. For future tests, a dedicated PCB design is needed to further reduce the noise. However, for the first characterization of the prototypes of a new detector design, the tests were successful in showing that the basic theory behind the diode is correct. The characterization also helped to show that the pLGAD detector concept i.e. a detector with a thinner entrance window and a deeper multiplication layer with a collection region is possible, as both of these technologies are tested and readily available [87, 88, 89], and it is just a matter of combining them.

4.3.2 Simulation of the Signal Pulse Shape of pLGAD

To simulate the signal pulse shape of the pLGADs, modifications to Weightfield2 (WF2) [90], as suggested in [91] were employed and the simulations performed with a thin passivation layer. WF2 is a simulation software that simulates the electric field

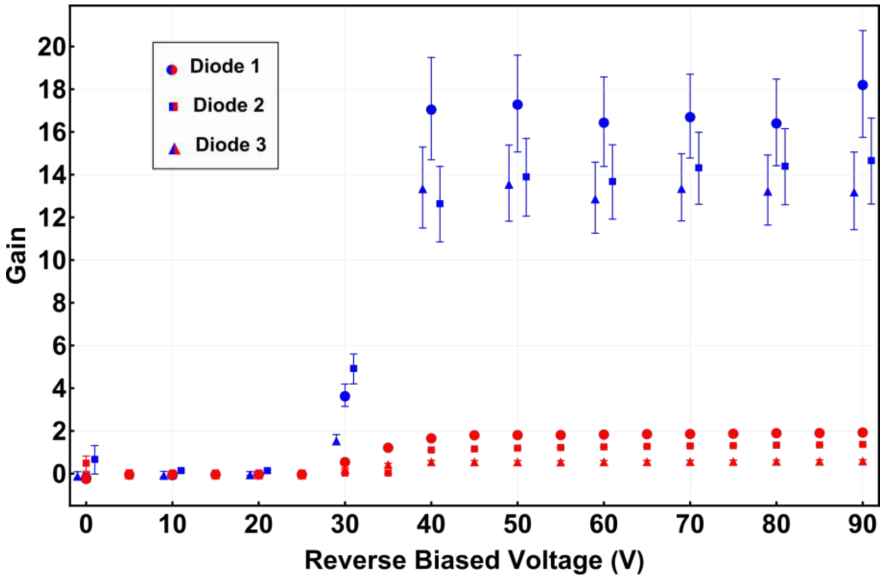

Figure 4.12: The measured gain for the 3 prototype diodes compared to a PIN diode for the near UV (blue points) and the IR (red points) laser. The points for diode 2 and 3 are shifted ±1 around the actual voltage for the case of near UV laser for the sake of clarity

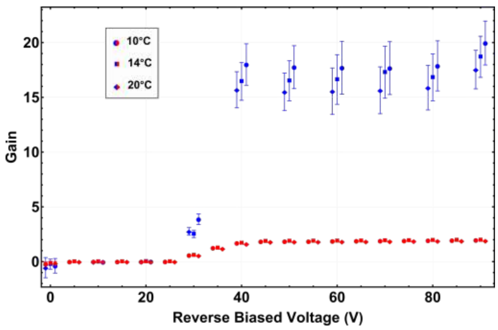

(a) Gain for different applied voltages and temperatures

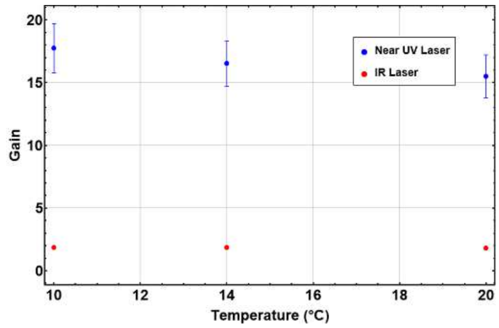

(b) Gain for different temperatures at 50 V

Figure 4.13: The temperature dependence of the gain for diode 1. The points are shifted by ±1 V for the sake of clarity.

inside silicon sensors and study their performance. The summary of the simulations settings is presented in Table 4.2.

The simulations were performed with production parameters close to the produced prototypes, but for the geometry of the pLGAD sensor instead i.e. with a thin entrance window and a collection region before the multiplication layer where low-energy protons can deposit the entirety of their charge.

Table 4.2: Parameters for the Weightfield2 simulation of the current pulses of a sample pLGAD sensor, for an incoming proton with 15 keV with normal incidence. The top section shows parameters of the sensor, and the bottom section shows parameters of the projectile proton and of the resulting 2D Gaussian e-h-pair cloud $\mathcal{N}(\mu_x, \mu_y, \sigma_x, \sigma_y)$ for normal incidence. Note that Weightfield2 does not actually simulate the projectile particle, but starts with an initial e-h-pair cloud. Hence, no parameters of the entrance window are needed, rather only the energy lost within the entrance window.

Quantity	Value
Sensor thickness	265 µm
Depletion voltage	30 V
Bias voltage	50 V
Sensing element width	300 µm
p-n-junction in a depth of	0.7 µm
Thickness of the multiplication layer	2.3 µm
Number of e-h-pairs (based on 15 keV proton)	$\approx$ 2400
μ_y (depth of cloud)	0.27 µm
μ_x (x position of cloud)	150 µm
σ_x	0.01 µm
σ_y	0.035 µm

Figure 4.14 shows the results of the simulation, with Fig. 4.14a showing the signal created by a 15 keV proton and Fig. 4.14b that of a MIP traversing through the whole sensor. Both impinging particles were with normal incidences. As discussed before, only signals close to the entrance window are amplified, therefore, for the case of a MIP, the signal resembles that of a normal silicon sensor with a slight bump being caused by the secondary electrons generated due to signal deposition near the entrance window of the pLGAD.

For the case of the proton, the signal looks different due to the multiplication layer. The peak at the start of the signal, as shown in Fig. 4.14c, is due to the generation of secondary electrons (magenta line). This peak sees a drop when the secondary electrons leave the gain layer and as the secondary holes (light blue line) are collected at the junction side. This is followed by a plateau as the secondary and primary electrons drift through the sensor towards the electrode, culminating in a peak when they get near the electrode due to the increasing strength of the weighting field and finally being collected, marking the end of the signal.

As this is a simplified simulation of the signal profile, the exact current pulse may very well be slightly different than the ones shown here as it depends on a myriad of factors ranging from the depth of the multiplication layer, the doping profile, the

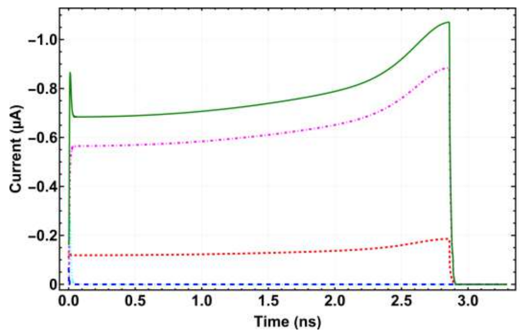

(a) Proton signal depositing 2400 e-h-pairs

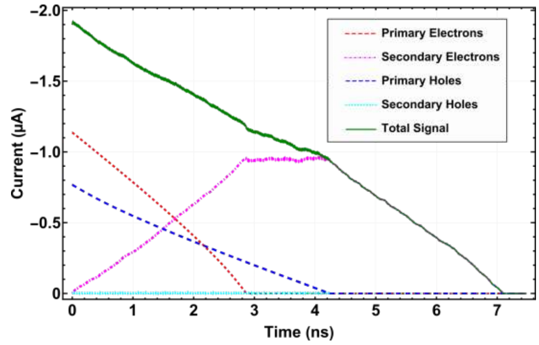

(b) MIP signal depositing 24000 e-h-pairs

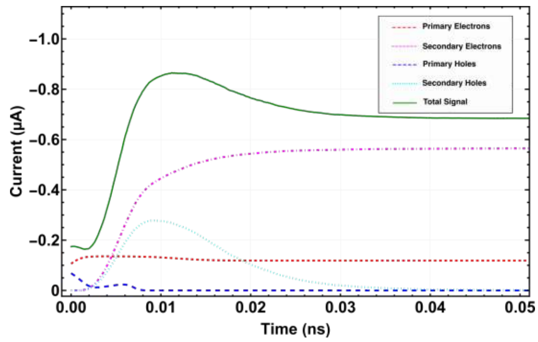

(c) Zoom of proton signal

Figure 4.14: Weightfield2 (modified) simulation results for the pLGAD sensor. For details of the modifications to Weightfield2, see text.

depth of the p-n junction, and obviously the readout electronics employed. However, the main features of the pulse, namely an initial peak followed by a plateau, should still be visible and this was observed by comparing the waveforms obtained during TCT measurements with the first prototypes.

Figure 4.15 shows the measured waveforms from diode 1 that were taken at 50 V. Even though the first prototypes had a different doping profile, depth of multiplication layer, depth of the p-n junction and addition of readout electronics i.e. a preamplifier and an amplifier, the main characteristics observed in Fig. 4.14a as compared to the waveforms obtained from the PIN diode (black waveform) can still be seen (as shown in Fig. 4.15a). It should be noted that the plateau is not as pronounced and the signal has a longer collection time. However the two-peak structure, with the first peak generated by the drift of the first e-h-pairs and the second peak being generated from the collection of the gain electrons can be seen. This dual peak structure is absent from the case of the IR laser, Fig. 4.15b, where the light passes through the sensor, and a sharper pedestal peak is generated by the drift of the first e-h-pairs followed by the gradual collection of the primary electrons at the readout. The slower drift can be

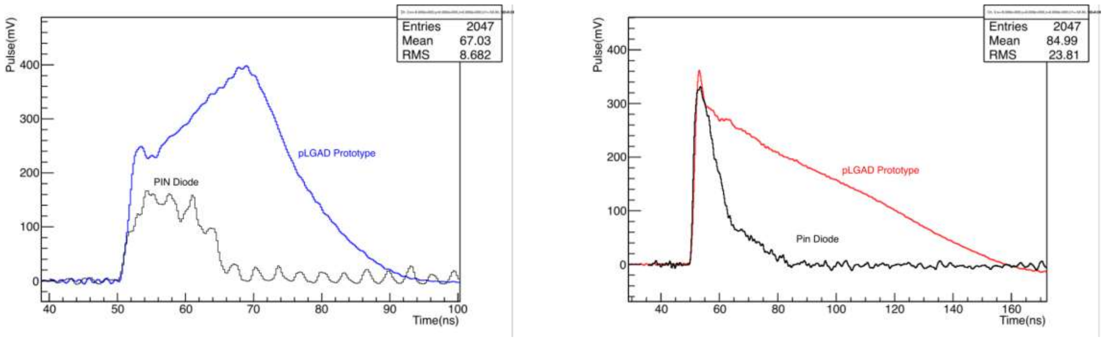

(a) Waveform from near UV laser (b) Waveform from IR laser

Figure 4.15: Waveforms taken from Diode 1 during TCT measurements at 50 V at room temperature. The signals have the same features as those observed in Fig. 4.14, with an additional peak for the IR waveform due to the absence of a collection region in the produced pLGAD prototypes. The black waveforms are those collected from the PIN diode for the same settings of the laser.

explained by the generation of some gain electrons and the difference of electric fields between the PIN diode and pLGAD prototype. It should be noted that in Fig. 4.15a, there is some sinusoidal noise in the PIN diode waveform, this is electronic noise due to the low signal to noise ratio. This noise is subtracted while integrating to ascertain the gain of the diode. It should be noted that the waveforms in Fig. 4.15 are shifted by 50 ns.

4.3.3 Advantages of the pLGAD Sensor Concept

Due to its optimized design for the detection of low-penetrating particles, the pLGAD sensor concept has many advantageous properties.

Noise behavior and background rejection As the primary signal is created near the sensor surface, the thickness of the pLGAD sensor can be chosen freely, within the limits of production technology, to adapt the pulse duration and amplitude, and the load capacitance that is seen by the readout electronics. For the case of NoMoS, the pLGAD sensor can even be made thicker (above 1.5 mm) to completely stop the impinging electrons and perform an additional spectroscopic measurement. Alternatively, a thin pLGAD (below 100 µm) can be used to allow high-energy particles such as cosmics to pass through the sensor and suppress their signal height.

Increased SNR The pLGAD is designed in a way that it only amplifies electrons, due to the chosen polarity of the gain and the bulk layer of the sensor. It has the additional advantage of having an increased SNR without multiplying the electrons created due to thermal excitations in the bulk of the sensor. This greatly reduces noise in comparison to the normal LGAD or iLGAD sensor polarity configuration that is chosen due to its radiation hardness in HEP application.

Operation at Room Temperature While a very high efficiency and an even increased SNR can be achieved by silicon sensors that store the signal charge and read it repeatedly, such as a DEPFET sensor, this however, increases the readout time. Due to the increased readout time, these sensors have to be cooled to reduce contributions from thermal excitations, i.e. leakage current, within the sensor. In contrast, the pLGAD can be operated at room temperature and still achieve high detection efficiencies (as will be discussed in Sec. 5.2) with additional cooling being an advantage for increased gain, as discussed in Section 4.3.1.

Compatibility with Usage at Multiple Post-Accelerations in NoMoS As the signal is multiplied depending on the thickness of the collection and the gain region, the pLGAD can be made to be used with multiple post-accelerations within NoMoS or similar experiments by choosing a collection region that is thick enough to stop the post-accelerated protons. This effect can be useful in studying systematic effects such as the additional $\mathbf{E} \times \mathbf{B}$ effects in NoMoS and comparing results with simulations for correction of the measured spectra.

Compatibility with Multiple Readouts The pLGAD on its ohmic side is similar to a planar sensor, therefore the detector can be realized with any desired geometries that are compatible with planar readouts, e.g. in the form of a microstrip or pixels of chosen length and width. This flexibility allows for a higher degree of freedom in the choice of the size of the pixels for NoMoS, which in the end is limited by capacitance load caused by the electrode design that goes into the calculation of the noise of the sensor.

4.4 Expected Performance of the pLGAD Sensor

4.4.1 DAQ System Requirements

The noise of a pLGAD sensor, when manufactured to the desired specifications i.e. with a thin entrance window and a collection region, can be estimated theoretically provided some assumptions regarding the DAQ system are made. The DAQ refers to the Digital Acquisition System and includes the pre-amplifier and amplifier setup to read out the signal from the pLGAD sensor. For the case of NoMoS, the requirements on the DAQ system are:

- Since the events are random in nature, the readout system has to be self-triggering i.e. whenever a signal is deposited within the detector above a certain threshold, a signal should be recorded.
- As the energy deposited by the protons is low, the DAQ system should have a low noise threshold, so the actual data acquisition threshold can be set according to requirement while ensuring the signal is well separated from the noise.
- The DAQ system should be charge sensitive, i.e. it should be able to record the signal height or if possible a sample set of the signal waveforms as well, which will allow background corrections to be applied to the data with far more ease. The ability to record the signal height will also allow rejection of background events, including cosmic events or background induced from the neutron beam.
- Lastly, due to the position sensitive requirement of the NoMoS apparatus, the DAQ should be able to handle multiple channels at once. The ability to do so will also help drive down the capacitive noise from the sensor as pixelation reduces noise compared to single strips.

4.4.2 Noise Calculation

The Equivalent Noise Charge (ENC) refers to the noise from the entire readout chain and is expressed in numbers of electrons. The contributions to ENC on a silicon planar sensor can be approximated as follows [92]:

$$ENC_J = \frac{e}{2}\sqrt{\frac{J_{\text{leak}}\cdot t_{\text{int}}}{q_e}} \approx 107\sqrt{J_{\text{leak}}\cdot t_{\text{int}}} \tag{4.3a}$$

$$ENC_C = a\psi + b\psi ENF\psi C\psi \tag{4.3b}$$

$$ENC_{R_p} = \frac{e\psi}{q_e}\sqrt{\frac{k_B T t_{\text{int}}}{2R_p}} \approx 772\sqrt{\frac{t_{\text{int}}}{R_p}} \tag{4.3c}$$

$$ENC_{R_s} = \frac{eC\psi}{q_e}\sqrt{\frac{k_B\, T\, R_s}{6\, t_{\text{int}}}} \approx 0.395\cdot C\psi\sqrt{\frac{R_s}{t_{\text{int}}}},\psi \tag{4.3d}$$

$$\tag{4.3e}$$

where ENC_J is the contribution from the leakage current, ENC_C is the capacitive load, ENC_{R_p} and ENC_{R_s} are the contribution from the parallel and series resistance respectively. The capacitive load $C\psi = C_{\text{int}} + C_{\text{back}}$ is the sum of the capacitance between the sensing elements C_{int} and the backplane capacitance C_{back}. $a\psi$ and $b\psi$ are constants that depend on the readout chip, J_{leak} represents the dark current in nA, and t_{int} is the integration time of the readout chip in µs. R_p is the parallel resistance in

MΩ, which for the case of a pixelated sensor is defined by the interpixel resistance due to the absence of a dedicated bias resistor such as those present in silicon microstrip sensors. R_s is the series line resistor in Ω. T is the temperature and k_B is the Boltzmann constant, e is the Euler number (2.718...) and q_e is the electron charge. The approximated values are the values of these contributions at room temperature with the constants plugged in. Lastly, the excess noise factor (ENF) increases the shot noise in semiconductor devices with internal amplification and applies to the series component of the capacitive noise. For the case of the pLGAD sensor, the $ENF = 2.9$, which was calculated according to [80].

When we assume that the noise sources are uncorrelated to each other, the total noise is calculated as:

$$ENC = \sqrt{ENC_I^2 + ENC_C^2 + ENC_{R_p}^2 + ENC_{R_s}^2}. \tag{4.4}$$

From the estimated value of the ENC, the minimum number of detectable primary e-h-pairs $p_{\min}$ i.e. e-h-pairs generated by the impinging particle, required to maintain an assumed SNR of 5 can be calculated as:

$$p_{\min} = ENC \frac{SNR}{\text{gain}} \tag{4.5}$$
$$= \frac{ENC}{3}, \tag{4.6}$$

where the value of gain is set to the average of 15 obtained at room temperature of the three diodes and a SNR of 5 is assumed to obtain a 5-sigma significance of the detection.

The pLGAD sensor can then be paired with three combinations of sensor layout and electronics and by using Eq. (4.4) and Eq. (4.5) the minimum number of primary e-h-pairs for the following three combination of sensor and readout was calculated:

1. AliVata Readout: For simple, small sensors, similar to the diodes albeit with a much thinner passivation layer in front, the AliVata's VATAGP7 readout chip [93] could be connected with the electrode of the sensor with a wire bond, similar to the PCB setup shown during the course of this work.

2. Pixelated NoMoS sensor with Timepix3 [94] readout: The Timepix3 could be connected to the customized layout of the pixelated NoMoS sensor, with at least 64×32 pixels of size $0.33 \times 1.6\,\mathrm{mm}^2$ for the superconducting or $1.3 \times 2.2\,\mathrm{mm}^2$ for the normal conducting case, via the help of a second metal layer.

3. Pixelated sensor with Timepix3 native layout: The NoMoS drift detector is instead made to match the native layout of the Timepix3 chip and no additional routing lines are required.

With these assumptions, the ENC contributions result in the estimates listed in Table 4.3 as a best-case approximation with a pLGAD that has a gain of 10. The detection thresholds which are under 50, are not possible due to Timepix3's self-triggering threshold of 500 electrons [95]. Therefore, for NoMoS, these thresholds are automatically moved to 50 electrons. Another fact to note is that for the Normal Conducting (NC) and Super Conducting cases of NoMoS, the stated threshold values can even go lower if a standard 300 µm wafer is used instead of the 2 mm wafer thickness assumed here. This assumption was made to allow for the spectroscopic measurements of the electrons by having them stop within the sensor material. It should be noted that these values are a bit abstract and may change due to noise stemming from external sources e.g. interference from the post-acceleration electrode. Therefore, to exploit the full capabilities of the pLGAD sensor, more effort has to go into the design of a potential DAQ system. In an ideal case, a DAQ with the aforementioned random sampling to compare with Monte Carlo studies for background rejection would be the best case scenario. Another thing to keep in mind is the DAQs ability to handle signals from both the electrons and the protons, which can be accomplished by using a similar DAQ strategy to that of *a*SPECT [10][96].

Table 4.3: Equivalent Noise Charge (ENC) contributions for three variants of pLGAD detection systems, all values are in electrons. Note that the Timepix3 chip has a self-triggering threshold of 500 electrons [95], so the detection thresholds calculated here can only be achieved with external triggering. Therefore, for NoMoS, in this case the detection threshold is limited to above 50 electrons, assuming a gain of 10 and a pLGAD connected to a self-triggered Timepix3 chip.

Parameter	Single channel	NoMoS_{NC}	NoMoS_{SC}	Timepix3 native
ENC_{C}	603.9	62.0	62.0	62.0
ENC_{J}	264.2	234.27	98.41	3.2
$ENC_{R_{\text{P}}}$	17.3	17.3	17.3	17.3
$ENC_{R_{\text{S}}}$	61.7	0.84	0.15	0.01
Quadratic sum ENC	662.3	242.9	117.6	64.4
Detection threshold p_{min}	221	81	40	22

Ultimately, this may be beyond the capabilities of an off the shelf DAQ and may require a special ASIC setup.

4.4.3 Comparison with Other Detector Technologies

Even though the pLGAD sensor fulfils the criteria required by the NoMoS experiment, there are two other established silicon based detector technologies which have comparable properties, namely the DEPFET sensors and the Silicon Drift Detectors (SDDs). Therefore, those technologies will be briefly discussed here and compared to the pLGAD detector concept. Both technologies are well established and can be operated in a fully-depleted state, with an unstructured, and a very thin entrance window in the order of 10s of nm for impinging particles.

Before finally deciding to use the pLGAD detector concept, both the DEPFET and SDD were in contention for use as the main drift detector within the experiment. The charge collection efficiency of a DEPFET sensor was even used to model the simulated response of a pLGAD sensor's efficiency, as discussed in Sec. 5.2. Reportedly, a DEPFET sensor can reach a detection threshold of below 30 electrons if cooled down to $-50°$. Alternatively, the DEPFET sensors can also detect single signal electrons by using correlated double-sampling and repetitive non-destructive readout to reduce noise [97]. However, this requires a bigger window of time between two signals which the NoMoS concept does not allow. An additional benefit of the pLGAD concept is its ability to achieve a good SNR of 5 with only 50 electrons without requiring additional cooling.

Both the DEPFET and SDD technologies also come with their own complications. For example, the DEPFET sensor requires at least 7 (5 for the SDD) different operation voltages. Both of the sensors benefit immensely from additional cooling and often specific pre-amplifiers or readout chips for the technologies are required. Lastly, the biggest point in the favour of the pLGAD concept was its cheaper price point compared to the DEPFET or the SDD sensors. As in its essence, the pLGAD is a silicon planar sensor, it means that it is cheaper to produce, can work with commercial readout systems designed for planar sensors, only requires one operating voltage and can be operated at room temperature with a reasonable SNR while still offering competitive efficiency (discussed in Chapter 5). Due to these reasons, the pLGAD sensor concept was ultimately chosen as the main drift detector technology for the case of NoMoS.

4.5 Potential Other Applications

As the pLGAD is a new sensor concept, this section briefly talks about further applications of the concept outside the scope of NoMoS. Some potential pLGAD applications are:

- Monitoring of low-energy beam lines with high detection efficiency instead of MCPs that suffer from uniformity issues and also have a smaller efficiency than that of a pLGAD. Thus usage of pLGAD will result in more accurate beam-line monitoring and reconstruction of beam profile.
- Low-energy spectroscopy experiments that require high energy resolution. These experiments can benefit from the introduced collection region of the pLGAD

and change it to suit the needs of their experiment to conduct low-energy spectroscopy on a detector with linear gain.

- Experiments for the detection of soft X-rays or neutrons, albeit a conversion layer in front of the sensor instead of a passivation layer may be required. In this case, the efficiency of the pLGAD may be bottle necked by the efficiency of the conversion layer.

- Time of flight (TOF) experiments with high time resolution, e.g. Time of Flight Position Emission Tomography (TOF PET) for imaging. As the pLGAD sensor uses electrons as its majority charge carriers, the signal from it will be faster than traditional silicon sensors which use holes as their majority charge carriers.

In general, the pLGAD could be used in many cases instead of a MCP, scintillating fiber, SiPM arrays and photosensitive foil technologies, with better spatial resolution. This holds especially true for low-energy environments where a Geiger avalanche for detection of impinging particles is not required.

Chapter 5

Channeling in Silicon Sensors

Since NoMoS is a precision experiment, detailed simulation studies are required to, inter alia, understand the detector response. This is especially important for the case of low-energy protons, which even after post-acceleration have a maximum kinetic energy of $\approx 15\,\mathrm{keV}$. Due to their low energy, protons are susceptible to some additional effects such as channeling. Channeling is a solid state effect that arises when a charged particle is guided through an open channel of a crystal lattice.

This is the first investigation of effects of channeling in a silicon detector within the neutron beta decay community with results being compared to those achieved by the conventionally employed software within the community [98, 10] SRIM (The Stopping and Range of Ions in Matter) [99, 100]. The results of my investigation led to the discovery of a potential oversight of channeling as a source of systematic error within the neutron beta decay community. Taking this systematic effect into account, a detailed simulation study of the efficiency of silicon sensors with different passivation layers at different angles and energies of interest was performed. These simulations result in an efficiency of $\approx 99.9\%$ for the proposed NoMoS detection system. The studies also lead to an acceptable uncertainty in the thickness of the passivation on top of the sensor of $1\,\mathrm{nm}$.

Furthermore, by performing simulation studies similar to those done for backscattering correction in beam experiments for the determination of neutron lifetime, channeling could help bridge the gap in solving the beam versus bottle neutron lifetime puzzle [101, 40].

5.1 Introduction to Channeling

Due to the crystalline structure of silicon, the assumption that the impact parameter distribution is independent of the relative orientation of the target to the beam direction is not valid any more. In such cases, the orientation of the beam to the target

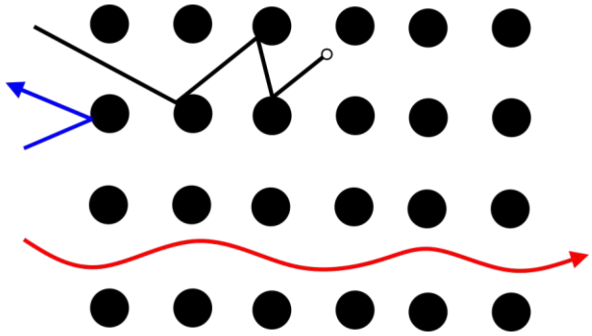

Figure 5.1: Schematic representation of a crystalline lattice. The red line shows a channelled particle, whereas the blue and black lines represent a backscattered particle and one that enters the crystal at an angle to the normal of the crystal surface and deposits its entire energy within the crystal respectively.

is of paramount importance. This is because charge particles moving nearly parallel to a crystal's major axis or plane can be steered down the open channels between the planes of atoms. This so called "channeling effect" affects the overall trajectory of the impinging particle and consequently the overall rate of backscattered particles [102, 103, 104]. A schematic representation of channeling can be seen in Fig. 5.1.

Also due to channeling, ions or in the case of free neutron beta decay, protons see a reduction in the energy loss per unit path length that contributes to increased ion ranges within the crystalline material [105]. Consequently, protons that penetrate deeper into the material can liberate more e-h-pairs which have a lower probability to recombine.

Within the context of this work, the case of protons for channeling will be discussed in detail. Note that for electrons, these effects are suppressed. For electrons with high energy, channeling effects are less likely to occur due to the small angle required for axial channeling. To understand this, the classical Lindhard case of axial channeling in a continuum potential can be considered i.e. a potential averaged over a direction parallel to a plane or a row that can be used in lieu of the actual periodic potential of the row or plane of the crystal [106]. In this case, the critical angle, the angle cutoff below which channeling effects can take place is dependent on energy by:

$$_{crit} \propto E^{-\frac{1}{2}}. \tag{5.1}$$

For particles with energy greater than 100 keV the critical angle is smaller than 1° and the assumption of treating the crystalline silicon structure as amorphous is valid as there are very few electrons which will hit the detector with such a low angle. For the case of low-energy electrons $T_e <$ 100 keV channeling effects can take place and actually form the basis for a SEM (Scanning Electron Microscope) called Electron Channeling Contrast Imaging (ECCI) where samples are placed almost normal to the impinging beam of electrons [107]. However, due to the negative charge of electrons and their smaller mass, they are easily "dechanneled" compared to protons, in the order of a few nm, within the energy range of interest [108].

Within the context of this thesis, a Binary Collision Algorithm (BCA) was used instead of a molecular dynamics approach, as studies have shown that a properly written BCA software can provide similar results as a Molecular Dynamics (MD) simulation down to 10 eV [109]. This corresponds to 2 e-h-pairs in Silicon and consequently can be safely ignored without compromising the overall detector efficiency calculation. Furthermore, IMSIL [110, 111], the BCA software utilized for this purpose, had a considerable speed advantage and ease of execution compared to a MD simulation software.

Even though channeling is a well known process, the validation of the chosen software compared to literature as well as to the conventionally used software within the neutron beta decay community called SRIM, which does not take effects such as channeling into account, was still performed to understand the importance of channeling and the role of the passivation layer in front of the detector.

5.1.1 Simulation Setup

Electronic energy loss in channels within a crystal is described in IMSIL by a model which combines the Lindhard stopping power [112] and an impact parameter dependent contribution according to Oen and Robinson [110]. The parameters of this model for protons in silicon as determined in [111] were used. These parameters were extracted by the author of the software after calibrating IMSIL by comparing the range profiles of H in Si at the energy range of 10, 40, and 100 keV obtained from Secondary Ion Mass Spectrometry (SIMS) with those obtained from the software.

For the case of amorphous targets, only the correction factor k_{corr} to the Lindhard stopping power [113] given by Eq. (5.2) was changed.

$$-\frac{dE}{dR} = NkE^{\frac{1}{2}}, \tag{5.2}$$

where

$$k = k_{corr}\frac{1.212 Z_1^{\frac{7}{6}} Z_2}{(Z_1^{\frac{2}{3}} + Z_2^{\frac{2}{3}})^{\frac{3}{2}} M_1^{\frac{1}{2}}} \mathrm{eV}^{\frac{1}{2}} \mathring{\mathrm{A}}^2, \tag{5.3}$$

and $-\frac{dE}{dR}$ is the electronic energy loss by the particles within an amorphous material, N the atomic density of the target, Z_2 the atomic number of the target atoms, and Z_1 and, M_1 the atomic number and mass of the impinging ions.

The parameter k_{corr} was determined for each individual material of the passivation layer in front of the supposed silicon sensor by matching the electronic energy loss at 1 keV to the PSTAR database [114]. For cases, where the amorphous material was not listed on the PSTAR database, the electronic energy loss was instead matched to that of a 10 keV proton impinging on the same material in SRIM. The choice of using two different correction parameters was done as SRIM uses an electronic energy loss model considering the electronic energy loss $S_e \propto E^p$ where often for low energy cases $p \neq 0.5$. This is in contrast to the Lindhard stopping power which uses $S_e \propto E^{1/2}$ and it is important that these stopping power fits are done in the energy regime of interest.

Lastly, in amorphous regions the lower limit to the maximum impact parameter, which is the maximum value of the impact parameter for a collision to occur, was set to 2.7 Å. The value was chosen by comparing the overall computation time, and comparing the overall backscattering rates obtained by increasing and decreasing the parameter. A small value for this parameter was decided on, at the cost of overall computation time, to increase the accuracy of the proton interactions within the amorphous regions.

For a first order approximation of the sensor, a two-layer structure with a silicon crystal and an amorphous passivation layer was chosen. The choice of the passivation layer was investigated by using what has already been used in detectors within the neutron beta decay community i.e. SiO_2 of a few nanometers in N*ab* [77], and Al of a thickness of 30 nm by *a*SPECT [10]. This was further compared with a passivation layer of Al_2O_3 realized with a thickness of 1 nm via Atomic Layer Deposition techniques (ALD), according to the manufacturers of the pLGAD (IMB-CNM-CSIC).

For the orientation of the crystalline silicon, the crystal was chosen with a (100) surface, and [001] reference direction within the surface. This choice was one of the three possible crystalline choices of silicon with (110) and (111) surfaces being the other two. Even though the (111) surface has the largest interatomic distance, and is theoretically susceptible to more channeling effects, the choice of a (100) surface was sufficient to highlight the differences caused in detector backscattering and efficiency caused by having a crystalline structure as opposed to an amorphous one. A reference file for one of the IMSIL simulations with the relevant comments can be found in Appendix B.

For the case of SRIM, the backscattering model was set to the sputtering model for accurate description of ion backscattering after investigation under my co-supervision [67].

5.1.2 Verification of IMSIL Results

In order to verify that IMSIL is indeed capable of modelling different crystalline planes and axis, and consequently the effects of channeling, a basic simulation of a silicon crystal with the aforementioned change in the maximum impact parameter and the modified electronic energy loss model was performed with 10 keV protons. The angle of the impinging protons was varied from 0 to 90° in steps of 2° in both the polar and azimuthal axis. These axes define how the beam of impinging protons strike the target material. This allowed the comparison of the ranges of the impinging protons with those shown in literature [115] (see Fig. 5.2)

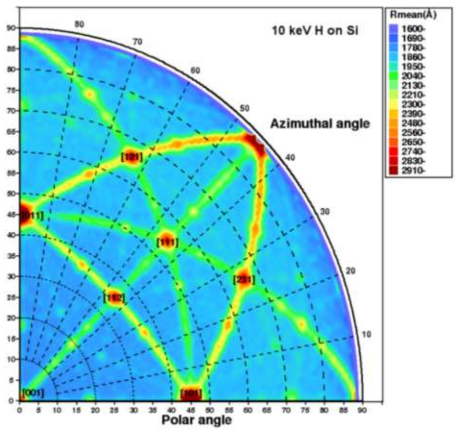

(a) MD (Molecular Dynamics) simulated result for 10 keV H ions impinging on Si. Taken from [115]

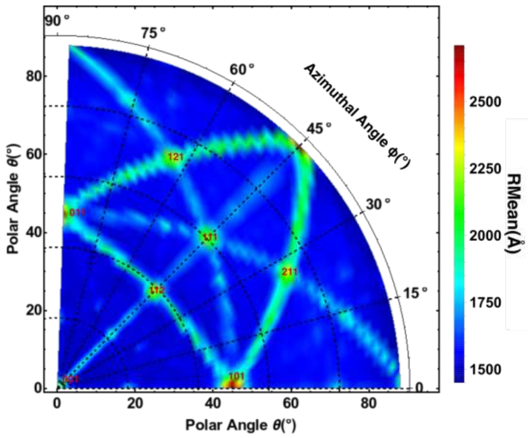

(b) IMSIL simulated result for 500,000 10 keV H ions impinging on Si

Figure 5.2: Comparison of simulated mean range of 10 keV H ions impinging on Si from IMSIL (a Binary Collision Algorithm software used in the framework of this thesis) with published literature values [115] for the verification of the BCA approach over an MD approach.

As it can be seen from in Fig.5.2, IMSIL shows similar mean ranges of H ions impinging upon a [001] crystal surface normal when compared to that taken from literature. The impinging beam sees different crystalline planes and axis as the polar and azimuthal angle changes, with very strong channeling effects being observed in the <110> channels. The critical angle for all of these channels varies slightly as apart from the energy of the impinging particle, it also depends directly on the interplanar distance between the Si atoms. It is important to note that for this comparison, the mean range in both cases was not defined as vertical to the surface, but by projection to the initial direction of the ions. Nonetheless, the excellent agreement of IMSIL with MDRange (the molecular dynamics software used in literature), and the clear visibility of different channels reaffirmed the choice of IMSIL for investigating channeling effects of low-energy protons in silicon.

5.1.3 Comparison of SRIM and IMSIL

Difference in Backscattering Rate

To understand the detector response, one of the quantities that is often studied in detail in neutron beta decay experiments, whether for lifetime [98] or for the electron-antineutrino correlation coefficient a measurement [10, 116] is the overall backscattering rate of the impinging particles. The knowledge of the backscattering rate is then used to correct the measured spectrum by either extrapolating the overall backscattering to 0 for the case of the neutron lifetime or by performing further simulations to correct for double hits and signal loss by backscattered protons in the case of the electron-antineutrino correlation coefficient measurements.

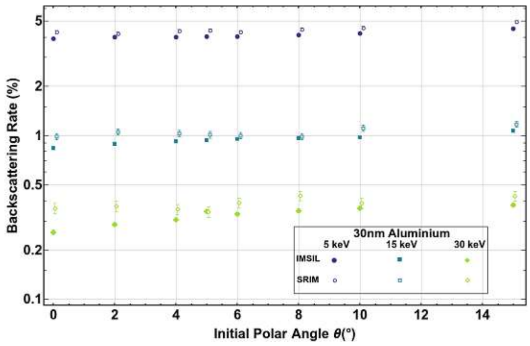

(a) 30 nm Al

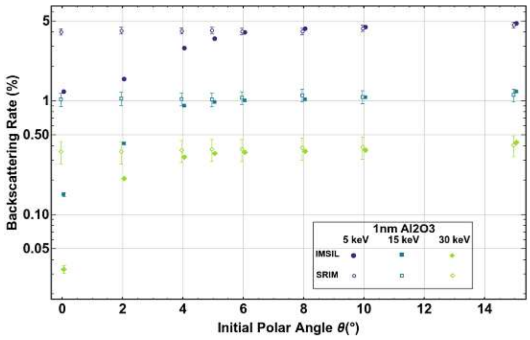

(b) 1 nm Al_2O_3

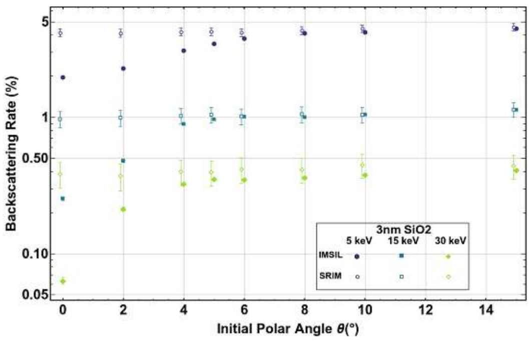

(c) 3 nm SiO_2

Figure 5.3: Comparison of backscattering rates in Log scale when channeling is taken into account (IMSIL) versus when it is ignored (SRIM) for protons impinging upon silicon sensors with different passivation layers. The simulations were performed with the azimuthal angle ϕ averaged over in the case of IMSIL. Note that the points for SRIM are shifted by 0.25° for the sake of clarity.

Figure 5.3 shows the comparison of backscattering rates obtained via simulations conducted using SRIM, what is conventionally employed, versus IMSIL to highlight the difference of the backscattering rates when the crystalline structure of silicon is taken into account. The simulations were performed for 500000 particles for the case of IMSIL and 50000 for SRIM and plotted with statistical error bars. As SRIM can only model amorphous solids, simulations performed via IMSIL were done with the azimuthal angle ϕ averaged from 0° to 360°. The simulations were performed to a maximum impinging polar angle θ_0 of 15°, as due to the post-acceleration of the protons within NoMoS, the maximum angle at the detector $\theta_{\max}$ is reduced from the nominal value of 45° (highest angle allowed from the filter). The relation of kinetic energy T_0 and impinging polar angle θ_0 at the decay versus T_{Det} and θ_{Det} due to post acceleration is given by:

$$\begin{aligned} T_{\mathrm{Det}} &= (T_0 - eU_{\text{post-acc}}) \\ \theta_{\mathrm{Det}} &= \arcsin\left(\sqrt{\frac{B_{\mathrm{Det}}}{B_0} \cdot \frac{T_0 \sin{\theta_0}^2}{T_{\mathrm{Det}}}}\right) \end{aligned} \tag{5.4}$$

where B_0 and B_{Det} are the magnetic fields at the decay and detector respectively, $U_{\text{post-acc}}$ is the applied post acceleration voltage, and T_0 and T_{Det} are the kinetic energy of the proton at decay and the detector respectively.

For the case of NoMoS, the maximum angle at the detector would be ≈ 10° for a post-acceleration of 15 keV.

As it can be seen in Fig. 5.3, for small angles, i.e. $\theta < 5°$ or smaller, a clear deviation between SRIM and IMSIL is observed due to the effects of the crystal structure on the backscattering rate. This deviation depends on the kinetic energy of the impinging protons as well as on the thickness of the passivation/conducting layer. It can be seen that the discrepancy in backscattering rate increases with increasing energy at constant passivation layer thickness. While it is true that the critical angle ψ_{crit} of a crystal is inversely proportional to the square root of the initial energy of the particle, at the same time the beam spread due to multiple scattering in the passivation layer is reduced with increasing energy. This can be seen in Fig. 5.4, which shows the beam spread of the protons after passing through a 30 nm Al conduction layer i.e. just before hitting the active area of the sensor. The beam spread increases as the energy is lowered, see Fig. 5.4a, while having the peak i.e. the most probable value, skewed towards the initial impact angle. Moreover, the critical approach distance r_{crit} decreases as the energy is increased. r_{crit} is the minimum distance from a row or plane of atoms required so that channeling is possible [105]. This leads to a larger fraction of channeled protons if the amorphous layer is absent. The aforementioned simulations show that the latter effects i.e. beam spread and r_{crit} dominate over ψ_{crit}.

The effect of the thickness of the dead layer or passivation layer on proton channeling can be seen more explicitly in Fig. 5.5, which shows the effects of the dead layer thickness on the backscattering rate of protons of varying energies, on a logarithmic scale, impinging upon the detector at 0° with the azimuthal angle averaged over. The data point at 0 degree in all three graphs, represents the backscattering rate of a pure silicon crystal without a passivation or a conduction layer in front. It can be seen that when the thickness of the amorphous layer decreases, due to a decrease in the beam spread after passing through the layer, more protons undergo channeling and as a

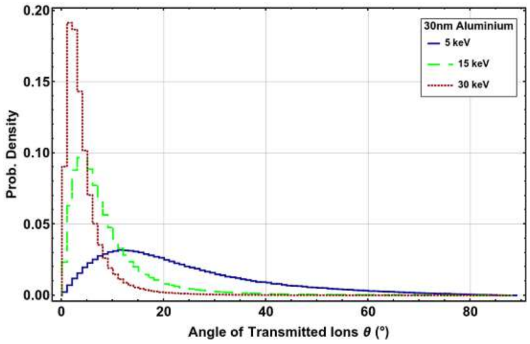

(a) Beam spread after protons of various energies pass through the 30 nm Al with an initial angle θ of 0°

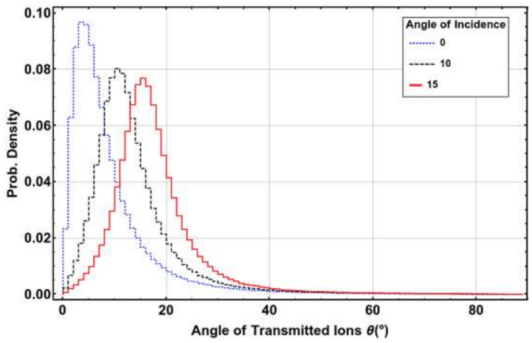

(b) Beam spread after protons of various angles pass through the 30 nm Al with an initial energy of 15 keV

Figure 5.4: The beam spread after protons impinging the detector at different energies and angles pass through a 30 nm of Al conduction layer in front of the detector.

consequence a lower backscattering yield is achieved. Therefore, for any detector with a thin amorphous layer, e.g. 1 nm of Al_2O_3 for NoMoS or 3 nm of SiO_2 for N*ab*, the backscattering rate is severely reduced due to channeling effects and the uncertainty in the thickness of the passivation layer justifies a further detailed investigation especially when either correcting the measured data for backscattering or when ascertaining the efficiency of the detector in NoMoS.

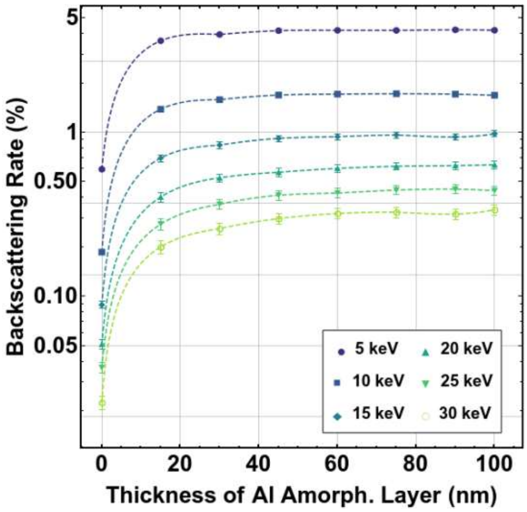

(a) Al

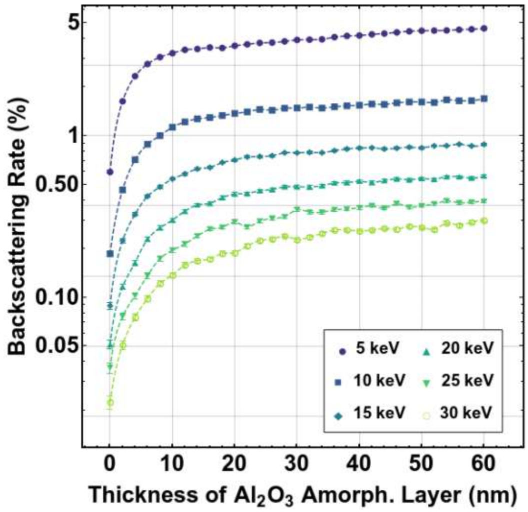

(b) Al_2O_3

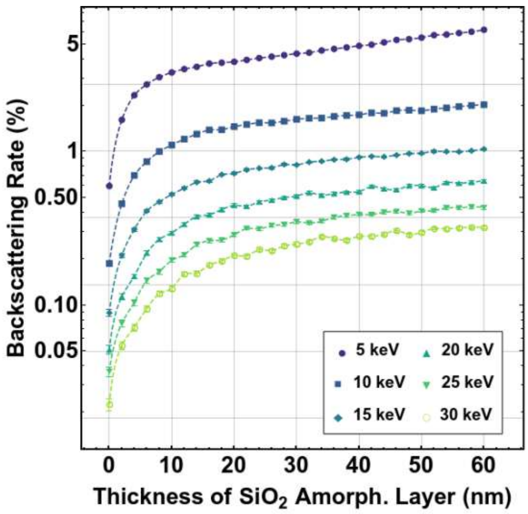

(c) SiO_2

Figure 5.5: Logarithmic plots of the dependence of the backscattering rate of protons of varying energies on the thickness of the dead layer in front of the detector when impinging normal to the sensor surface. Due to the convolution of multiple scattering, especially at lower energies or thicker dead layers, taking place in the amorphous layer, the effects of channeling are diminished at lower energies or thicker dead layers. However, at higher energies and thinner layers, these effects are more pronounced by the dip seen in the start of the graph. The left most point in all graphs represents backscattering rate from crystalline silicon without any amorphous layer in front. The connecting lines are just Hermite interpolations between the data points.

Difference in Ionizing Energy Loss

To further investigate the effects of channeling on protons, IMSIL was modified to output the average ionization energy lost by the impinging particles as a function of the penetration depth. Using this information to the number of e-h-pairs generated within the sensor could be derived and consequently compared to that obtained from SRIM to further gauge the effect of channeling on the detector efficiency in neutron beta decay experiments in general and NoMoS in particular.

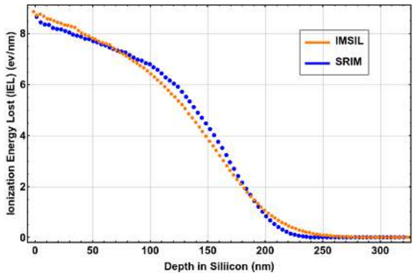

(a) Al 30 nm

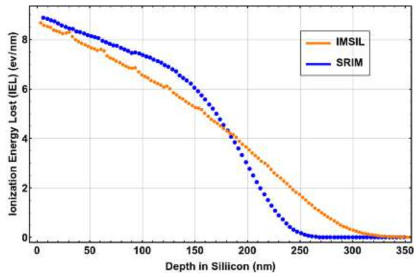

(b) Al_2O_3 1 nm

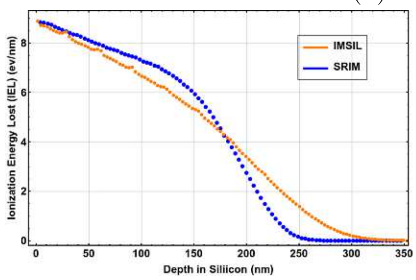

(c) SiO_2 3 nm

Figure 5.6: The average ionization energy lost as a function of the penetration depth of the impinging particles (15 keV at 0°) on silicon sensors with various dead layers obtained from IMSIL and SRIM. The ionization energy loss profile changes slightly due to channeling as the passivation layers get thinner.

Figure 5.6 shows the average ionization energy lost (IEL) by 15 keV protons impinging on silicon sensors with different dead layers in front of the active detector area at 0° from both IMSIL and SRIM. While the IEL profiles for 30 nm Al are similar for IMSIL and SRIM, see Fig. 5.6a, they vary quite significantly for the case of the thin passivation layers of SiO_2 and Al_2O_3, where the channeling effects are strong, as seen previously for the case of the backscattering yield in Fig. 5.3. Another important thing to note is how the range of particles in silicon varies due to channeling effects. This is an important observation as the probability of recombination of generated e-h-pairs, referred to as the Charge Collection Efficiency (CCE) (see Sec. 4.1.1), gets smaller the deeper the impinging particle penetrates in the active detector area, as shown before in Fig. 4.1. Similar observations can be made for other energy and angle combinations of the impinging particles, as those observed in Fig. 5.3 i.e. the IEL profile will vary between the two programs when channeling effects for that particular combination are observed.

Difference in Detector Efficiency

Due to the difference of ionization energy lost in thin passivation layers, it is evident that the efficiency of the detector will also change if channeling is taken into account. To investigate this, IMSIL was further modified to output the overall track information of the impinging protons. Doing so enabled the determination of the efficiency of the detector by calculating the overall detectable e-h-pairs generated by each impinging particle within the sensor.

Calculation of Detector Efficiency The efficiency of a detector depends upon: the passivation layer, the charge collection efficiency of the detector, the properties of the impinging particles, and the total Equivalent Noise Charge (ENC_{Total}). Hence, to compare efficiencies when channeling is taken into account versus when it is ignored, some assumptions were made in order to conserve computation time. These assumptions are as follows:

1. The charge collection efficiency of a DEPFET (DEPleted p-channel Field Effect Transistor) detector that was made available courtesy of P. Lechner from MPG-HLL (The Halbleiterlabor of the Max Planck Society, Munich, Germany) was used [74].

2. The passivation layer of the N$ab\not{}$detector was chosen i.e. 3 nm of SiO_2 as it is an existing detector (whose CCE is unknown) and would be the case of a natural oxide formation on top of a silicon detector if there was no passivation layer at the time of manufacturing.

3. The scenario where channeling is the strongest for the angular range of neutron beta decay experiments that aim to measure the parameter a, i.e. $0°$, was simulated for various energies.

Protons with energies of 5 keV, 15 keV, and 30 keV were simulated from both IMSIL and SRIM and the data was analysed for each individual track using the logic shown in Fig. 5.7.

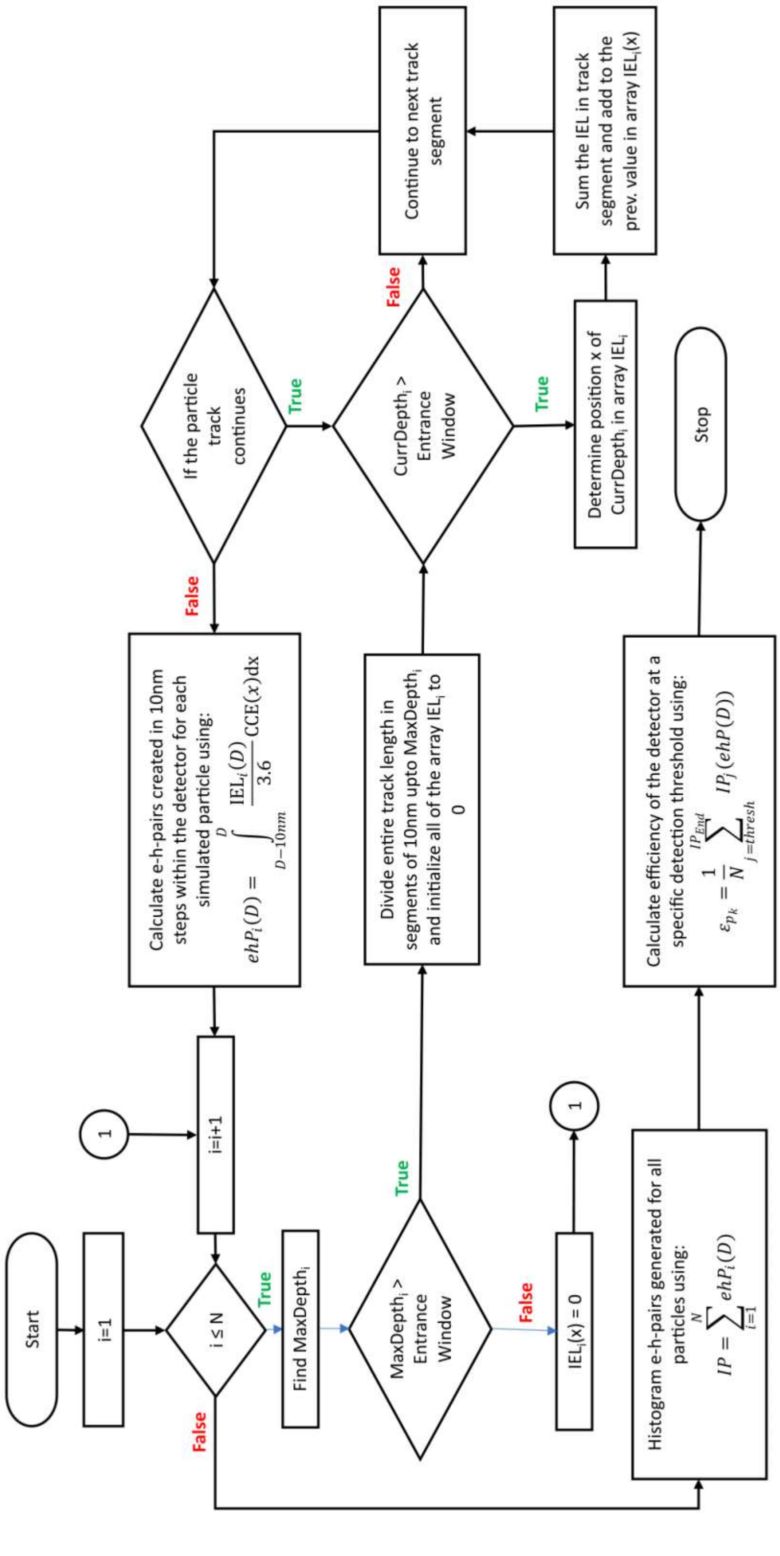

Figure 5.7: Flowchart for the calculation of the detector efficiency, where N is the total number of simulated protons, D is the depth in silicon, and i represents the ith particle.

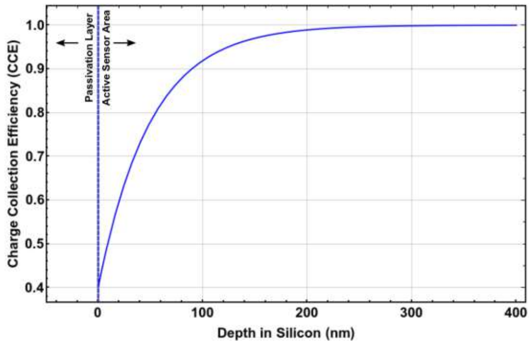

(a) Exemplary CCE with measured values for a DEPFET sensor

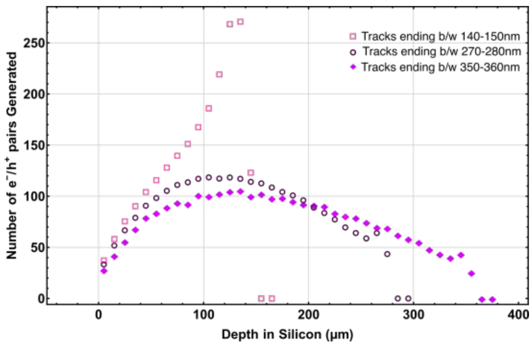

(b) Generated e-h-pairs after convolution with the CCE(x) obtained by averaging 50 tracks that end at various points within the active silicon sensor

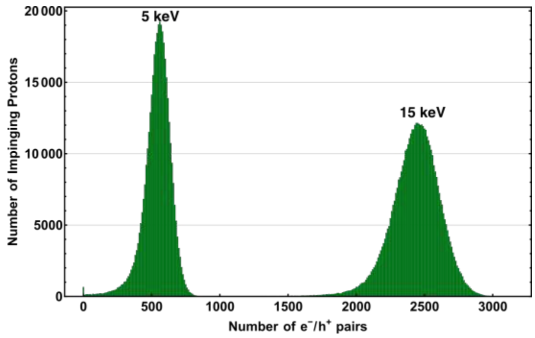

(c) Histogram of the number of e-h-pairs generated by 500,000 protons each at two different energies

Figure 5.8: Results of different steps within the efficiency calculation procedure. Convolution of the CCE with the IEL by a particle within the sensor leads to Fig. 5.8b, which when histogramed for all the generated e-h-pairs results in Fig. 5.8c.

In descriptive form, the efficiency of a detector under the aforementioned conditions was calculated by analysing the tracks of N number of particles individually within the detector. For each particle track, the number of e-h-pairs generated within the active silicon area was calculated in intervals of 10 nm depth within the sensor. For each interval the total Ionizing Energy Lost (IEL) within that bin was divided by 3.6 eV, which is the energy required to generate one e-h-pair by a particle within silicon, and multiplied with the integral of CCE of that bin. The integral of the CCE could be calculated analytically as it is given by the formula (for a DEPFET sensor):

$$CCE(x) = 1 - \quad e^{-\frac{x}{\tau}}, \tag{5.5}$$

where x is the depth of the particle within the active part of the sensor, and the parameters as well as τ were derived from experimentally measured data for a

DEPFET detector with $\tau/$having the dimensions of length.

An example of the detectable e-h-pairs within the sensor can be seen in Fig. 5.8b, which shows the averages of 50 tracks each that end at various points within the sensor. For example, the empty square data points represent 50 tracks of particles that came to a stop at 140 to 150 nm within the sensor. The detectable e-h-pairs data is then histogramed, as shown in Fig. 5.8c. It should be noted that protons that are in the 0th bin are those which do not leave any signal within the active part of the sensor and are backscattered from the dead layer of the detector instead. From this the efficiency of the detector can be calculated for an reasonable threshold value where the signal to noise ratio is favourable i.e. the overall expected noise is lower than the generated signal usually by a factor of 5 or more, by summing over the number of protons from the threshold value until the last bin and then dividing by the total number of simulated protons N. The threshold noise value depends on the Data Acquisition (DAQ) system as well as properties of the detector itself and a desired signal to noise ratio (SNR) for separation of noise from the actual signal, as explained earlier in Sec. 4.4.2. For the case of a superconducting NoMoS, this value is set to 50 e-h-pairs.

Repeating the aforementioned procedure for both IMSIL and SRIM results in Fig. 5.9. The figure shows a Log-Log plot of efficiency or rather the amount of signal lost (100-Efficiency)% for a specific detection threshold value for a silicon detector with 3 nm passivation layer of SiO_2 for protons impinging upon the sensor at 0°.

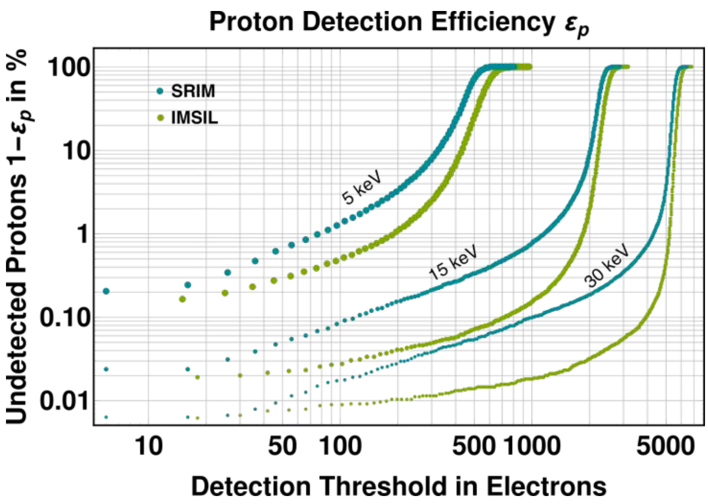

Figure 5.9: A Log-Log plot for the comparison of detection efficiencies obtained from SRIM and IMSIL for protons with varying energies impinging at 0° upon a silicon sensor with 3 nm passivation layer of SiO_2. The y-axis on the plot shows the amount of signal lost at a specific threshold value of generated e-h-pairs required to separate the noise from the signal.

As expected, depending on the impact energy of the protons, there is a significant difference in the efficiency of a silicon sensor if channeling is taken into account or not. This difference increases at higher values of the detection threshold for all energies where due to the smaller range within the sensor, SRIM gives a lower value of the threshold at which all signal is lost compared to IMSIL. Nonetheless, the so called "lower value of the threshold" is relative for the post-acceleration voltage, and the detector geometry of an experiment.

5.1.4 Dependence of Channeling on Azimuthal Angle

As discussed earlier, channeling also has a dependence on the azimuthal angle of the impinging particle as a particle can undergo both axial and planar channeling effects. However, for amorphous materials this extra angular dimension can be ignored as in that case a particle's interactions only depends on the polar angle relative to the normal of the material. Therefore programs such as SRIM do not even provide the users an option to vary the azimuthal angle, which on the other hand is relatively important for software such as IMSIL that take channeling effects into account. Up till now all simulations shown in the course of this work, with the exception of the one which was done for verifying the validity of IMSIL with published values of average penetration range of H ions in silicon, were performed with the azimuthal angle uniformally distributed and averaged over i.e. to make the simulations comparable with those obtained from SRIM. However, it can be seen that the backscattering rate varies relative to the other channels in the silicon crystal. Therefore, investigations were performed for a polar angle θ range of 0° to 20° in steps of 2° and an azimuthal angle ϕ range of 0° to 90° in steps of 2°, because the silicon crystal is cubically symmetric, to quantify how big the differences in backscattering could be within the context of a neutron beta decay experiment.

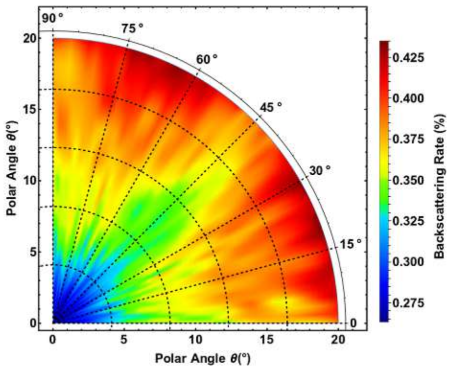

(a) 30 keV protons impinging on 30 nm conductive Al Layer

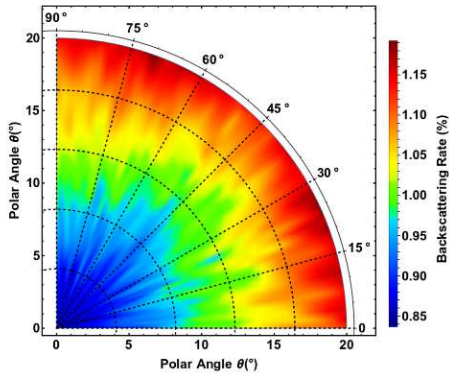

(b) 15 keV protons impinging on 30 nm conductive Al Layer

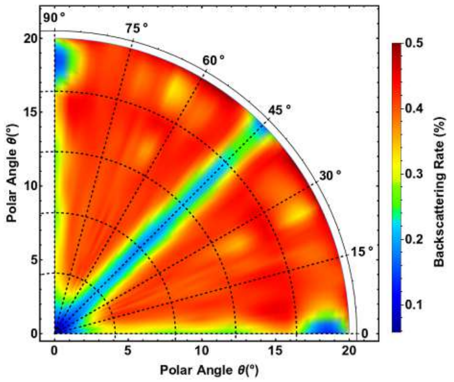

(c) 30 keV protons impinging on 3 nm passivation layer of SiO_2

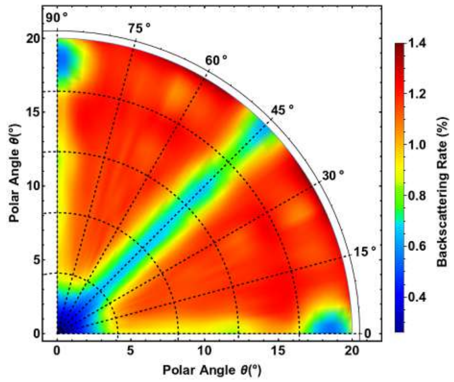

(d) 15 keV protons impinging on 3 nm passivation layer of SiO_2

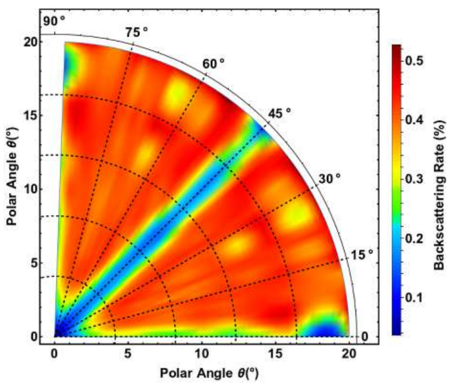

(e) 30 keV protons impinging on 1 nm passivation layer of Al_2O_3

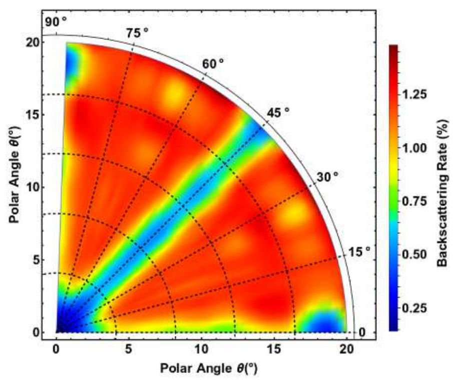

(f) 15 keV protons impinging on 1 nm passivation layer of Al_2O_3

Figure 5.10: Dependence of backscattering on the azimuthal angle $\phi\psi$for specific energies and sensor compositions. Note that each subfigure has its own colour scale so the angular dependence is easily visible.

Figure 5.10 shows the simulated IMSIL backscattering rates for the aforementioned combinations of polar and azimuthal angles for different sensor compositions with each figure having its own colour scale so the angular dependence is easily visible. As before, the thickness of the dead layer plays a key role in reducing the channeling effect and its impact on backscattering. When the thickness of the amorphous layer decreases or alternatively as the energy of impinging particles increases, a clearer change in the overall backscattering rate is observed for different impinging azimuthal and polar angles. However, for thicker layers, especially with lower proton energies, the backscattering rate more or less remains constant for different azimuthal angles, as seen in Fig. 5.10b. The backscattering rate changes minutely for different azimuthal angles, relative to the other compositions, and some semblance of a crystalline structure is seen for different azimuthal angles when the proton energy is increased as seen in Fig. 5.10a. For thinner passivation layers, such as those shown in Figs. 5.10c, 5.10d, 5.10e, and 5.10f, crystal channels as those shown in Fig. 5.2 are seen with smaller details being more visible for the latter case. However, as there is no major change of crystal axis due to the polar angle range being small, the absolute change in backscattering rates is not as huge as it would be if the polar angle would be extended up to 45° where impinging particles will see the {101} planar channels instead.

In many neutron beta decay experiments, the ϕ angle is isotropically distributed at the detector and therefore the assumption of averaging over it should be adequate. However, for experiments which have edge effects, e.g. due to shaping of the beam, the azimuthal angle distribution at the detector should be studied further. From the results of those investigations, if the uncertainty introduced by exclusion of the azimuthal angle dependence is large for a specific experiment, the effects should be incorporated appropriately within the data correction procedure (backscattering correction or calculation of detector efficiency). For NoMoS, this is further discussed in Sec. 5.2.

5.1.5 Importance of Channeling

Channeling effects are a cause of uncertainty and should be considered to apply corrections to the proton backscattering or detector efficiency. One of the standing puzzles in physics is the difference in the lifetime of free neutrons obtained from so-called bottle and beam experiments. The neutron lifetime values from beam experiments have a $\approx 4\sigma$ tension with those from bottle experiments, with the latter reporting a lower lifetime [41, 47]. While the bottle experiments go for counting of the neutrons left after a certain time period, the beam experiments on the other hand detect the decay products, namely post-accelerated protons, to derive the lifetime. For the latter purpose, the backscattering correction is of utmost importance for the beam experiments, which employ detectors with different thicknesses of Gold as a passivation layer in front of their silicon sensors [42] as well as "windowless" sensors, which are silicon sensors with a thin layer of SiO_2 in front. To account for backscattered protons i.e. those protons which leave a signal within the detector, those which are backscattered from the entrance window, and those which re-enter the detector after backscattering, a thorough Monte Carlo simulation study is carried out using SRIM. Consequently, the lifetime of the neutron is determined by fitting the linear functional dependence of the backscattering fraction obtained from SRIM, and the lifetime measurements conducted with different dead layered detectors at varying post-acceleration voltage and extrapolating the fit to the time value where backscattering fraction becomes 0 [42].

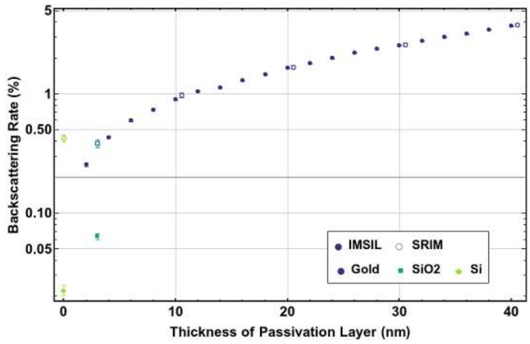

(a) 30 keV at 0°

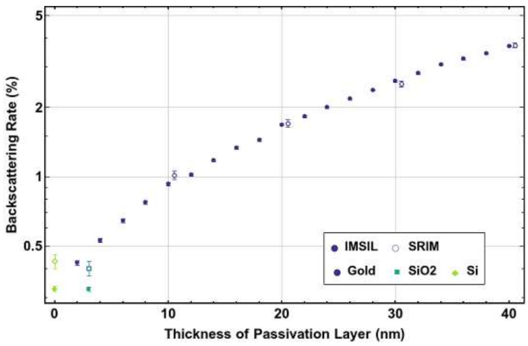

(b) 30 keV at 4°

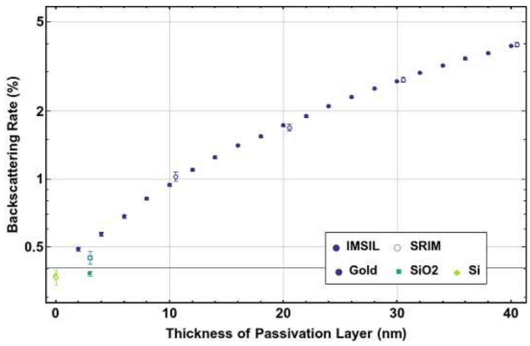

(c) 30 keV at 10°

Figure 5.11: Log Plots of the backscattering rate of 30 keV protons impinging upon detectors with different passivation layer thicknesses of gold, SiO_2 and pure silicon at different angles. The hollow points are the backscattering rates obtained from SRIM whereas the filled points represent those from IMSIL. Different colours represent the different materials of the passivation layer in front of the detector.

Figure 5.11 shows the backscattering rates obtained from both IMSIL and SRIM for different passivation layer thicknesses of Gold, SiO_2 and pure silicon at three different angles (0°, 4°, and 10°) for protons with a post-acceleration of 30 keV. A clear deviation between the backscattering rates is seen for lower angles for the detector without a passivation layer in front due to channeling effects. This difference is reduced but nonetheless still present for detectors with a thin passivation layer of 3 nm of SiO_2 even for angles of 10°. This is due to multiple scattering occurring within the dead layer that leads to the widening of the beam spread. It can also be seen in Fig. 5.11 that for even 10 nm layers of gold the channeling effects are smeared out. This is a consequence of multiple scattering widening the initial beam spread due to the high density of gold.

Another minor fact to consider is the determination of thickness of the passivation layer accurately. As already seen in Fig. 5.5c, for thinner dead layers the backscattering rate can vary slightly with the change of the layer thickness even by 2 nm. However, that correction is usually in the order of 0.02% and should be within the allowed systematic error budget.

It should be noted that the beam experiment utilizes three different post-acceleration voltages with an experiment specific distribution of the impinging polar angles, out of which 0° i.e. normal to the detector surface is most likely due to post-acceleration [117]. These experiments also employ a far more detailed study of the backscattered protons where backscattered protons which deposit a signal within the detector are treated differently than those which do not. If the untrue assumption for simplicity is made, that all backscattered protons are lost, than the deviation between the lifetimes will increase as the "windowless" detectors have the lowest backscattering rates at angles where channeling is the strongest for silicon sensors. However, another thing to note is how the electronic energy loss profile, and consequently the detector efficiency due to different penetration ranges of the protons, changes in silicon detectors when channeling is considered (see Figs. 5.6 and 5.9). Taking this into account may potentially help bridge the gap between the beam and bottle experiments but a detailed investigation of the incorporation of channeling in not only the backscattering but also the efficiency of the detector is required to make a solid statement as to in which direction will this shift the neutron lifetime or if it just increases the overall error bar on the current measurements.

5.2 Detection Efficiency of pLGAD Sensor

The detection efficiency of a pLGAD sensor in theory was calculated as explained before in Sec. 5.1.3, albeit with a passivation layer of Al_2O_3 of 1 nm thickness. The minimum detection threshold was set at 50 for the case of the superconducting NoMoS setup (see Sec. 4.4.2). However, as NoMoS is a precision experiment, additional investigations were performed as to how the detection efficiency of the sensor changes with varying angles, energies and uncertainties in the thickness of the passivation layer, which will be discussed further in this section.

5.2.1 Influence of Uncertainty in Passivation Layer Thickness

Even though Atomic Layer Deposition (ALD) is a well established technique with subnanometer precision in film thickness and composition [118], we will assume the worst case scenario where there may be an uncertainty introduced in the thickness of the passivation layer in front of the sensor. For this purpose, three different passivation layer thicknesses were investigated. These thicknesses included the intended 1 nm Al_2O_3, 2 nm Al_2O_3, and 3 nm Al_2O_3. Figure 5.12 shows the worst case scenario for change in detection efficiency due to uncertainty in the thickness of the passivation layer i.e. the lowest possible energy of the impinging protons in NoMoS at the highest impact angle (15 keV protons impinging the detector at 10°) for the three different dead layers. This is the worst case as the efficiency of any detector is the lowest at the minimum energy within the experiment, which is 15−15.8 keV in NoMoS. Furthermore, the higher the impinging polar angle of the protons, the more interactions it will have within the passivation layer leading to a drop in the overall detection efficiency.

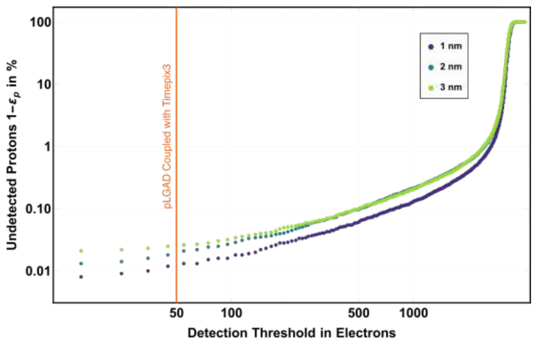

(a) Inverse of the efficiency of the 3 different simulated detector setups

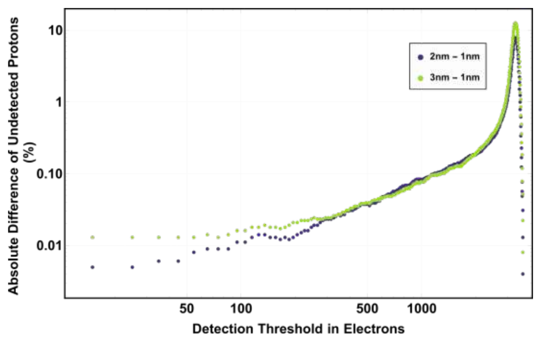

(b) Absolute difference of the signal lost due to uncertainty in passivation layer thickness

Figure 5.12: Log Log Plots of the proton detection efficiencies of three different simulated detector setups with 1 nm, 2 nm, and 3 nm thick passivation layer of Al_2O_3 in front of the silicon sensor with 15 keV energy impinging at 10°. The orange line represents the minimum number of e-h-pairs required by the pLGAD when coupled with a Timepix3 readout chip.

It can be seen in Fig. 5.12b that when the detection threshold of the minimum primary e-h-pairs required by the detector and DAQ increases, so does the difference introduced by the uncertainty in the thickness of the dead layer, reaching a peak at 10% before all signal is lost. However, due to the design of the pLGAD sensor, even in the case of having a dead layer with a thickness uncertainty of 2 nm, the absolute difference in the efficiency of the drift detector for NoMoS is ≈ 0.008%. This uncertainty can be further suppressed by measuring the thickness of the deposited passivation layer by the use of Tunneling Electron Microscopy (TEM) [119]. However, in the case a

TEM measurement is not possible, the thickness uncertainty is one of the sources of correction that will go into the calculation of the uncertainty of the overall detection efficiency of the drift detector of NoMoS.

5.2.2 Energy Dependence of Detector Efficiency in NoMoS

To study the energy dependence of the detector response, energies in the range of 15 − 15.8 keV in steps of 0.2 keV were simulated. Figure 5.13 shows the simulated signal lost at 0° as well as the absolute difference between the different energies when compared to the signal lost at 15 keV. Due to the low detection threshold of the pLGAD sensor, the difference is in the order of ≈ 0.005%. However, due to the low detection threshold of the pLGAD sensor and the overall small energy range of the protons, a functional dependence is hard to discern.

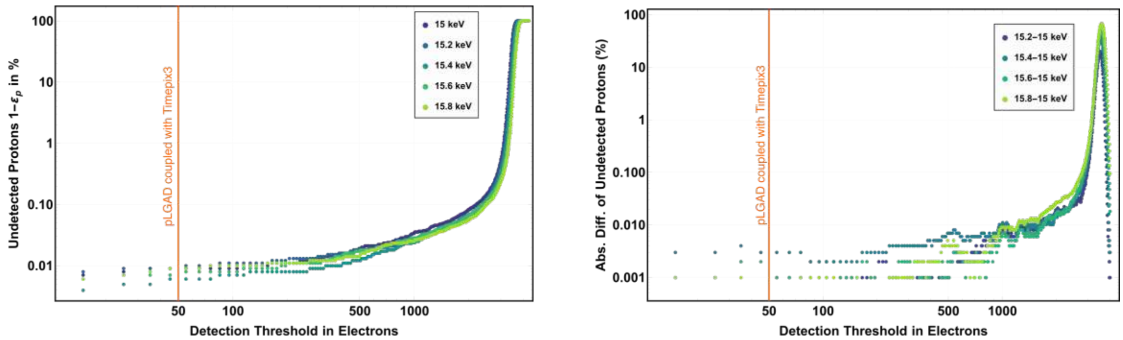

(a) Inverse of the efficiency of protons with different energies impinging on the detector at 0°

(b) Absolute difference of the signal lost when compared to that of 15 keV.

Figure 5.13: Log Log Plots of the protons detector efficiencies at different energies impinging at 0° on a detector with a 1 nm thick Al_2O_3 layer. The orange line represents the minimum number of e-h-pairs required by the pLGAD when coupled with a Timepix3 readout chip.

5.2.3 Polar Angular Dependence of Detector Efficiency in NoMoS

Due to post-acceleration, the polar angular distribution of protons is tilted forward and the maximum angle expected at the detector is ≈ 10°, as shown by Eq. (5.4). To study the effects of the angular dependence of detection efficiency, angles in the range of 0° – 10° in steps of 2° were simulated at various energies. Figure 5.14 shows the angular dependence of the efficiency due to change of the impinging polar angle of the protons at 15 keV, along with the absolute difference in efficiencies when compared to that of the protons at 0°. As expected protons impinging the detector below the critical angle ψ_c (≈ 4°) have a higher efficiency compared to angles greater than ψ_c due to their higher penetration depth. The highest absolute difference is in the order of ≈ 0.005%. Nonetheless, compared to the energy dependence a definite deviation in the absolute difference is seen between $\theta \leq \psi_c$ and $\theta > \psi_c$.

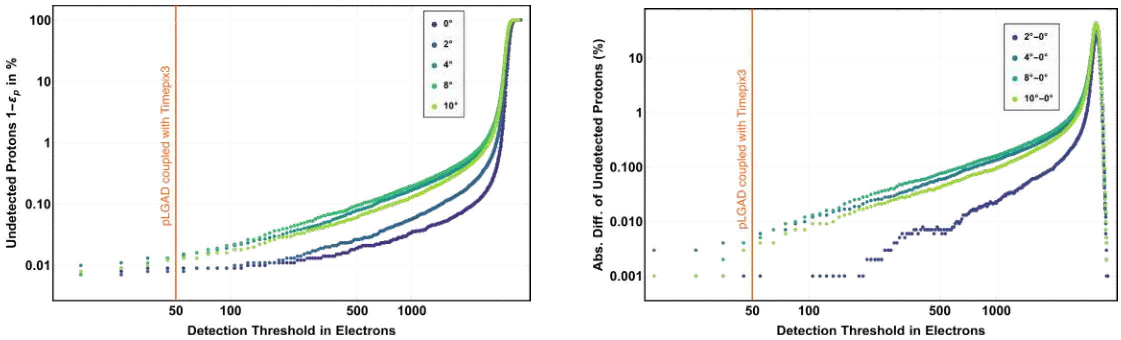

(a) Inverse of the efficiency of the protons impinging the detector at different angles

(b) Absolute difference of the signal lost when compared to that of 0°.

Figure 5.14: Log Log Plots of the undetected protons efficiencies at different angles impinging on a detector with a 1 nm thick Al_2O_3 layer at 15 keV. The orange line represents the minimum number of e-h-pairs required by the pLGAD when coupled with a Timepix3 readout chip.

5.2.4 Azimuthal Angular Dependence of Detector Efficiency in NoMoS

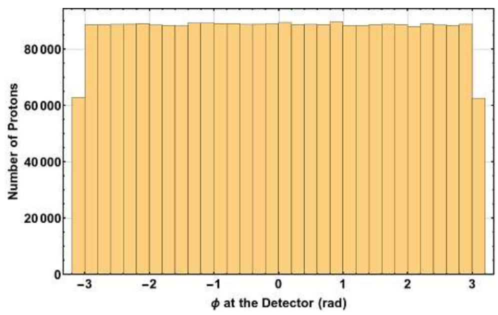

Figure 5.15: Azimuthal angle ϕ distribution of protons from neutron beta decay impinging on the main drift detector for the proposed superconducting setup of NoMoS [27] after passing through the aperture and the $\vec{R} \times \vec{B}$ region. Data obtained from Monte Carlo simulations with a total statistics of 3×10^6 protons on the detector

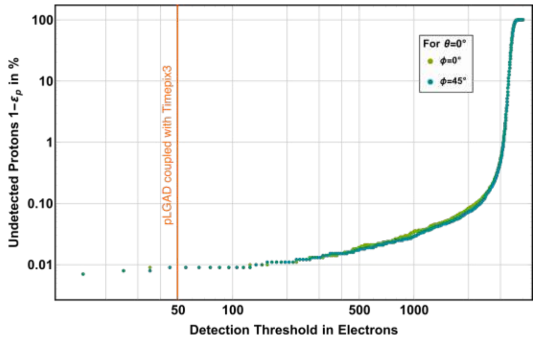

(a) Inverse of the detection efficiency of 15 keV protons impinging the detector with a polar angle of 0° and different azimuthal angles

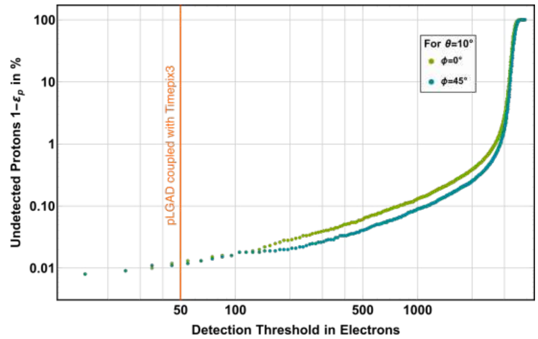

(b) Inverse of the detection efficiency of 15 keV protons impinging the detector with a polar angle of 10° and different azimuthal angles

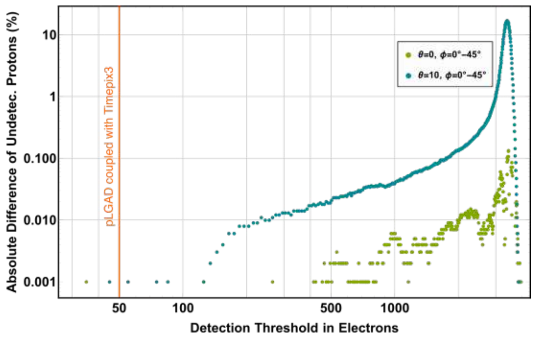

(c) Absolute difference of the signal lost when compared to that of ϕ =0°.

Figure 5.16: Log Log Plots of the protons' detection efficiencies at different angles impinging at 15 keV on a detector with a 1 nm thick Al_2O_3 layer. The orange line represents the minimum number of e-h-pairs required by the pLGAD when coupled with a Timepix3 readout chip.

Considering the additional dependence of backscattering on ϕ, any experiment which has edge effects should consider the effect of the azimuthal angle dependence of channeling at the detector. Usually, a uniform distribution of ϕ is expected at the detector, however an additional dependence may be introduced due to edge effects stemming from different parts of the experiment e.g. from shaping the beam at the aperture in NoMoS. Therefore, Monte Carlo simulations of NoMoS were performed for the proposed superconducting setup for protons. The results of which are shown in Fig. 5.15, where the ϕ angle of the protons hitting the detector after passing through the $\vec{R} \times \vec{B}$ are shown. As already covered in the thesis of [27], a uniform distribution is seen for the case of protons. Therefore the assumption of averaging over the azimuthal angle, at least for the case of NoMoS, remains valid.

However, as already shown in Fig. 5.10f, there are certain angles within the chosen detector configuration of NoMoS where some azimuthal angles introduce a different crystalline plane for the protons to channel into e.g. at $\phi = 45°$. Therefore, for an advanced investigation of the detector efficiency, at least two cases were studied for two different polar angles $\theta = 0°$ and $\theta = 10°$ for fixed azimuthal angles of $\phi = 0°$ and $\phi = 45°$. The choice of these angles was influenced from Fig. 5.10f, where $\phi = 45°$ offers a lower backscattering rate due to the proton impinging upon a different crystalline axes.

Figure 5.16 shows the Log-Log plots of the signal lost for the aforementioned cases, as well as the absolute difference between the two different ϕ angles for their respective θ. As expected, the variable of ϕ barely makes a difference in the efficiency for the case of $\theta = 0°$. However for the case of $\theta = 10°$, a bigger deviation compared to all other sources of uncertainties that have been considered until now is observed, especially for a detection threshold $p_{\mathrm{min}} > 200$ electrons. Due to the internal gain and low noise requirements of the pLGAD, this is a smaller correction than that of the polar angle and energy for NoMoS due to the uniformity of the ϕ angle of the impinging particles, but if a different silicon detector technology is utilized then the ϕ angle dependence of the impinging protons, which already defines some edge effects at the aperture and the detector, should be considered for the case of the detection efficiency as well, therefore increasing the integration dimensions of the transport function (see Chapter 6) of NoMoS.

5.2.5 Total Detection Efficiency of the pLGAD in NoMoS

When all the aforementioned sources of uncertainty in the loss of signal of the pLGAD are taken into account, it can be seen that the sensor can nonetheless achieve a detection efficiency of $99.99\% \pm 0.02\%$, where the error bars are statistical, for the chosen post-acceleration voltage and passivation layer in front of the detector. The effect of the uncertainty in the energy, and angular dependence of the total detection efficiency on the parameter a will be studied further in the next chapter. However, it should be noted that the total detection efficiency may need to be revisited if due to surface defects in the final production wafer of the pLGAD, the CCE is worse than that used for the sake of these studies.

Chapter 6

Investigation of Systematic Effects in NoMoS

The investigation of systematic effects and the associated uncertainties allow for the calculation of an total systematic error budget for an experiment. For the case of NoMoS, these studies could be performed with the help of an analytical description of the experiment along with its systematic effects called the transfer function.

Using the Transfer function, different systematic effects for the superconducting setup of the NoMoS apparatus were investigated to suggest corrections for the determination of the desired correlation coefficients and study the magnitude of uncertainties so that the experiment could meet its final precision goal. During the course of these investigations, it came to attention that the superconducting setup of the NoMoS apparatus needed further optimization. As the optimization of the magnetic field setup of the experiment were out of scope of this thesis, a compromise with a semi-optimized setup was found. Furthermore, the need of smaller aperture dimensions for the super conducing variant of the experiment were also highlighted during the course of my investigations.

Additionally, the investigation of detection-related systematic effects such as detector misalignment, efficiency, and the spatial resolution required, with their corresponding uncertainties was performed. Furthermore, the use of an additional fit parameter in the Transfer function was also studied. It was found that this can improve the uncertainty introduced by certain systematic effects by a factor of at least 10.

6.1 The Transfer Function of NoMoS

An alternative to the popularly utilized Monte Carlo simulations for the investigation of systematic effects is the use of an analytical description of the experiment instead. The transfer function allows for the analytic reconstruction of the observable spectrum by the use of numerical integrations. While the full description of the Transfer function for the case of electrons can be read in Chapters 4 and 5 of [27], for the purpose of this work, the function for protons was developed instead by me and is given by:

$$\begin{aligned} G(j, s_i) = \iint_{\mathcal{T}} & w_p(p_p, a) \sin\theta_0 T_x(\ldots, s_i) T_y(\ldots, s_i) \\ & \mathrm{Apert}(x_{\mathrm{A}} y_{\mathrm{A}}, s_i) \varepsilon(\ldots, s_i) BS_{\mathrm{corr}}(\ldots, s_i) n(\ldots, s_i) W_F(\ldots, s_i), \end{aligned} \tag{6.1}$$

with the nine-dimensional domain $\mathcal{T}$

$$\mathcal{T} = dy_{\mathrm{DV}}\, dx_{\mathrm{DV}}\, dy\phi_{\mathrm{A}}\, dp_{\mathrm{p}}\, d\phi_{\mathrm{DV}}\, d\phi_{\mathrm{D}}\, d\theta_0\, dx_{\mathrm{Dj}}\, dy_{\mathrm{Dj}}, \tag{6.2}$$

where dx_{Dj} and dy_{Dj} represent the detector bin differentials for the bin j, for a proton momentum decay spectrum within the neutron beta decay given by w_p for a value of p_p of momentum and an electron-antineutrino correlation value a produced at an angle of θ_0. The singular functions within the integral along with their arguments are as follows:

Delta Function T_x: This is the delta function in the drift direction of the experiment and incorporates the proton's transfer from the Decay Volume (DV) with a magnetic field B_{DV} through the Aperture (A) into the $R \times B$ region where it experiences the $R \times B$ drift $D_{R\times B}$ and finally its arrival at the Detector (D). Mathematically it has the following arguments:

$$\begin{aligned} T_x = & T_x(x_{\mathrm{DV}}, p_p, \phi_{\mathrm{DV}}, \phi_{\mathrm{D}}, \theta_0, x_{\mathrm{Dj}}; \\ & B_{R\times B}, r_{R\times B}, y_{R\times B,GC}(\ldots, y_{\mathrm{DV}}, y_{R\times B,\mathrm{Shift}}), G_1, G_2, r_{\mathrm{D}}, x_{\mathrm{D,Shift}}). \end{aligned} \tag{6.3}$$

The Delta function T_x as a consequence of its construction, apart from depending upon the systematic parameters also has a dependency on the $y_{R\times B,\mathrm{GC}}$, which is the second detector dimension. x_{DV} is the position of the proton at the Decay volume and is given by:

$$\begin{aligned} x_{\mathrm{DV}} = & [(x_{\mathrm{D}} - r_{\mathrm{D,G}} \cos\phi_{\mathrm{D}} - x_{\mathrm{D,Shift}}) \sqrt{\frac{r_{\mathrm{D}}}{r_{R\times B}}} - D_{R\times B}(y_{R\times B,\mathrm{GC}})] \\ & \times \sqrt{r_{R\times B}} + r_{\mathrm{DV,G}} \cos\phi_{\mathrm{DV}}, \end{aligned} \tag{6.4}$$

where $r_{\mathrm{D,G}}$ and $r_{\mathrm{DV,G}}$ represent the gyration radii at the detector and decay volume respectively, $x_{\mathrm{D,Shift}}$ is the shift of the central magnetic field line at the detector compared to the geometric centre of the experiment in the drift axis, $y_{R\times B,\mathrm{GC}}$ is the gyration centre of the protons within the $R \times B$ region and $\sqrt{r_{\mathrm{D}}}$ and $\sqrt{r_{R\times B}}$ represent the magnetic field ratios of the detector and the $R \times B$ region respectively compared to the magnetic field at the decay volume.

It should be noted that the $R \times B$ drift function depends on the $y_{R\times B,\mathrm{GC}}$, which is the second detector dimension that in turn depends on the y position of the proton in the decay volume y_{DV}. This dependence mainly stems from the magnetic field gradient in the radial coordinate axis of the $R \times B$ region's toroid, referred to as the non-drift axis. Mathematically it is given by:

$$y_{\mathrm{DV}} = (y_{\mathrm{D}} - r_{\mathrm{D,G}} \sin \phi_{\mathrm{D}} - y_{\mathrm{D,Shift}})\sqrt{r_{\mathrm{D}}} + r_{\mathrm{DV,G}} \sin \phi_{\mathrm{DV}}. \tag{6.5}$$

Delta Function T_y: T_y is the delta function in the non drift direction, and it depends on:

$$T_y = T_y(y_{\mathrm{DV}}, p_{\mathrm{p}}, \phi_{\mathrm{DV}}, \phi_{\mathrm{D}}, \theta_0, y_{\mathrm{Dj}}, B_{R\times B}, r_{\mathrm{D}}, y_{\mathrm{D,Shift}}), \tag{6.6}$$

where y_{DV} is given by Eq. 6.5, $B_{R\times B}$ is the absolute magnetic field of the $R \times B$ region, and $y_{\mathrm{D,Shift}}$ is the shift of the central magnetic field line compared to the geometric centre of the experiment in the detector region in the non-drift axis.

Aperture Function Apert: This is the Aperture function that introduces cuts at the aperture of the experiment to cut the decay products beam and will be discussed in a bit more detail during the investigation of the aperture size as a systematic in NoMoS. Mathematically it is dependent on:

$$\mathrm{Apert} = \mathrm{Apert}(x_{\mathrm{DV}}, y_{\mathrm{DV}}, p_{\mathrm{p}}, \theta_0, \phi_{\mathrm{DV}}, \phi_{\mathrm{A}}, B_{R\times B}, r_{\mathrm{A}}, x_{\mathrm{A,Shift}}, y_{\mathrm{A,Shift}}), \tag{6.7}$$

where $x_{\mathrm{A,Shift}}$ and $y_{\mathrm{A,Shift}}$ are the deviation of the central magnetic field line at the aperture from the geometric centre of the experiment at the aperture region.

Efficiency Function ε: For the case of protons, the efficiency function basically defines the detector efficiency of the pLGAD for the impinging post-accelerated protons. It will be further discussed in the efficiency systematic investigation. It is dependent on:

$$\varepsilon = \varepsilon(p_p, \theta_0, r_{\mathrm{D}}, U_{\text{post-Acc.}}, c_i), \tag{6.8}$$

where $U_{\text{post-Acc.}}$ is the post-acceleration voltage, and c_i are the fit coefficients obtained by fitting over the simulated efficiencies for a specific detection threshold at different energies and angles.

Backscattering Correction $\mathbf{BS_{corr}}$: The backscattering correction function corrects the spectrum for the backscattered protons or electrons. For the case of electrons, the function is aided additionally by the active aperture which can provide some information about veto signals. For the case of protons, this function provides correction of the spectrum for double hits as backscattered protons will have a chance of depositing enough signal within the detector, backscatter and then re-enter the detector due to the presence of a post-acceleration electrode. The function is dependent on:

$$\mathrm{BS_{corr}} = \mathrm{BS_{corr}}(p_p, \theta_0, r_{\mathrm{D}}, U_{\text{post-Acc.}}, c_n), \tag{6.9}$$

where c_n represent the fit coefficients. For the case of electrons, as there is no post-acceleration there is no additional dependency on r_{D}.

Neutron Beam Profile n: The neutron beam profile function is an estimated neutron beam profile at the decay volume of the experiment. During the course of this work, this was set as infinitely wide i.e. having no falling edges within the decay volume, to decouple edge effects introduced from the aperture in an attempt to check the optimization of the superconducting setup of the experiment. It is dependent on:

$$n = n(x_{\mathrm{DV}}, y_{\mathrm{DV}}, w_x, w_y, p_x, p_y, k_{1,x}, k_{2,x}, k_{1,y}, k_{2,y}), \tag{6.10}$$

where w_n gives the length of the beam's boundaries, p_n gives the length of the trapezoidal plateau, and $k_{i,n}$ give the slopes in different dimensions.

Work function Differences Function W_F : Lastly, the work function differences function gives the change of the kinetic energy of the protons caused by the work function of different materials used in the construction of the $R \times B$ region of the experiment. It depends on:

$$W_F = W_F(p_p, \Phi_{\mathrm{mat}}), \tag{6.11}$$

where Φ_{mat} is the material work function of the different material. It should be remembered that these differences can be reduced by conducting measurements of the material work functions of the different materials within the vacuum tube, having the welding seams be performed in the y-axis of the experiment, as far away from the drift direction of the protons as possible.

6.2 Methodology of Investigation

The methodology employed to investigate the systematic effects was to use the Transfer Function of NoMoS to study the effects of the inaccuracies of the relevant systematic parameters on the fitted observables and provide correction values for the observables as well as to study the effects of the uncertainties of the systematic parameters.

To perform the aforementioned task, a slight deviation was introduced on a systematic parameter within the Transfer function. A minimized squared sum difference analysis was then conducted by comparing the modified spectrum with a reference spectrum. The modified spectrum was obtained by varying solely the value of the "fitted" correlation coefficient parameter i.e. electron-antineutrino angular correlation coefficient parameter a or the Fierz Interference term b. For example, for the uncertainty introduced in the efficiency of the detector for the case of protons is shown in Fig. 6.1. Fig. 6.1a shows the absolute difference between a reference spectrum without a correction for detection efficiency and the drift spectra with the incorporated detector efficiency correction for different a values. This correction in the detection efficiency of protons is further dependent on the impinging angle and energies of the protons (see section 6.5), and as a consequence ranges from unity between $0.01\% - 0.03\%$. Figure 6.1b on the other hand shows the manual parabolic fit of the least square minimization, or what is referred to as the χ^2 distribution within the course of this work, for this example.

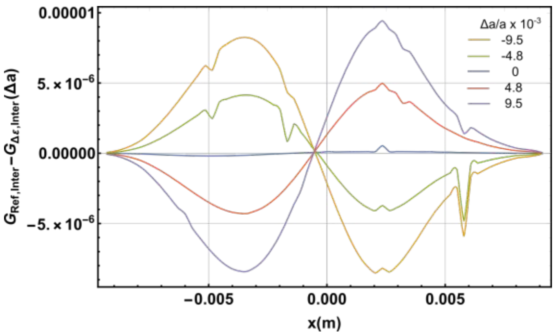

(a) Difference of the interpolated reference transport spectrum with modified one for different a values. Please note that certain peak behaviours are due to the limits of the set numerical precision of the integral and vanish if it is increased

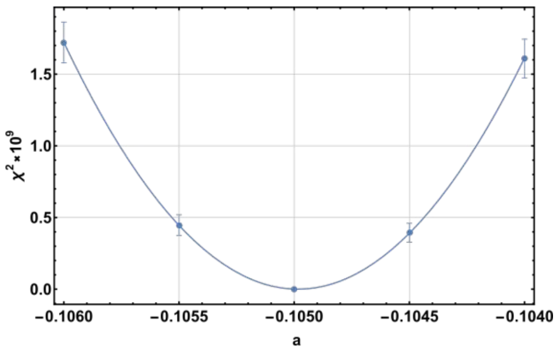

(b) Parabolic fit over the χ^2 distribution (see Eq. (6.12)) obtained by the least squared method. The values of the fit are: $a = -0.104984$, scale $= 0.0017$, and offset $= 4.8 \times 10^{-13}$. The error bars are conservative estimates of the error introduced by the set limit on the precision of the numerical integration

Figure 6.1: An exemplary plot of the uncertainty introduced when the correction for detector efficiency is not taken into account. The corresponding efficiency of the detector has an additional dependence on p_p and θ_0 and consequently varies in the range of $0.01\% - 0.03\%$ compared to the reference spectrum which has a detector with unity efficiency for all energies and angles i.e. without the correction. This gives a relative deviation $\Delta a/a = 1.6 \times 10^{-4}$

The χ^2 is determined by:

$$\chi^2(\Delta a)_{p_1=\varepsilon} = \sum_{\text{bin}=1}^{N} \Big([G_{\text{Ref}}(\text{bin}, a = -0.105, p_1, p_2, \ldots, p_n) \\ - G_{\text{fit}}(\text{bin}, \Delta a, p_1 + \Delta p_1, p_2, \ldots, p_n)]^2, \qquad (6.12)$$

where p_i are the systematic parameters, ε is the detector efficiency, G_{Ref} is the reference spectrum and G_{fit} is the spectrum where the value of a is varied to find the least square for the uncertainty introduced on a systematic parameter. As there are no statistical uncertainties assumed in this case, the values of these χ^2 reductions will always be far from 1.

To obtain the value of the minimum from the χ^2 reduction, a manual parabolic fit is used due to the computational intensity of the Transfer function, which would require more than a week to converge to a fit value otherwise. The equation used for the parabolic fit is:

$$\chi^2_{\text{fit}} = \text{scale}(\Delta a - a)^2 + \text{offset} \tag{6.13}$$

Where scale and offset are variables which are fitted over to obtain the deviation caused in a by the uncertainty of a specific systematic parameter.

6.2.1 Scaling Factors

By introducing an uncertainty in a systematic parameter, the deviation caused in the observable can be scaled linearly as long as the introduced uncertainty Δp was small enough. Using this assumption, so called scaling factors can be calculated for systematic parameters to not only give the deviation caused on the observable for a certain uncertainty of a specific systematic parameter but also as a tool to gauge how well an uncertainty should be known for the experiment to reach its ultimate precision goal. Mathematically, we can calculate this scaling factor k by using:

$$\frac{\Delta a_{\text{min}}}{a} = k \frac{\Delta p}{p} \rightarrow k = \frac{\Delta a}{a} \frac{p}{\Delta p} \tag{6.14}$$

6.3 Update of the Proposed Superconducting Setup for NoMoS

As NoMoS is a position sensitive experiment, systematic effects which can cause additional uncertainty in the final position of the impinging particles have to be studied in detail to ensure the experiment can meet its ultimate precision goal. As one of these effects stems from the post-acceleration of protons in the presence of a magnetic field before detection, efforts have to be made to ensure that the additional $\vec{E} \times \vec{B}$ drifts experienced by the protons are suppressed and understood. The preliminary studies of the electrode design suggested that for suppression of additional $\vec{E} \times \vec{B}$ effects, a setup with a magnetic flux density of at least 800 mT needs to be considered [58]. Therefore, this work focuses primarily on the proposed superconducting setup for NoMoS in Ref. [27]. Furthermore, the superconducting setup in principle should also provide a lower overall systematic error budget as the increase in the flux density of the magnetic field suppresses some other systematic effects [27]. A brief summary of the magnetic field parameters based on design studies of the magnetic field coils for the superconducting setup can be seen in Table 6.1 as suggested in Ref. [27].

Investigation of the Magnetic Field Ratio at the Aperture

Even though this work deals mainly with the study of the uncertainties introduced by the detection system within NoMoS, some additional parameters that are closely related to the detection side of the experiment were also studied. The purpose of these studies was to check if NoMoS could indeed reach the desired final precision for the case of protons, as those values had not been investigated before.

One parameter chosen for this purpose was the investigation of the aperture size as well as the magnetic field ratio at the aperture r_{A}, as the aperture within the experiment is supposed to be active for the veto of backscattered electrons. r_{A} was also selected as it had a higher scaling factor compared to the one from the uncertainty in the magnetic field ratio at the detector r_{D} for the case of electrons in the normal conducting setup. However during the course of investigations, it was discovered that the systematic uncertainty introduced by an uncertainty on r_{A} for the proposed superconducting setup was far higher than expected. The investigation gave a relative uncertainty of 1.5% on a, compared to a relative uncertainty of 0.1% on a for the normal conducting setup. This meant that for the experiment to achieve its ultimate precision of 0.3% or even closer, r_{A} should be known to a relative uncertainty of 1×10^{-5} level. This warranted further investigations as one possibility for such a high value of systematic uncertainty was the non perfect optimization of the magnetic field ratios between the different regions of the experiment and the decay volume.

The first attempt to investigate where the uncertainty came from was by eliminating unnecessary sources of edge effects within the experiment. For this purpose, the neutron beam profile was set to be infinitely wide within the decay volume. However it made little to no effect on the error caused by the systematic uncertainty. Nonetheless, in all subsequent investigations the neutron beam profile was left infinitely wide as in principle the uncertainty caused by the neutron beam profile was small enough to be ignored and it sped up the numerical integrations as there was one less integral to evaluate.

Systematic Effect	**Parameter**	**Value**	**Uncertainty** (10^{-3})
Magnetic Field			
Filter Magnetic Field Ratio	r_{F}	2.036	0.1568
Aperture Magnetic Field Ratio	r_{A}	0.937	0.1057
$R \times B$ Magnetic Field Ratio	$r_{R\times B}$	0.902	0.150
Magnetic Field in $R \times B$ Region	$B_{R\times B}$	0.976 T	0.150
Radial Gradient Coefficients	G_1	1.290	2.000
	G_2	1.792	2.000
Curvature Angle		180.030°	0.100
Detector Magnetic Field Ratio	r_{D}	0.880	0.0466
Central Field Line Displacement	$x_{\mathrm{A,Shift}}$	0.000 mm	0.100 mm*
	$y_{\mathrm{A,Shift}}$	2.873 mm	0.100 mm*
	$y_{R\times B,\mathrm{Shift}}$	1.518 mm	0.100 mm*
	$x_{\mathrm{D,Shift}}$	0 mm	0.100 mm*
	$y_{\mathrm{D,Shift}}$	6.234 mm	0.100 mm*
Other			
Aperture Dimensions	x_{AA}	10.000 mm	0.200 mm*
	y_{AA}	35.000 mm	0.200 mm*
	$x_{\mathrm{AA,Offset}}$	30.000 mm	0.200 mm*
	$y_{\mathrm{AA,Offset}}$	0.000 mm	0.200 mm*
Neutron Beam	$w_{n,x}, w_{n,y}$	10,6 cm	0.750
	$p_{n,x}, p_{n,y}$	9,5 cm	2.600
	$k_{x,1}, k_{y,1}$	0.9	6.000
	$k_{x,2}, k_{y,2}$	0	1.000*
	$k_{x,3}, k_{y,3}$	-0.9	1.000

Table 6.1: The values for the superconducting NoMoS setup, as estimated in Ref. [27]. All uncertainties except those marked with * are relative. Those marked with * are absolute.

Further attempts to minimize the error caused by the uncertainty included shifting the position of the centre of the aperture from the proposed 30 mm to −9 mm in the drift direction so that centre of the detector coincided with the maximum of the measurement spectrum. Furthermore, all magnetic field ratios were also set to 1, with the exception of the filter magnetic field ratio r_{F} as it defines the maximum angle allowed to pass through the filter region within the experiment. An exemplary figure of how the drift distance spectrum in such a case looks like is shown in Fig. 6.2. This caused the relative uncertainty introduced by r_{A} to shrink down to 0.32% meaning that r_{A} has to be known to a relative uncertainty of 10^{-4} or 9×10^{-5} level to be able to achieve the ultimate precision within the experiment.

For the case of electrons, the same exercise of having to move the aperture, albeit in the other direction, as well as reducing the magnetic field ratios apart from the one at filter to 1 yielded numbers close to the ones provided by D. Moser in his thesis for the normal conducting case. Thus further cementing the conclusion that the magnetic field ratios within the superconducting setup had to be further optimized in order to achieve better results. However, as the optimization of the magnetic field is outside the scope of this work, for further investigations, all magnetic field ratios apart from r_{F} were set to 1 for the sake of introducing a slight simplicity in a complex system. Furthermore, this also means that all uncertainties within the course of this work are not set in stone and can be made better by further optimizing the superconducting setup of NoMoS.

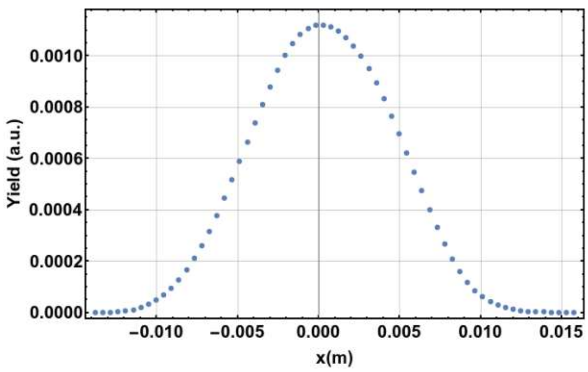

Figure 6.2: The proton drift distance spectrum in the drift dimension with 64 detector bins. Here the other dimension is integrated over and the spectrum was obtained from using the Transfer function that has the magnetic field ratios, apart from r_{F}, set to 1, and the aperture moved so that the spectrum is more centric on the detector.

6.3.1 Aperture Dimensions

The aperture of the experiment not only helps define the final beam at the detector but in essence it is also a part of the detection system. Therefore, its dimensions were investigated in detail during the course of this work. However, as the aperture will be 3 dimensional, for these studies it was assumed to have negligible thickness in the axis of beam propagation. For this purpose, the study of the same systematic uncertainty introduced on r_{A} as in the previous section was repeated. The choice of investigating the systematic uncertainty on r_{A} was made so that a reference spectrum could be obtained for a specific aperture width and height. Having a reference spectrum dependent on r_{A} meant that it was independent of how the change of aperture dimensions influenced the observables in the experiment but instead provided information on how well the aperture height and width should be known to achieve the desired precision.

Aperture Width

The aperture's width is one of the key parameters in defining how the beam looks like on the detector as it is in the drift direction of the particles. Therefore, it was the first parameter to be investigated by keeping the aperture height constant at the proposed 35 mm. Figure 6.3 shows the scaling factors obtained for a relative uncertainty of 10^{-4} on r_{A} for different aperture widths. A lower scaling factor corresponds to a lower relative uncertainty on the observable as explained in Section 6.2.1. A "W" like structure for the aperture widths with two minima was observed as a result of this investigation, see Figure 6.3. While one minimum was at the originally proposed width of 10 mm, the other was at 2.5 mm, after which the edge effects started to dominate. This in essence meant that usage of either the proposed aperture width of 10 mm or the smaller aperture width of 2.5 mm could be used within the superconducting setup of NoMoS.

In order to arrive at a proposed value of the aperture, the final uncertainty on the observable was also considered by taking the fit uncertainty of different aperture widths into account. Figure 6.4 shows the uncertainty on the fitted observable a of the fits applied for the evaluation of Fig. 6.3. As the uncertainties scale by a factor of $1/\sqrt{N}$, to achieve the same statistical sensitivity on a, longer measuring times are required for 10 mm compared to 2.5 mm, even though the smaller aperture allows for fewer particles to pass through. This is due to the smearing out of the measured spectrum as particles with bigger gyration radii are able to pass through the 10 mm wide aperture. This leads to a loss of sensitivity on the measured observable, a in this case. Therefore, for the course of this work, the aperture width of 2.5 mm for the superconducting case is used as it allows achieving a better statistical uncertainty on the final observable a collecting of fewer protons. Nonetheless, the possibility of a 10 mm aperture can also be used as a smaller aperture is more susceptible to manufacturing tolerances

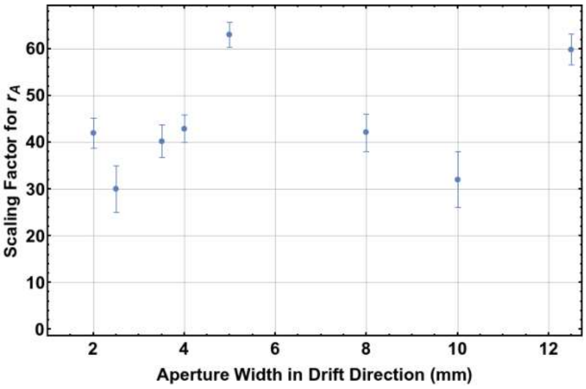

Figure 6.3: The scaling factors obtained for r_A for different aperture widths in the drift direction. A lower scaling factor corresponds to a lower relative uncertainty on the observable a, as the same relative uncertainty of 10^{-4} was introduced on r_A for all cases. The error bars are the result of the propagation of errors from the parabolic fit as well as the constraints on the numerical precision of the integration when Δa is determined.

compared to a bigger one. Consequently, the aperture width of 2.5 mm is only a recommendation, and if a smaller aperture with small manufacturing tolerances is not possible, it is recommended to revert back to the originally proposed aperture width of 10 mm instead.

A similar study for the case of b for electrons was also conducted, however it was reduced to comparing only the 2.5 mm aperture width with 10 mm with all magnetic field ratios apart from the one at filter set to 1. The results of the study yielded an absolute uncertainty on b of 0.0011 for a relative uncertainty of 10^{-4} introduced on r_A for the 10 mm aperture and an absolute uncertainty of 0.0007 for the case of the 2.5 mm aperture, thereby supporting the decision to study further systematics with the reduced aperture size.

Aperture Height

The height of the aperture does not have as big an influence on the observable as the width because at the end the non-drift direction at the detector is integrated over to allow for more bins in the drift direction of the detector. Nonetheless, the influence of different heights of the aperture were also studied by introducing a relative uncertainty of 10^{-4} on r_A for three different aperture heights.

Figure 6.5 shows the scaling factors for 4 different aperture heights. It can be seen that the aperture height as opposed to the aperture width does not change the scaling factors for r_A as dramatically, even when a step size of 5 mm is used. However at 20 mm height the scaling factor explodes with a huge error bar, which is a consequence of the

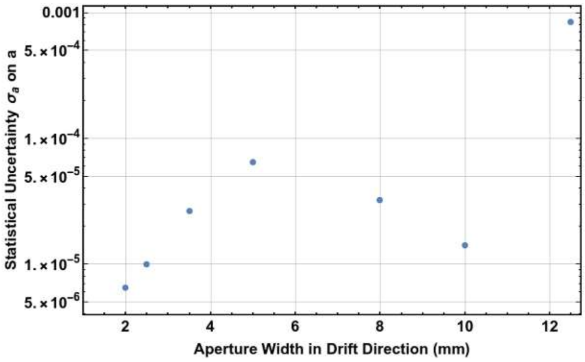

Figure 6.4: The uncertainty on the fitted observable a, in log scale, for varying aperture widths for 10^{-4} relative uncertainty introduced on r_{A}. It should be remembered that the uncertainties scale by a factor of $1/\sqrt{N}$.

domination of edge effects as this height combined with the aperture width of 2.5 mm starts to cut harshly into the decay products beam. Consequently, the aperture height was left unchanged and the proposed value from the normal conducting setup of 35 mm was used for the rest of the investigations.

6.3.2 Aperture Offset

Even though the magnetic field ratios for the superconducting setup need to be optimized, nonetheless studying the existing magnetic coil setup could provide an avenue for making educated guesses for the determination of different parameters of the experiment. For investigation of the aperture offset in the y dimension, the magnetic field generated by the proposed setup was studied using Radia [120], initially as a check of the previous investigations.

Figure 6.6 shows the contour plots of the magnetic field at the aperture in the originally proposed superconducting NoMoS setup with a small aperture of 2.5 mm × 35 mm and $2r_{\mathrm{G,max}}$ on all sides to show the region from which protons could enter the $R\!\!\!/\times B\!\!\!/$ region of the experiment. It is observed that introducing a small offset in the y position from 0 mm to −8.5 mm reduces the homogeneity of the magnetic field experienced by the charged decay particles entering the $R\!\!\!/\times B\!\!\!/$ region from 4×10^{-4} to 3×10^{-4}. It should be noted that even though changing $x_{\mathrm{AA,offset}}$ can also further reduce this number, it is not recommended in order to ensure that the particles at the detector see a more homogenous field.

To investigate if this also held true for the simplified NoMoS setup where all magnetic field ratios apart from the one at the filter were set to 1, a $y_{\mathrm{AA,offset}} = -8.5$ mm was introduced in the Transfer Function. In the most simplistic case, where the drift does not take the magnetic field gradient in the non drift direction into account, this

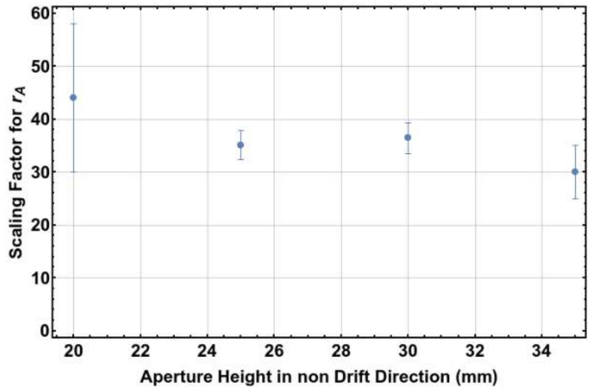

Figure 6.5: The scaling factors obtained for r_{A} for different aperture heights in the non drift direction. A lower scaling factor corresponds to a lower relative uncertainty on the observable a, as the same relative uncertainty of 10^{-4} was introduced on r_{A} for all cases. The error bars are the result of the propagation of errors from the parabolic fit as well as the constraints on the numerical precision of the integration when $\Delta a/$ is determined.

should have had no effect. However, as the Transfer function used is in a more finalized state, introducing this offset saw the scaling factor of the uncertainty investigated, r_{A}, reduce slightly from an absolute uncertainty on $b/$ of 7.8×10^{-4} to 6.8×10^{-4} whereas for the case of $a/$ the relative uncertainty remained within error bars of the fit.

Even though this investigation did not lead to further reduction of the uncertainty on the fitted observables, it however did strengthen the ansatz that further optimization of the superconducting setup was required as well as the fact that some of these numbers would need to be revisited after the optimization and design of a new magnetic coil setup.

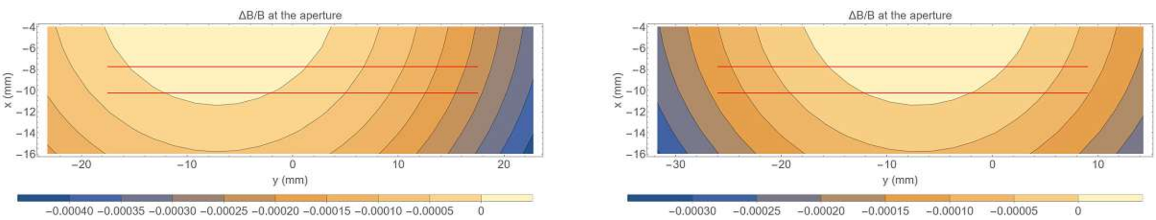

(a) Aperture position is offset in the drift direction $x_{\mathrm{AA,offset}}$ to make the spectrum centred at the detector and $y_{\mathrm{AA,offset}} = 0$

(b) Aperture position is offset in the drift direction $x_{\mathrm{AA,offset}}$ to make the spectrum centred at the detector and $y_{\mathrm{AA,offset}} = -8.5\,\mathrm{mm}$

Figure 6.6: Contour plots of the relative change of the magnetic field at the aperture for the proposed superconducting setup of NoMoS with the reduced aperture size of $2.5\,\mathrm{mm}$ plus $2r_{\mathrm{G,max}}$ on all sides. The red lines mark the actual aperture position.

6.3.3 Summary of Proposed Changes

For further investigations within this thesis, the following changes are made to the proposed original superconducting setup:

- $r_{\mathrm{A}} = r_{R\times B} = r_{\mathrm{D}} = 1$
- $x_{\mathrm{AA,offset}} = -9\,\mathrm{mm}$ for protons and $6.5\,\mathrm{mm}$ for electrons for the superconducting case
- Neutron beam profile set to be infinitely wide and uniform at the decay volume
- Summation of the bins in the non-drift direction so all investigations are performed on a 1D spectrum, see Sec. 6.4.1.
- Reduced the aperture width to $2.5\,\mathrm{mm}$
- Centering the observable spectrum at the detector by moving the aperture so that the maximum of the spectrum in the drift direction falls on the centre of the detector

The rest of the values are the kept the same as in Table 6.1. Whereas in general the following recommendations are made before the superconducting setup of the experiment is realized:

- Further Optimization of the magnetic field ratios of the superconducting setup
- Revisiting aperture offsets after the re-optimization process of the magnetic field ratios
- Re-enabling the neutron beam profile with a proper description

6.4 Detector Related Systematics

Due to the low energy of protons from free neutron beta decay, their detection is quite a challenge. Therefore, majority of this work dealt with studies of the uncertainties related with the detection of protons. However, for the sake of completeness estimates on the electron detection system are also provided. Due to the fact that the final iteration of the drift detector was not manufactured and the need for optimization of the magnetic field coils for the superconducting setup, it should be noted that the uncertainties on these systematics are not final and would need to be repeated once everything is finalized. Nonetheless, this work does aim to provide solid steps into the calculation of final numbers for these systematic effects.

6.4.1 Number of Required Bins

Since NoMoS inevitably is a position sensitive experiment, the first and foremost investigation has to be the investigation of the number of bins required by the detector. As the Transport function is computationally quite intensive, the focus of these investigations was only limited towards the drift direction axis of the detector. In theory, this is quite reasonably achieved by a 2D pixel detector by integrating over the second dimension in post-data analysis as doing so on the readout may increase the overall capacitive noise or the hit processing time depending upon whether it is performed on the hardware or the software side.

For the case of protons, different numbers of bins in the drift direction were investigated by doing a least square analysis of different values of the observable a while keeping everything else constant. Then the fit results, along with their corresponding error bars, from different bin numbers could be compared with each other. Figure 6.7 shows the resulting deviation $\Delta a/a$ caused by varying bin numbers. While all the points are within error bar of 0, it should be noted that with increasing bin numbers, the size of the uncertainty on the fit results gets smaller.

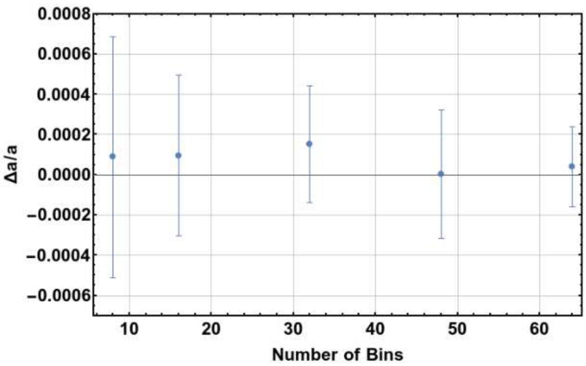

Figure 6.7: The results of $\Delta a/a$ for varying number of bins in the drift direction.

A similar study was also conducted for the case of electrons, where as before the absolute uncertainty Δb introduced by the choice of number of bins was investigated. As before, a similar pattern was observed, where the error bars on the fit results shrink as the number of bins in the drift direction increases, as can be observed in Fig. 6.8.

Considering the two results, it is recommended to use at least 64 or higher number of bins for the main drift detector. For the case of this work, the number of bins in the drift direction were chosen to be 64 for the interest of saving some time and computation power as higher bins require more time and consequently more computation power. Furthermore, systematics which introduce an uncertainty on the observables that is bigger than that introduced by the choice of number of bins of the detector, can be investigated by lowering the number of bins for the drift detector to save some

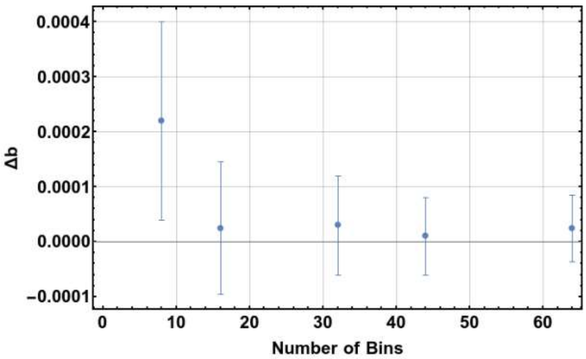

Figure 6.8: The results of Δb for varying number of bins in the drift direction.

time.

6.4.2 Sensitivity to Bins Crashing

A silicon detector is a very sensitive instrument and there are times when it may not function as intended. This includes the possibility of different pixels or bins of the detector malfunctioning and crashing. Since the momentum of the particles is mapped to a position on the detector, the drift distance spectrum as a consequence is also sensitive to the malfunctions of the bins. However, this sensitivity is not uniform throughout the drift distance axis and the fits should be more sensitive to the flanks of the spectrum than the peak or the edges.

To substantiate the aforementioned claim, the fit for 64 bins where only the value of the observable was changed was repeated by systematically deleting 4 bins at a time and seeing how it affected the uncertainty of the fit. For regions where the spectrum is more sensitive the uncertainty of the fit should be higher when those bins are excluded and vice versa lower for regions where the drift distance spectrum is not as sensitive to the malfunction of the detector bins. Figure 6.9 shows the result of this sensitivity analysis, where Fig. 6.9a shows how the uncertainty on the fit changes as 4 bins are systematically deleted or "made non-functional". Two maxima could be observed, which when plotted on the drift distance spectrum show the two regions where the sensitivity is the highest. The location of the two maxima in the drift distance spectrum of the protons is shown in Fig. 6.9b, by marking them in a different colour than the rest of the spectrum at the detector.

Similarly, the result of the sensitivity of the bins within the drift distance spectrum of electrons is shown in Fig. 6.10. Interestingly, for the case of electrons, the detector has an even higher sensitivity for the case of the falling flank compared to the rising one (compared to that of the proton spectrum) as seen in Fig. 6.10a. As before the two maxima are plotted on top of the drift distance spectrum for electrons obtained

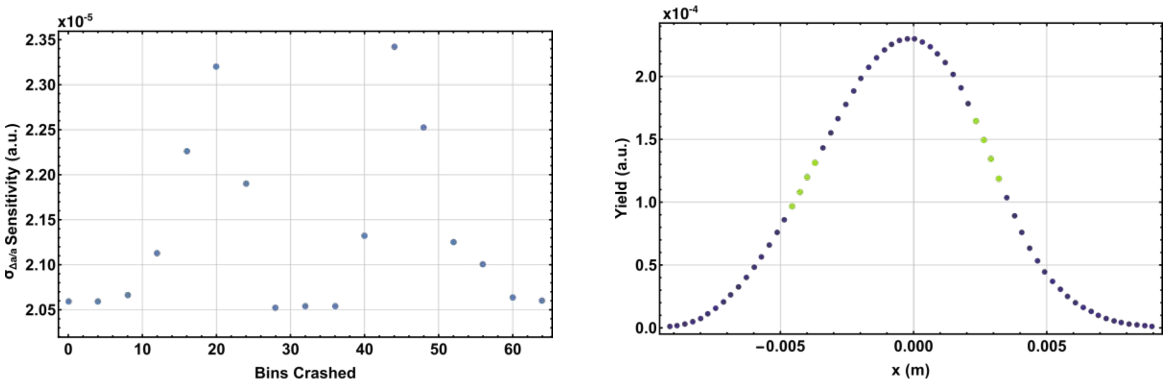

(a) Change of uncertainty on the fit results when 4 bins at a time from 0 to 64 are made to be non-functional. The two peaks represent the regions where the drift spectrum is most sensitive.

(b) Drift distance spectrum of the protons at the detector obtained from the Tranfer function of NoMoS, with the bins in green representing the most sensitive regions of the spectrum.

Figure 6.9: The sensitivity of the drift distance spectrum of protons on different regions of the detector in the drift axis.

by using the Transfer function as seen in Fig. 6.10b.

6.4.3 Backscattering from the Drift Detector

Backscattering at the drift detector is a systematic effect that is treated differently for the case of protons and electrons in NoMoS. This is because of the fact that due to the post-acceleration of the protons, backscattered protons have a probability to be reflected within the electrode to hit the detector again and be re-detected. Whereas for the case of electrons, backscattered particles drift towards the active aperture, where they are either detected by the active aperture or by the back detector (if present) of the setup.

Analytical Correction of Proton Backscattering

Due to the low detection threshold possible with the pLGAD, most backscattered protons will leave a detectable signal within the detector. For the desired entrance window of 1 nm Al_2O_3, simulations indicate a total of $\approx 0.013\%$ of particles will deposit a signal smaller than that of the sensor sensitivity when bump bonded to a Timepix3 readout (see Sec. 5.2). However, due to the fact that the protons are post-accelerated before detection, most of the protons will re-enter the detector causing a double hit. This is a systematic effect that needs to be corrected by Monte Carlo simulations or an analytical description of proton backscattering.

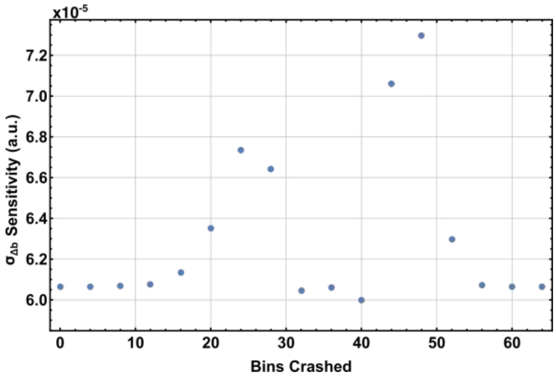

(a) Change of uncertainty on the fit results when 4 bins at a time from 0 to 64 are made to be non-functional. The two peaks represent the regions where the drift spectrum is most sensitive.

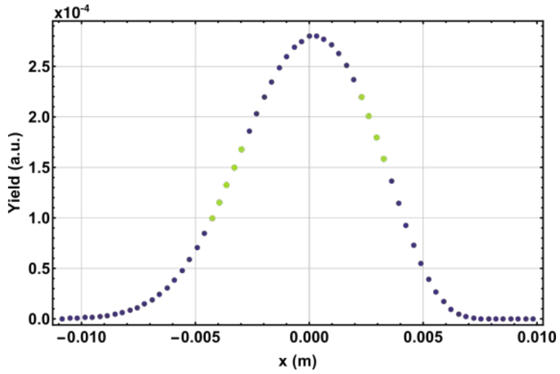

(b) Drift distance spectrum of electrons at the detector obtained from the Tranfer function of NoMoS, with the bins in green representing the most sensitive regions of the spectrum.

Figure 6.10: The sensitivity of the drift distance spectrum of electrons on different regions of the detector in the drift axis.

For this purpose, 1 million protons impinging upon the desired detector setup were simulated using IMSIL within an energy range of $15\,\text{keV} - 15.8\,\text{keV}$ with a step of $0.1\,\text{keV}$ and a polar angle range of $0° - 10°$ with a step of $1°$. It was found that the backscattering percentage of protons could be modelled reasonably well by the function:

$$\eta_{\text{prot. BS}}(T,\theta) = (c_1 * T\psi + c_2) * (1 - c_3 \frac{\sqrt{2}}{\sigma\sqrt{\pi}\psi} \exp^{-\frac{\theta^2}{2\sigma^2}} + (\frac{\theta\psi}{c_4})^2),\psi \tag{6.15}$$

where c_1, c_2, c_3, c_4 and $\sigma\psi$ are coefficients obtained from fitting the backscattering data. As modelled by the function, the energy part has a linear dependence whereas the polar angle has a more complex dependence which is an addition of an inverted half gaussian due to lowered backscattering at smaller angles as a result of channeling and a square-dependent part for higher angles. The results of the obtained fit for an exemplary angle and energy, along with the fit parameters are shown in Fig. 6.11 and Table 6.2 respectively.

As the backscattering description changes the spectrum in a way that a change of the observable $a\psi$ alone can not account for, this correction has to be included in the final spectrum. The uncertainty on the correction however, still needed to be studied. For this purpose, the correction function from Eq. 6.15 with the uncertainties in Table 6.2 were applied in the Transfer function. This lead to an error of:

$$\frac{\Delta a\psi}{a\psi} = 6.5 \times 10^{-3} \tag{6.16}$$

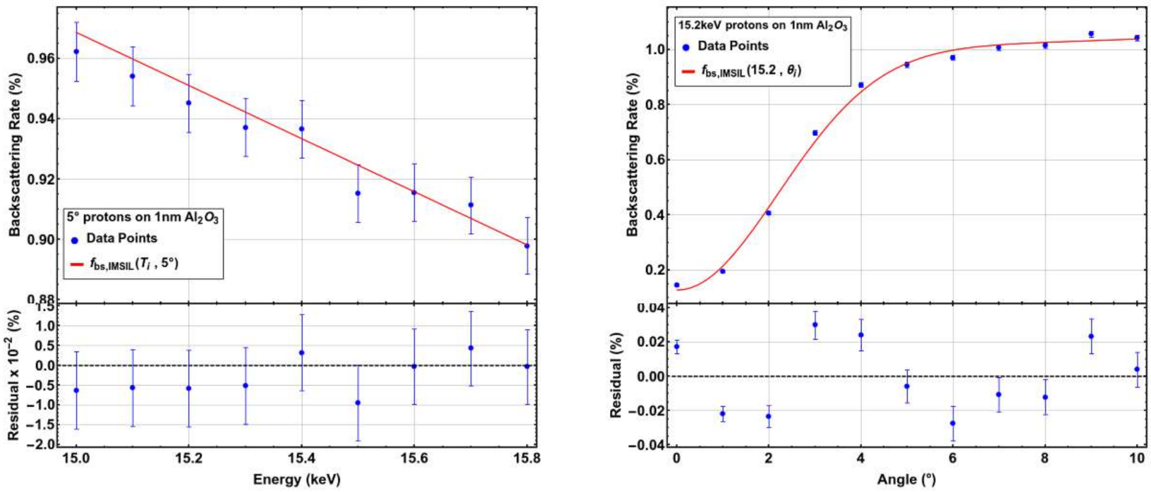

(a) The obtained fit results along with the data points for protons impinging on the detector at 5°

(b) The obtained fit results along with the data points for protons impinging on the detector at 15.3 keV

Figure 6.11: The obtained fit results and the fit residuals for one specific energy and angle obtained by using Eq. 6.15

This uncertainty is obviously higher than the final aim of the experiment, therefore the uncertainties on the fit parameters need to be a factor of 10 or smaller. For a first approximation of how it will effect the overall uncertainty, an additional fit was performed where the introduced uncertainties were a factor of 10 smaller, without simulating the actual statistics. This lead to a reduction of the uncertainty from 6.5×10^{-3} to:

$$\frac{\Delta a\psi}{a\psi} = 9.5 \times 10^{-4} \tag{6.17}$$

The first approximation provides a valuable input that the uncertainty on the correction can indeed get smaller as the fitted model matches the Monte Carlo results more. This is because due to the small backscattering rate, especially at lower angles,

Table 6.2: Fit Parameters for the backscattering distribution at the main drift detector.

Coefficient	Fitted Value	Fit Uncertainty
c_1	-0.093	0.006
c_2	2.42	0.09
c_3	2.39	0.02
c_4	56	9
$\sigma\psi$	2.18	0.015

more statistics do not lead to a direct $\sqrt{N}$ improvement in the fit results. Therefore, this translates to simulating 100x or more backscattering statistics for each angle and energy combination, which is out of the scope of this work as not only does it require precise knowledge of the final configuration of the manufactured drift detector but it also requires quite a substantial amount of time and computational power as well.

It should be noted that due to the low signal detection threshold of the pLGAD sensor concept, most of the backscattered protons will deposit enough energy to be detected. Therefore, it is imperative that the backscattering correction to the data be made. This can be done by either implementing a newer DAQ system which allows the storage of waveforms so some signals can be vetoed on the basis of some energy information obtained from the stored waveforms or by Monte Carlo simulations. Since an electrode design is not finalized, and the detector efficiency was calculated by taking a Timepix3 readout, we have opted to show the latter approach.

The probability density of the energy distribution of the backscattered protons looks similar for all impact energies, however a slight dependence on the impinging polar angle θ_{inc} was observed due to the effect of channeling. This dependence can be observed in Fig. 6.12, which shows the energy distribution of backscattered protons for different θ_{inc} with an impact energy of 15.8 keV. The x-axis in the figure represents the ratio of the backscattered proton energy to the impact energy while different lines represent the different θ_{inc}. It is observed that the distributions remain constant for the case of $\theta_{\text{inc}} \geq 2°$ where a peak can be seen at 0.1 (see Fig. 6.12b) with a gradual decrease before the distributions end at a value of 0.9, while there is a slight deviation for the case of $\theta_{\text{inc}} < 2°$. For those distributions, while a similar peak is seen at a value of 0.1, there is a second peak present near the end of the distribution. The source of the second peak most likely may be due to Rutherford scattering from the first few layers of the silicon crystal, whereas the rest of protons lose more energy within the crystal due to channelling increasing their penetration range.

The angular distribution of the backscattered protons, however had no extra dependencies and showed a peak at 45°, or 135° depending how the angle of the backscattered particle is measured, similar to that observed for electrons backscattering from a scintillator as discussed in [68]. Figure 6.13 shows the angular distribution of the backscattered protons obtained from protons that impacted the silicon detector with an energy of 15.8 keV at various angles θ_{inc}. Unlike the energy distribution, there is no additional angular dependence at smaller θ_{inc} and a peak is observed at 45°, where 0° is parallel to the impact angle of the original proton. To model the angular distribution, a rather simplistic model was used, that is given as:

$$\kappa(\theta_{\text{BS}}) = c_1 \sin\left(\frac{\theta_{\text{BS}}\pi}{90°}\right), \tag{6.18}$$

where the backscattered angle θ_{BS} is in degrees and c_1 is a scaling factor that can be obtained by fitting the histogram.

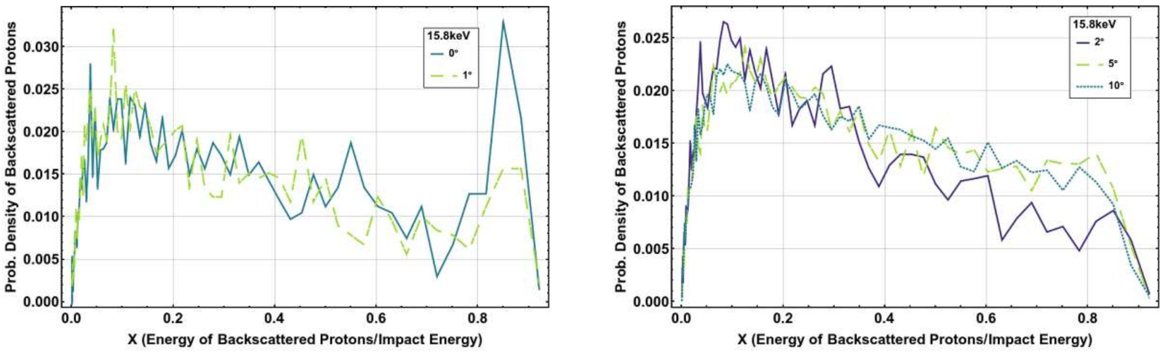

(a) $\theta_{\text{inc}} < 2°$

(b) $\theta_{\text{inc}} \geq 2°$

Figure 6.12: The energy distribution of the backscattered protons at different impact angles θ_{inc} and an impact energy of 15.8 keV. The x-axis represents the ratio of the backscattered proton energy to the impact energy.

For a Timepix3 readout coupled to a pLGAD, Weightfield2 simulations show that the proton signal will take a total deposition time of $\approx 3\,\text{ns}$ (see Sec. 4.3.2), additionally, the Timepix3 readout is capable of a timing resolution of 1.5 ns [121]. Therefore a preliminary analysis of the worst case scenario reveal that a proton impinging the detector with $\approx$15.8 keV at 1° (as due to the neutron beta decay no protons will impinge the detector at 0°) will be backscattered with a gyration radius of $\approx$1.2 cm at 45° and a kinetic energy of 13.4 keV. If the gyration radius is ignored for the sake of simplicity, it can be shown that the proton will take a total time of $\approx 0.5\,\mu\text{s}$ to drift a distance of $2 \times L_{\text{electrode}}$. Here the length of the electrode $L_{\text{electrode}}$ is assumed to be 40 cm with a uniform electric field of the same potential within the electrode as a first order approximation. Therefore, it is a safe assumption that the proposed drift detector will be able to distinguish double hits of the backscattered protons and the correction can be applied by conducting backscattering studies. Furthermore, taking the most probable gyration radius into account, certain conditions on the detector pixels could be set to account for a coincidental signal hit on pixels where a backscattered proton should not be expected. However, as this correction depends on the design of the electrode, it is out of the scope of this work.

6.4.4 Analytical Correction of Electron Backscattering

In principle the correction of electron backscattering should be easier than the case of protons due to the presence of both a back and backscattering detector to provide veto signals. However, it should be noted that backscattered electrons can be backscattered once more from the veto detectors and have a chance to reach the drift detector to be detected. Therefore, an analytical correction for electron backscattering in the

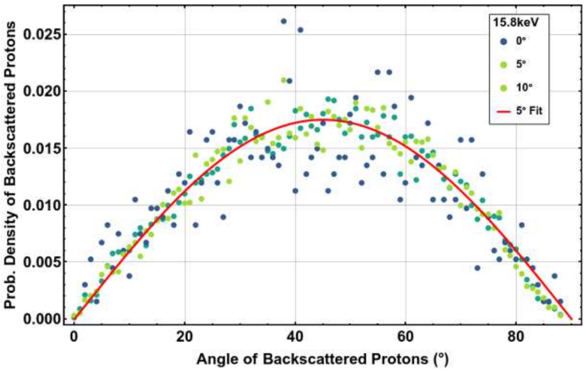

Figure 6.13: Angular distribution of the backscattered protons at different impact angles θ_{inc} and an impact energy of 15.8 keV. The red line exhibits a fit to the angular distribution of the backscattering protons with an impact angle θ_{inc} of 5° according to Eq. 6.18 with a c_1 of 0.0175.

obtained drift spectrum is required.

To get a first estimate of the correction and the associated uncertainty, electron backscattering studies were conducted using CASINO on the pLGAD detector geometry. The choice of using CASINO over Geant4 was made as setting up Geant4 along with the appropriate physics libraries takes a considerable amount of time. As a consequence, these investigations were not foreseen to be performed in Geant4 as a part of this work. 100,000 electrons impinging on the drift detector with energies ranging from $1 - 780$ keV in steps of 60 keV and the angles from $0 - 45°$ in steps of 5° were simulated. However, due to the sharp decrease in backscattering in the step from 1 keV to 61 keV, further energy values in steps of 10 keV with an additional value at 5 keV were simulated within that regime. The backscattering rate was found to fit a cubic dependence on the polar angle, which could be perceived as a reduced Taylor expansion of Eq. (3.2) taken from Ref. [68]. The reduced equation could be stated in terms of energy dependent coefficients as:

$$\eta_{\text{BS, DriftDet.}}(\theta,\psi E_e) = c_1(E_e) + c_2(E_e)\theta^3,\psi \tag{6.19}$$

where c_1, and c_2 are the aforementioned energy-dependent coefficients. The values of the coefficients can be found in Appendix C. Fig. 6.14 shows the backscattering rate with the fit from Eq. 6.19 and the fit residuals.

To model the backscattering correction within the transfer function, the energy dependent coefficients were cubicly interpolated between the simulated energy values for different angular dependence fits in order to smooth out any outliers. To obtain a first value for the uncertainty on the backscattering correction, this was an adequate assumption as electron backscattering would be further corrected by data obtained from the backscattering detector at the active aperture. To study the effect of the

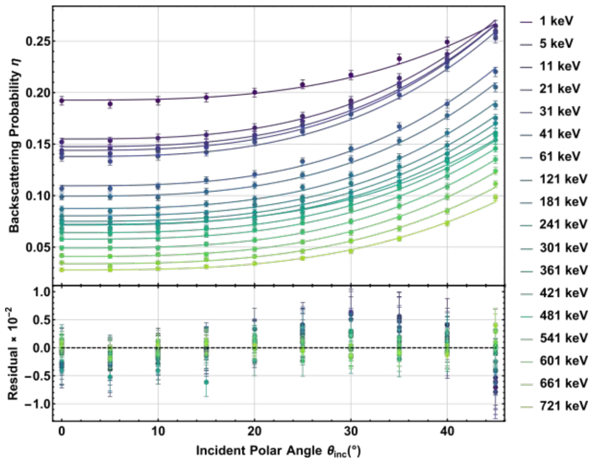

Figure 6.14: Angular dependence of electron backscattering from the drift detector for various energies. The coloured lines show the fit results with the appropriate energy dependent coefficients in Eq. (6.19). Please note the scale of the residuals is different from that of the backscattering probability.

uncertainty, the fit uncertainties for the energy dependent coefficients was used, see Fig. 6.14. This gave an absolute uncertainty on Δb of:

$$\Delta b = 6.3 \times 10^{-4} \tag{6.20}$$

This number could be further shrunk by decreasing the uncertainty on the fitting coefficients with the help of more statistics as the quality of the fit for the energy dependent coefficients will improve. From this study, a total of one million particles for each point should be sufficient to reduce the number by a factor of approximately 3, as to not increase the overall uncertainty budget of the experiment.

Furthermore, as already pointed out, the Monte Carlo correction to the final data would be helped by the veto signals from the backscattering detector. As the veto signals from the backscattering detector could be used to rule out electrons from Time of Flight and energy information of the impinging electron, which for the case of NoMoS can be obtained by the spatially resolved drift distance spectrum.

Correction of Electron Backscattering from Backscattering Detector

Electrons which backscatter from the drift detector will go through the $R \times B$ region once more and arrive at the backscattering detector provided they do not hit the vessel walls, where they could go through one of the following scenarios:

- Impinging electrons are detected by the backscattering detector and are absorbed by the detector

- Impinging electrons are backscattered from the backscattering detector

- Impinging electrons pass through the aperture opening and are either reflected by the magnetic filter or pass through it, depending on their polar angle θ, to arrive at the back detector (in stand alone configuration).

For the first case, the associated mathematical correction can be applied to the backscattering correction as discussed in the previous section, provided it is corrected for electrons which backscatter from the backscattering detector (case two). Similarly, the correction introduced by the third scenario needs to be studied as well. Therefore, Monte Carlo tracking simulations were performed to determine the angular and energy distribution of the electrons which were either backscattered from the backscattering detector or reflected from the filter and managed to hit the drift detector a second time.

For the Monte Carlo simulations, the impinging electrons on the drift detector were weighted with respect to their backscattering probability given by Eq. (6.19) and the energy and angle of the backscattered electrons were generated by playing dice in two dimensions over the interpolated energy and angular distributions obtained from Casino simulations of the drift detector as a function of the original electrons impinging energy and angle.

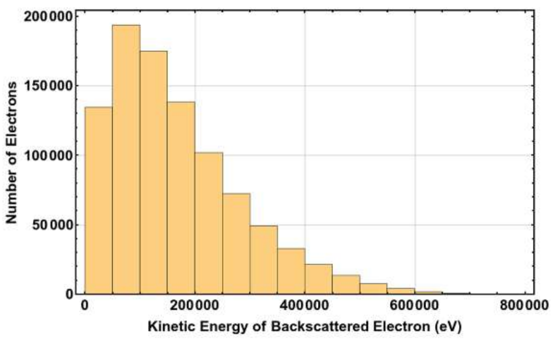

(a) Energy distribution of the backscattered electrons

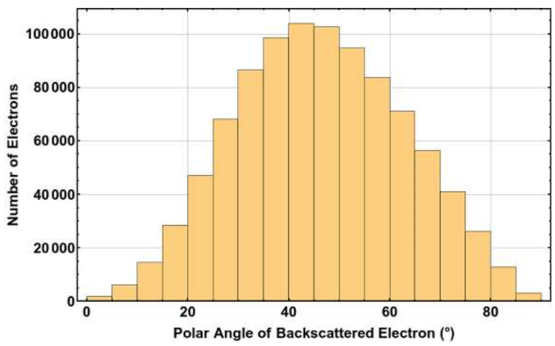

(b) Angular distribution of the backscattered electrons

Figure 6.15: The energy and angular distributions of the electrons after they backscatter from the drift detector and before moving towards the aperture region once more.

Figure 6.15 shows the energy and angle distribution of the backscattered electrons used for the Monte Carlo simulation with a total statistics of 1×10^6 particles. From the results of the simulation, it was observed that $\approx 96\%$ of the backscattered electrons made it back to the aperture, whereas the rest hit the walls of the experiment within the $R\!\!\!/\times B\!\!\!/$ region. The backscattered electrons which did reach the aperture were then further divided into two categories:

- Backscattered electrons that go through the aperture opening
- Backscattered electrons that hit the backscattering detector at the aperture

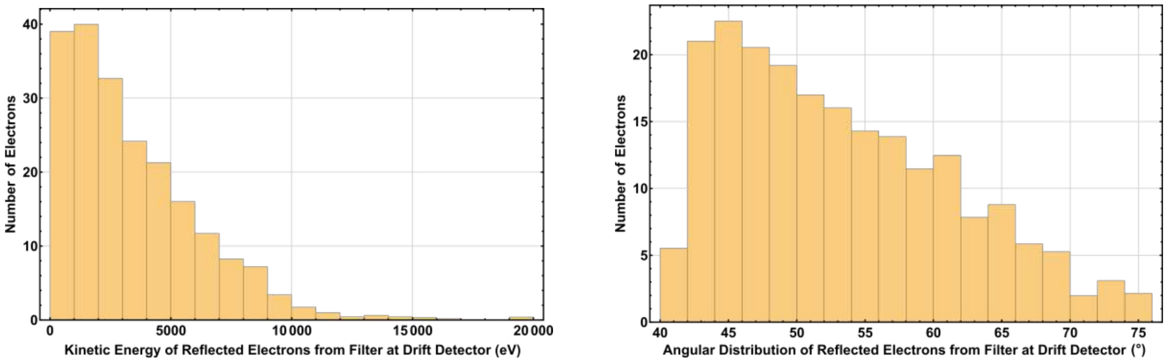

(a) Energy distribution of the backscattered electrons at the drift detector

(b) Angular distribution of the backscattered electrons at the drift detector

Figure 6.16: The energy and angular distributions of the backscattered electrons which do not hit the backscattering detector but instead are reflected from the filter and arrive at the drift detector again.

Backscattered electrons that go through the aperture opening can then either be reflected back from the filter or pass through it, depending on their polar angle θ, and finally impinge on the back detector if the experiment is in its stand alone configuration. While the electrons that pass through the filter are not an issue for the experiment, those which are reflected can pass through the aperture once again and hit the drift detector a second time without a corresponding veto signal on the backscattering detector. Figure 6.16 shows the angular and energy distribution of the backscattered electrons which reach the drift detector once again after being reflected from the filter coils and passing through the aperture opening. From the figure it can be seen that the energy of the electrons which reach the drift detector again after being reflected from the filter is very low compared to the overall kinetic energy range observed for the backscattered electrons (see Fig. 6.15a). Furthermore, the θ angle distribution is also restricted up to 75°.

To ascertain the correction introduced by these additional electrons on b, their spatial distributions at the drift detector after normalization (as shown in Fig. 6.17) was added with the drift distance spectrum obtained from the Transfer function. This convolution was then compared to the reference spectrum as discussed earlier in Sec. 6.2 and led to an overall correction on b of:

$$\Delta b = -1.7 \times 10^{-4} \tag{6.21}$$

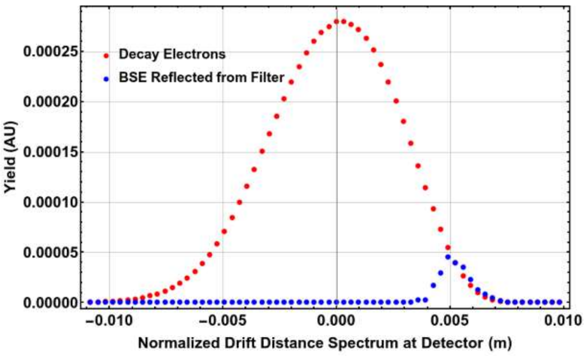

Figure 6.17: The normalized spatial distribution of the backscattered electrons (BSE) to the total number of decay electrons at the drift detector which do not hit the backscattered detector but instead are reflected from the filter after passing through the aperture opening. For comparison, the drift distance spectrum of the original decay electrons is shown in red.

The magnitude of the correction is quite small, however it makes sense as only 0.02% of the backscattered electrons make it back to the drift detector for a second hit after being reflected by the filter.

As for the backscattered electrons that do end up being detected by the backscattering detector, some will be backscattered once again and make their way to the drift detector. To avoid any confusion, these electrons will be referred to as the second backscattered electrons or SBE within this section. These electrons were also studied with the help of Monte Carlo tracking simulations by playing dice over the backscattered electrons arriving at the aperture with the probability of backscattering obtained by using Eq. (3.2), as both the back and backscattering detector are scintillator based. The resulting SBE were then tracked further as they drifted towards the drift detector.

Figure 6.18 shows the energy and angular distribution of the SBE at the drift detector after being backscattered firstly from the drift detector, and then the backscattering detector. The energy distribution is narrower than that of the decay electrons that were backscattered from the drift detector. Also the angular distribution apart from being restricted to a smaller range, has a peak at $\approx 75°$ as opposed to the $45°$. Majority of these contributions arise from low-energy electrons as electrons with a high energy and angle are more prone to hit the walls of the $\vec{R} \times \vec{B}$ section due to their large gyration radii and drift.

As before, the systematic correction introduced by the SBE was studied by summing the results obtained from a simulation with the drift distance spectrum obtained by using the Transfer function. As it can be seen in Fig. 6.19a the contribution of the systematic effect can not be explained by variation of $\vec{b}$ alone as the SBE experience a

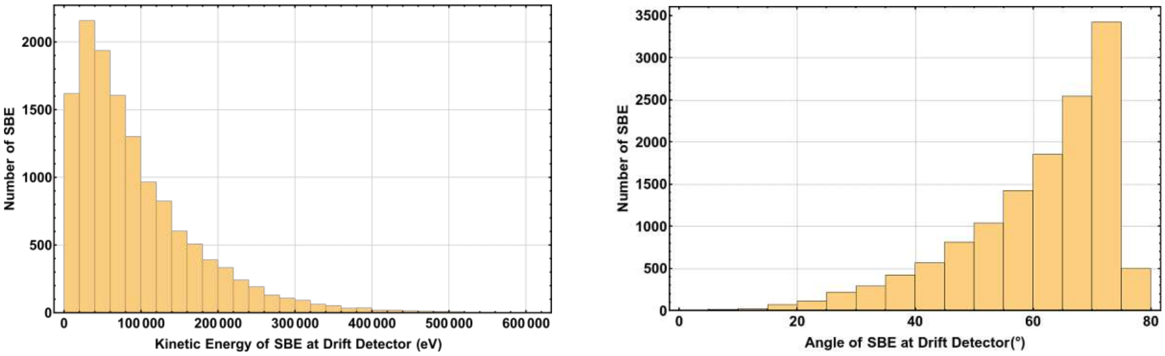

(a) Energy distribution of the SBE at the drift detector

(b) Angular distribution of the SBE at the drift detector

Figure 6.18: The energy and angular distributions of the SBE which hit the drift detector for a second time after being backscattered from the backscattering detector

large drift due to them passing through the $R \times B$ region three times. Furthermore, as seen in Figs. 6.19b and 6.19c, the major contribution to the systematic effect is caused by SBE that have a kinetic energy < 100 keV as electrons with higher energies experience a large enough $R \times B$ drift to be separated from the original drift distance spectrum. Therefore to properly take this systematic effect into account, a drift distance detector capable of performing calorimetric measurements is highly recommended for the case of measurement of electrons.

For a detector capable of resolving signals calorimetrically down to 100 keV, the systematic uncertainty where an additional veto is done on the signal if the deposited energy is more than expected at that particular detector position is:

$$\Delta b = -6 \times 10^{-4} \tag{6.22}$$

However, this correction can be reduced even further to 10^{-5} level if the detector is capable of doing calorimetry down to the 10 keV level.

It should be pointed out that due to the design of the pLGAD detector, it should be capable of doing calorimetry as long as the detector wafer is thick enough to stop the impinging electrons. For reference, a 100 keV electron has a penetration depth of $\approx$ 80 µm in Silicon whereas this is reduced to $\approx$ 2 µm for a 10 keV electron. Consequently, a detailed characterization of the gain with electron sources of varying energy would have to be performed to determine the gain values for the signal of the impinging electrons and apply the correction in an appropriate manner.

For the case of high-energy electrons, to do calorimetry, two options are recommended. Either a scintillating fiber detector is installed behind the pLGAD to stop the high energetic electrons. In this case, both the pLGAD and the scintillating fibers would have to be read from the side instead of from the bottom to ensure an accurate

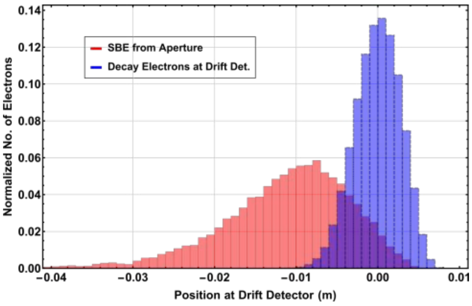

(a) Entire drift distance spectrum of SBE and decay electrons

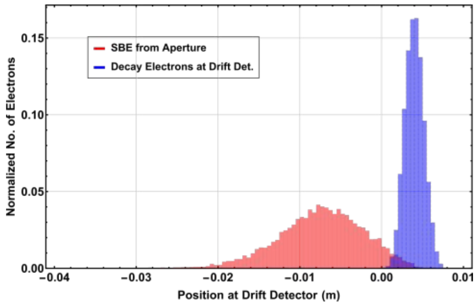

(b) SBE and decay electrons that have a kinetic energy <100 keV

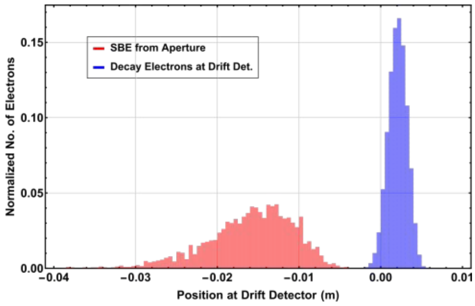

(c) SBE and decay electrons that have a kinetic energy in the range of 100 keV to 200 keV

Figure 6.19: The normalized drift distance spectrum of the SBE compared to that of the electrons from neutron beta decay for different kinetic energy ranges. It should be noted that both spectra in each individual plot are normalized with the total counts of the respective histograms and not with the overall number of simulated particles. This is done only to visualize the SBE contribution to the final drift distance spectrum. This is the reason why the y-axis values of the first plot differs from the plots (b) and (c).

calorimetric value of the impinging electron. This is because an electron with 800 keV of kinetic energy has a penetration depth of $\approx$ 1.8 mm in silicon. Alternatively, a wafer-to-wafer bonding approach as outlined in [122, 123] could also be utilized, where a high absorbing wafer such as GaAs could be bonded to the end of the pLGAD without the use of any other additional material to do calorimetry.

6.4.5 Correction of Electron Backscattering from the Back Detector

As already discussed in Section 3.3.1, backscattered electrons from the back detector have a possibility to reach the drift detector. Using the angular and energy distribution shown in Fig. 3.6 and 3.5a, a Monte Carlo tracking simulation was performed to see the influence of backscattered electrons from the back detector on the drift distance spectrum. Of the total particles that impinge on the drift detector, only 0.005%

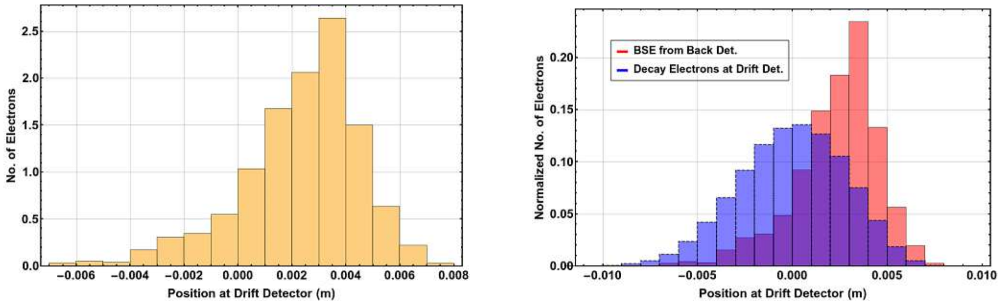

(a) Spatial distribution of electrons backscattered from the back detector at the main drift detector.

(b) Normalized position spectrum of backscattered electrons (BSE) from the back detector in comparison to that from decay electrons.

Figure 6.20: The drift distance spectrum of the electrons backscattered from the back detector which pass through the filter and the aperture to hit the main drift detector. It should be noted that both spectra are normalized with the total counts of the respective histograms and not with the overall number of simulated particles. This is done only to visualize the contribution of the backscattered electrons to the final drift distance spectrum.

particles hit the drift detector after backscattering from the back detector and passing through the aperture. This leads to a correction on $b\!\!/$ of:

$$\Delta b\!\!/ = -4.3 \times 10^{-4} \tag{6.23}$$

which is relatively high considering the overall number of particles that do manage to reach the detector. However, the magnitude of the uncertainty can be explained as the majority of the backscattered electrons fall on the flank of the drift distance spectrum where the spectrum is most sensitive to changes in values of b, as seen in Fig. 6.20b. Nonetheless, the uncertainty is well under the overall uncertainty on the observable that is wished to be reached by the experiment. However, this uncertainty can be further studied by moving the back detector closer or further away from the decay volume. E.g. for a back detector positioned at 10 cm from the decay volume, the correction on $b\!\!/$ increases to $\Delta b\!\!/ = -5.5 \times 10^{-4}$. The uncertainty can be further reduced by correcting it with the help of Monte Carlo simulations and adding more statistics. Additionally, the validity of the Monte Carlo corrections can be verified by moving the back detector to various set positions away from the decay volume and taking additional data during the run of the experiment.

6.5 Drift Detector Efficiency Correction

As already discussed in Sec. 5.2, there are multiple factors that determine the efficiency of the main drift detector in NoMoS. Furthermore, due to the additional dependence of angle and energy, the efficiency is not unity albeit near to it. Even then, due to the nature of NoMoS, any angular and energy dependence has to be studied to determine the correction as well as the uncertainty of the correction. For this purpose, the efficiency of the pLGAD coupled with the Timepix3 system at a detection threshold of 50 primary electrons was simulated (500,000 particles for each combination) using IMSIL for multiple combinations of energy and angles.

Figure 6.21 shows exemplary plots of the energy dependence of the efficiency of the drift detector for an angle of 10° in Fig. 6.21a, and of the angular dependence of the efficiency at an energy of 15 keV in Fig. 6.21b, with statistical error bars and an applied fit for correction. The statistical error bars consequently will be huge due to summation of the generated e-h-pairs histogram (see Sec. 5.2), due to the fact that the efficiency of the pLGAD is so high i.e. the threshold for primary electrons required for a good signal to noise separation is low. Consequently, this is also the reason why the error bars of the data points is bigger than the actual correction. However, to model an analytical behaviour, the backscattering correction fit was used for the data matrix, where the energy has a linear dependence and the angle has a half Gaussian dependence as shown in Eq. 6.15. This was done as the efficiency is to some degree also effected in the same behaviour by channeling effects as backscattering. Nonetheless, to simplify the fitting equation further, the θ^2 dependency i.e. the c_4 term in Eq. 6.15 was dropped. Due to the large size of the statistical error bars, it made sense to use a model that had a physics explanation behind it. For a first order approximation, the error bars were left symmeteric even though a negative value is unphysical because it means that the detector has an efficiency of $>$100%. The values used for the fit are given in Table 6.3.

Table 6.3: Fit Parameters for the signal loss (1-Efficiency) of the drift detector for impinging protons.

Coefficient	Fitted Value	Fit Uncertainty
c_1	-8.2$\times$10^{-4}	0.0013
c_2	0.026	0.02
c_3	1.08	0.22
$\sigma\psi$	2.02	0.4

Applying the correction, leads to a relative correction of $\Delta a/a$ of 1.5×10^{-4}, which is quite small compared to the desired precision for the experiment. However, applying

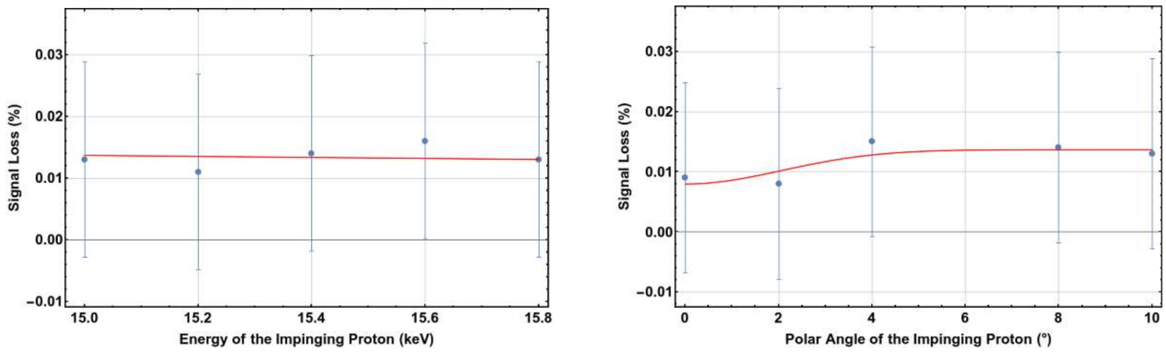

(a) Energy dependence of the drift detector efficiency at 10°

(b) Angular dependence of the drift detector efficiency at 15 keV

Figure 6.21: The energy and angle dependence of proton efficiency of the pLGAD at 50 primary electron threshold. The two cases are shown as the pLGAD will have the lowest efficiency for protons impinging the detector at 10° and 15 keV. For further details regarding the error bars and the applied fit (red line) see text.

the uncertainty to the correction lead the error to jump to a value of:

$$\frac{\Delta a\psi}{a\psi} = 6.2 \times 10^{-4} \tag{6.24}$$

This was an expected behaviour due to the large uncertainty associated with the fitting parameters. As a consequence, a factor of 100x more statistics is required for the error bars to be small enough to reduce the uncertainty by a factor of 10. However, unlike the backscattering simulations, this requires even more time and computation power. This is because to extract efficiency a full track analysis of all the proton interactions within the detector material have to be performed. This exponentially increases the amount of time, computation power and storage space required for such a calculation and there are multiple factors that go into the calculation of the efficiency, as explained in Sec 5.2. As stated before, the aim of this work is to provide a first order estimation that will need to be improved upon once a drift detector is manufactured and characterized. Therefore, it is recommended to start these studies, both for the backscattering correction as well as the efficiency one, at the earliest possible moment after the manufacturing of the drift detector, due to the high amount of statistics required to have the uncertainty value be in an acceptable range. Similarly, this study should also be performed for the case of electrons. But in this case fewer number of particles compared to the protons will be required due to the absence of channeling effects.

6.6 Positional Uncertainties of the Drift Detector

Due to the position-sensitive nature of NoMoS, uncertainties in the placement of the drift detector need to be minimized. However, as the position of the drift detector has to be known not with respect to the geometric centre of the experiment but rather to the central magnetic field line, the placement of the drift distance detector depends on the magnetic field mapping of NoMoS, which is a non-trivial task. Therefore, a study was performed of the relative uncertainty introduced on the fitted correlation parameters, a and b, due to a potential misalignment of the detector with respect to both axis as well as due to a possible tilting of the detector in the plane parallel to the axis in which the decay products beam propagates.

6.6.1 Detector Misalignment in the Drift Direction

To study the uncertainty in the observables introduced by a potential detector misalignment in the drift direction, a slight shift of 2 µm was introduced in the detector bins along the drift axis and the consequent spectrum fitted with varying observable values to find a chi-square minimum. This lead to an absolute uncertainty Δb of 5×10^{-3} and a relative uncertainty $\Delta a/a$ of 1.7×10^{-2}.

As both of the stated uncertainties are far greater than the desired precision of the experiment, even with a very small misalignment of 2 µm, it is evident that there is a need to use an additional fit parameter to account for detector misalignment effects. As a consequence, multiple misalignments in both spectra of up to 1 mm were introduced to get a 2D matrix of chi-squares with different values of observables and misalignments. The uncertainty introduced by the potential misalignment grew or shrunk depending upon the magnitude of the effect. However, this also meant that a new manual fitting method was required.

Introduction of Additional Fit Parameters

The manual search for an additional fit parameter utilizes the same ansatz as the one used for the introduction of a manual chi-square parabolic fit i.e. there is a single global minimum where the least square analysis gives the smallest possible value for the change of the observables and/or systematic effects. Therefore, if a second dimension is added to the variable being changed for the minimization of the chi-square distribution, it will lead to an elliptic paraboloid with a certain rotation depending on the correlation between the fitted parameters. For the case of detector misalignment, this could be seen by looking at the 1-dimensional cuts of the χ^2-distribution (see Sec. 6.2). Figure 6.22 shows the aforementioned 1-dimensional cuts, with a parabolic fit applied according to Eq. (6.13).

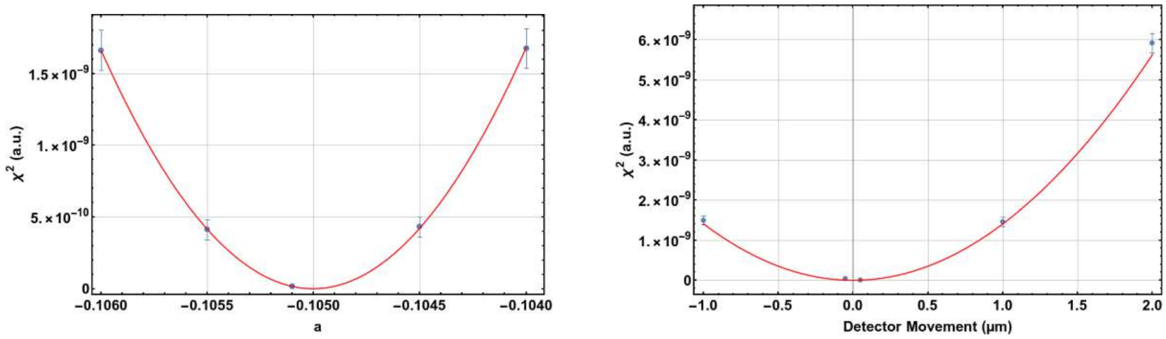

(a) Change of χ^2 by variation of a for no detector misalignment i.e. $s_{\text{mov}} = 0$. A $\Delta a/a = 3 \times 10^{-5}$ is obtained from the fit

(b) Change of χ^2 by variation of detector misalignment for $a = -0.105$. A $\Delta s_{\text{mov}} = 1 \times 10^{-12}$ is obtained from fit

Figure 6.22: 1-dimensional cuts for the change of χ^2-distribution by detector misalignment in the drift direction obtained by variation of the electron-antineutrino correlation coefficient parameter a and a potential misalignment of the detector s_{mov} with respect to a reference spectrum for protons ($a = -0.105$ and $s_{\text{mov}} = 0$). The red line is the result of a 1D parabolic fit (Eq. (6.13)) as discussed in Sec. 6.2

The following fitting equation for a rotated elliptic paraboloid is used to find a minimum in the two dimensions (a and s_{mov}) by the process of a manual search:

$$\chi^2_{fit2D} = \chi_{\text{offset}} + \left(\left(\frac{(\Delta a - a)\cos\theta_{\text{rot}} - (\Delta s_{\text{mov}} - s_{\text{mov}})\sin\theta_{\text{rot}}}{a_{\text{offset}}} \right)^2 + \frac{(\Delta a - a)\sin\theta_{\text{rot}} + (\Delta s_{\text{mov}} - s_{\text{mov}})\cos\theta_{\text{rot}}}{s_{\text{movOffset}}} \right)^2 \Bigg) \Bigg(\tag{6.25}$$

where s_{mov} is the second systematic parameter, θ_{rot} is the angle by which the elliptic paraboloid is rotated, $\chi_{\text{offset}}, a_{\text{offset}},$ and $s_{\text{movOffset}}$ are offsets for the paraboloid so it is shifted in the respective coordinates. It should be noted that due to the nature of the equation, the parameters will have some correlation with each other. However, for a first check, this method will show that a fitting parameter can indeed reduce the overall systematic uncertainties within the experiment. To verify if a 2D fit can account for misalignment effects at the detector, a manual fit in accordance to Eq. (6.25) was attempted with detector misalignments of 0, ±50 nm, ±1, 2, 5, and 10 μm for protons, where the a value for these data sets was varied to find the minimum when the misalignment effects were unknown and the distribution could only be explained by the variation of the observable a alone. The coarseness of the steps was a consequence of the computational intensity required for the generation of a single data set in Fig. 6.23b.

Figure 6.23 shows the fit results to the aforementioned data set as well as a zoomed out contour plot of the fit function to show the rotated elliptic paraboloid shape. The fit gave a result of $\Delta a/a = 2.4 \times 10^{-4}$ and $\Delta s_{\mathrm{mov}} \approx 0(< 10^{-20})$ for a reference spectrum with no misalignment. By changing the reference spectrum to one that was shifted, it was found that the additional fit parameter can decrease the k-factor of potential detector misalignment in the drift direction by a factor of 9 for the case of a misalignment of 1 µm and 2 µm.

Similarly, the fit was repeated for the case of electrons with the replacement of the data at 10 µm for a point at 1 mm instead. It was seen that the k-factor for the uncertainty introduced on the detector misalignment in the drift direction on b for different misalignments can be reduced by a factor of 11 for the case of 1 µm and 2 µm misalignment effects. From these investigations, it is recommended to have detector

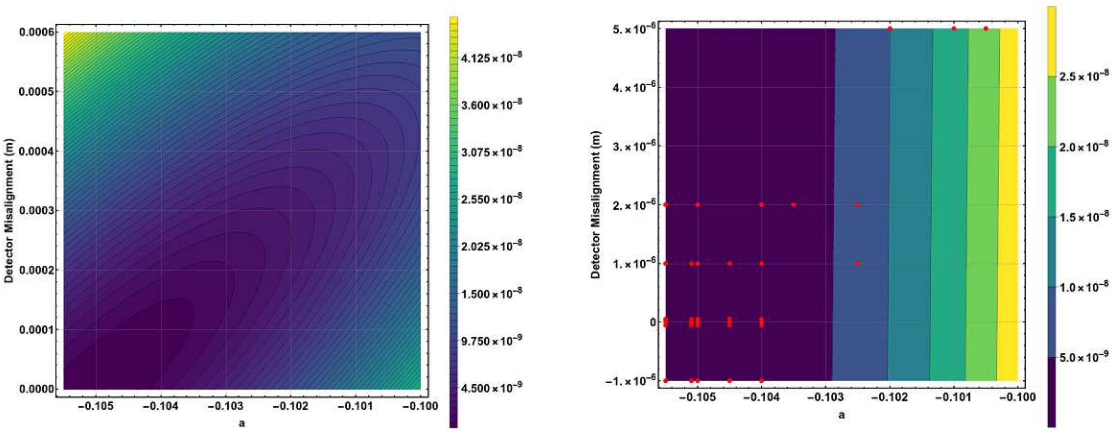

(a) Zoomed out contour plot of the fitted function to show the elliptical paraboloid structure.

(b) Fitted function to the data points with data points shown in red apart from the points at 10 µm. Please note the different contour shades compared to 6.23a

Figure 6.23: First attempts at a multivariable fit using Eq. 6.25 for the proton spectrum and detector misalignment effects. The fit gives a minimum value at $\Delta a/a = 2.4 \times 10^{-4}$ and $\Delta s_{\mathrm{mov}} \approx 0$

misalignment effects in the drift direction down to the order of 10 µm with the use of an additional fit parameter. It should be further noted that even though the additional fitting parameter could only reduce the uncertainty effects by a factor of ≈ 10 for electrons and protons, many other uncertainties in the overall uncertainty budget of systematic effects could be reduced by the use of an additional fit parameter as well.

It should be noted that in a full description and final data analysis, it is recommended to use a more refined minimization technique to find the global minimum as this approach gets far too complicated if there are more than 2 fit parameters being used. Furthermore, this technique also has the caveat of depending on the number of points in the fitting grid, where having more points in an equidistant matrix covering a wider phase space should lead to even better fit results. To investigate this claim a mathematical approach was taken by performing different fits using the elliptical paraboloid description obtained from the proton drift distance spectrum 2D fit (see Fig. 6.23a) on data taken at three different detector misalignment values by varying only the value of a between -0.106 and -0.1 in steps of 0.0005. This gave 3 different data sets at 0 mm, 0.5 mm, and 1 mm of detector misalignment, which were then fitted separately using a non-linear model fit routine with Eq. (6.25) as the fitting function in Mathematica to obtain values of a and s_{mov}. This resulted in an improvement by a factor of 2.7 on the obtained fitted parameters for the 1 mm data case compared to the 0 mm case as the data points for the fit were not confined to the plane of the elliptical paraboloid where the slopes of the paraboloid do not change sharply i.e. near the absolute minimum ($a = -0.105$ and 0 mm for this case) where the induced change in the χ^2-distribution is small.

Aperture Dependence of Detector Misalignment

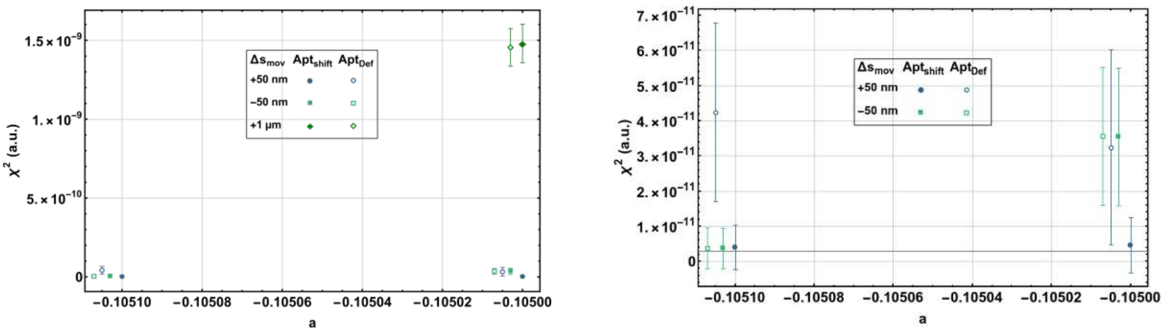

(a) (b)

Figure 6.24: Comparison of χ^2 values obtained for detector misalignment s_{mov} at two different a values for a NoMoS configuration where the centre of the aperture is placed at different positions compared to the recommended aperture position of 9 mm (represented by $\mathrm{Apt_{Def}}$). Figure 6.24b is the zoomed in version where the value of a detector misalignment of 1 μm is not shown. It should be noted that the values are shifted around the actual simulated a values of -0.105 and -0.1051 for the sake of clarity.

As the position of the aperture goes directly into mapping the decay products beam to the detector, a brief study to see the effects of aperture positioning on potential detector misalignments was also performed. The motivation for this study was to understand whether there is a correlation between the beams final position in the drift direction at the detector due to the placement of the aperture and potential detector misalignment effects. A potential correlation can be there as the flanks of the drift distance spectrum move due to the movement of the centre of the aperture opening in the drift direction.

Figure 6.24 shows the χ^2 values obtained at two different $a\psi$values for three different misalignment scenarios of the detector in the drift direction and two different positions of the aperture centre in the drift direction for the proton drift distance spectrum. The χ^2 values were obtained by comparison to the reference spectrum of the two aperture positions with no detector misalignment effects. By comparison of the solid points of the same colour with the hollow ones, it can be seen that detector misalignment effects in the drift direction are independent of the position of the aperture centre despite the sensitivity of the spectrum on the positions of its flanks. For the case of electrons, this investigation was not necessary as in general the magnitude of systematic uncertainties for protons is a factor of four or more higher than those of the electrons, therefore the effect will be similar if not smaller for electrons.

6.6.2 Detector Misalignment in the Non-Drift Direction

The decay products beam in the NoMoS apparatus can be resolved on to the pixel structure of the drift detector in 2D. However, as already argued before, due to the computational constraints, it is far more beneficial to have more bins in the drift direction than the non-drift one. Nonetheless, detection-related systematic effects such as misalignment in the non-drift direction could still introduce uncertainties in the final error budget. By using the transfer function, it was found that the total uncertainty introduced in the proton and electron spectrums for a misalignment of 1 µm is:

$$\frac{\Delta a\psi}{a\psi} = 5.3 \times 10^{-4} \quad \text{and} \quad \Delta b\psi = 1.4 \times 10^{-4}.\psi \tag{6.26}$$

This is quite low in comparison to the uncertainty introduced by the misalignment in the drift direction, and acceptable in terms of the overall accuracy goal of the experiment for the parameters. However, if needed, this uncertainty can be further reduced by the use of additional fit parameters.

6.6.3 Rotation of Detector in Drift Spectrum Plane

Apart from the alignment of the detector with respect to the central magnetic field line, it would still be susceptible to other misalignment effects such as rotation of the detector in the plane of the spectrum. This is an important effect to consider as a rotation in the drift spectrum plane will cause uncertainties in both the x and y position of the detector analogous to misalignment effects which as already discussed require additional fit parameters. In the superconducting setup of NoMoS, these effects for a rotation of 0.1° amounted to an uncertainty:

$$\frac{\Delta a}{a} = 9.9 \times 10^{-4} \quad \text{and} \quad \Delta b = 1 \times 10^{-4} \tag{6.27}$$

While the absolute uncertainty in b is small enough, the relative uncertainty in a is large enough to warrant a positioning system for the reduction of the uncertainty arising from rotation of the drift detector. For this purpose, it is recommended to use a laser positioning setup with additional reflectors placed on the detector PCB to know the positioning of the system in sub µm scales. The measurement can be done by pulling the detector behind the vacuum gate i.e. after the magnetic field coils in the DAQ section with the help of viewing ports without breaking the overall vacuum of the experiment. Due to technological advancements, these positioning systems can be bought off the shelf while not affecting the assembly costs of the experiment.

6.7 Aperture Related Systematics

As previously discussed, the aperture position in tandem with its dimensions affect the drift distance spectrum at the detector. While the aperture dimensions are already discussed in Sec. 6.3.1, here the focus will be on the tolerances for the positioning and dimensions of the aperture.

6.7.1 Uncertainty in Aperture Dimensions

As a first estimate, even though the active aperture will have a definite thickness, it was ignored as the majority of the edge effects from the aperture will arise from the other 2 dimensions. For the reduced aperture size recommended in this work, it was discovered that the drift distance spectrum at the detector was more influenced by the uncertainty in the drift dimension of the aperture x compared to the non-drift direction y. The obtained k-factors for the aperture dimensions were:

$$\begin{aligned} k_{x_{\text{AA,Prot.}}} &= 45.5 \quad k_{x_{\text{AA,Elec.}}} = 10.5 \\ k_{y_{\text{AA,Prot.}}} &= 3.4 \quad k_{y_{\text{AA,Elec.}}} = 0.76 \end{aligned} \tag{6.28}$$

To reduce the overall uncertainty within the experiment to an absolute and relative deviation of 10^{-3} level for the case of electrons and protons respectively, a precision of 10 µm in both x and y dimensions should be enough. However, considering the manufacturing tolerances that are easily achievable nowadays, it is recommended to aim for a precision of 1 µm for the case of the aperture dimension in the drift direction as it would reduce the uncertainty from a 10^{-4} level at a tolerance of 10 µm to 10^{-5} level.

6.7.2 Uncertainty in Aperture Positioning

The positioning of the aperture, much like the detector is not straightforward as its relative position to the central magnetic field line will need to be determined using the geometric reference points in the system and the magnetic field map of the experiment. Similar to the aperture dimensions, the drift distance spectrum was influenced more by the positioning offset in the drift direction relative to the non-drift direction. The k-factors for the positioning were:

$$\begin{aligned} k_{x_{\mathrm{AOffset,Prot.}}} &= 220.5 \quad k_{x_{\mathrm{AOffset,Elec.}}} = 62.2 \\ k_{y_{\mathrm{AOffset,Prot.}}} &= 7.2 \quad k_{y_{\mathrm{AOffset,Elec.}}} = 2.3 \end{aligned} \tag{6.29}$$

The increased uncertainty in the drift direction is expected as the drift distance spectrum is very sensitive to the positioning of the flanks, whereas in the non drift direction it is not as strong. Therefore, unlike the dimensions of the aperture, for the positioning it is recommended to have 1 µm precision in aperture position in the drift direction. It should be noted that this restriction can be loosened to the order of 10 µm by the use of an additional fit parameter as it should bring down the uncertainty at least by a factor of ≈ 10.

6.8 Non Detector Related Systematics

Due to the fact that the superconducting setup still needs to be optimized further, a full systematic uncertainties investigation was not conducted for the case of protons. However, in the following paragraphs some additional uncertainties that were investigated, that do not relate to the detection system of NoMoS, are discussed. The investigation of these systematic effects help highlight some additional factors that will have to be considered for using NoMoS to conduct electron-antineutrino correlation coefficient a measurements.

6.8.1 Work Function Differences

Work function differences can arise from the difference of material work functions of the different materials used within the experiment e.g. the aperture. These effects can introduce additional $\vec{E} \times \vec{B}$ effects or even effect the kinetic energy of the protons by either reducing or accelerating them depending upon the resulting potential seen by the protons relative to the decay point. While the same effect would be observed by the electrons, due to their high kinetic energy (three orders of magnitude higher than that of protons) the effect is negligible in this case.

In a first step, these effects were modelled within the transfer function by the introduction of a static potential difference that could alter the momentum of the protons. For a potential difference of 3 mV, the relative uncertainty introduced in $a\psi$ is:

$$\frac{\Delta a\psi}{a\psi} = 4 \times 10^{-4} \quad \text{or} \quad k_{\mathrm{WF}} = 0.14 \tag{6.30}$$

This means that to reduce these effects the work function differences should be known to a scale of 5 mV which will translate to a relative uncertainty of 7×10^{-4}. This task is extremely non-trivial but it can be possible using a good kelvin probe with the measurement being done preferably in vacuum to avoid effects from stray charges. It should be noted that in the actual experiment, these differences will have to be modelled by using COMSOL® [124], compared with literature values. Furthermore, experimental measurements during the assembly of the apparatus as well as after the beam time will have to be done using kelvin probes to minimize the uncertainty to a few mV. Some of these work function differences will have to be compensated for via the use of low-voltage (±2 V) with high precision («1 mV). It should be noted that the work function differences would be greater at the surface of the vessel, and will weaken towards the centre of the tube thus only affecting the low-energy protons. Therefore, additional systematic studies with the help of simulations, measurements, and calibration sources could be conducted to minimize the uncertainty. Additionally, systematic fits where the low-energy proton bins at the detector are removed can also be performed to understand the strength of the uncertainty if required.

6.8.2 Uncertainties in Magnetic Field Measurements

While the effects of the uncertainty in the magnetic field ratio at the aperture were already discussed in Sec. 6.3 and used to determine some recommendations for a deviation from the proposed superconducting setup for NoMoS, two other systematic uncertainties related to the magnetic field were also studied. These included the uncertainty in the magnetic field within the detection region, and the uncertainty in the measurement of the absolute magnetic field within the $R\psi \times B\psi$ region of the experiment for the case of protons. The motivation for the magnetic field ratio at the detector r_{D} was due to its close proximity to the detection system. Whereas, the motivation for the uncertainty in the absolute magnetic field within the $R\psi \times B\psi$ region $B_{R\times B}$ was due to its contribution to the overall uncertainty for the normal and superconducting setup for the case of electrons as already discussed in the thesis of D. Moser [27].

The scaling factor for the uncertainty in $B_{R\times B}$ for protons in the superconducting case was found to be:

$$k_{B_{R\times B}} = 73 \tag{6.31}$$

For the proposed relative uncertainty of 0.160 of $B_{R\times B}$ in Ref. [27], this corresponds to a relative uncertainty of 11×10^{-3} in the parameter $a\psi$ for the case of protons. To reduce this, either an additional fit parameter for the absolute magnetic field needs to be utilized or the uncertainty in the monitoring of the magnetic field needs to be reduced by a factor of 10 by measurement. It is recommended to take a combination of both approaches. A relative precision higher than 0.16 can be achieved by a combination of Hall probes, to be used for mapping the magnetic field and static NMR probes for the measurement of absolute magnetic field with accuracy of a few nT. Additionally, a fit parameter can then later be utilized to reduce the uncertainty in this magnetic field map further by an additional factor of 10.

Similarly the k-factor for the relative uncertainty introduced on the proton spectrum by r_D is:

$$k_{r_\mathrm{D}} = 2.2,\psi \tag{6.32}$$

meaning that the magnetic field ratio at the detector needs to be known with a relative uncertainty of 10^{-4}. This further supports the need for conducting precision magnetic field mapping of the NoMoS apparatus using a combination of Hall and NMR probes.

6.9 Summary of Systematic Uncertainties

Tables 6.4 and 6.5 show the summary of the uncertainties introduced on the observables, a and b, by the investigated systematic effects in a superconducting NoMoS setup. Taking the scaling factors into account, values for the precision required to achieve the desired accuracy level of 10^{-3}, either absolute or relative, in the observables was recommended. It should be noted that the stated values are not final and were calculated for a non-optimized setup and in theory should go down for a more optimized version of NoMoS. Furthermore, it should also be noted that introduction of additional fit parameters for particular systematic effects will also help reduce the overall uncertainty. However, increasing the number of additional fit parameters will also increase the overall measurement time required for the experiment, by a factor of four for each additional fit parameter. Therefore, a sweet spot should be found where the additional fit parameters will reduce the overall systematic error budget to a desired amount within a reasonable measurement time. An additional possibility for the usage of additional fit parameters, without increasing the overall beam time, is minimizing the uncertainties by conducting individual systematic investigations using appropriate calibration techniques, e.g. work function influences on protons could be studied further by the usage of a positron source.

It should be noted that Tables 6.4 and 6.5 only show some of the investigations performed within the course of this thesis. Other detector related recommendations include:

- Using detectors with at least a resolution of 0.33 mm in the drift direction for the superconducting version of NoMoS, which corresponds to 64 bins.

- Ensuring that the bins of the detector where the rising and falling flanks of the spectrum fall are always operational (see Sec. 6.4.2)

Using these recommendations, the ultimate accuracy goal of the experiment should be reachable if the uncertainties are added quadratically.

Table 6.4: Recommended precision required for proton-related uncertainties in various systematic effects of the experiment. The recommendations are tailored to achieve a final relative deviation in $a\psi$ in the 10^{-3} level by using a detector with 64 bins in the drift direction if the uncertainties are summed quadratically.
[1]: The original scaling factor is then reduced by the use of a fit parameter.
[2]: By using an additional fit parameter, the required precision can be increased.
[3]: Relative Uncertainty, dependent on the optimized magnetic field ratio.
[4]: The uncertainty of the systematic effect will decrease with the simulation of additional particles. Estimated time for simulation of one angle-energy combination is roughly 17 days without parallelization.

Systematic Effect	**Parameter**	**Scaling Factor (k)**	**Precision Req.**
Detector Misalignment	$s_{\text{mov.,x}}$	8.7×10^{3}[1]	10 µm
	$s_{\text{mov.,y}}$	530[2]	1 µm
	s_{Rotation}	9.9×10^{-3}	0.1°
Aperture Dimensions	x_{AA}	45.5	1 µm
	y_{AA}	3.4	10 µm
	x_{AOffset}	220.5	1 µm
	y_{AOffset}	7.2	10 µm
Work Function	Φ_{WF}	0.14	1 mV
Magnetic Field in $R\psi\times B\psi$ region	$B_{R\times B}$	73	10 µT
Magnetic Field Ratio at Detector	r_{D}	2.2	0.16[3]
Systematic Effect	**Parameter**	**Uncertainty $\Delta a/a\psi$**	**Recommendation**
Backscattering	η_{BS}	9.5×10^{-4}	5×10^{7}Particles[4]
Detector Efficiency	$\epsilon\psi$	6.2×10^{-4}	5×10^{7}Particles[4]

Table 6.5: Recommended precision required for electron-related uncertainties in various systematic effects of the experiment. The recommendations are tailored to achieve a final absolute deviation in $b\psi$ at the 10^{-3} level by using a detector with 64 bins in the drift direction.
[1]: The original scaling factor is then reduced by the use of a fit parameter.
[2]: By using an additional fit parameter, the required precision can be increased.
[3]: The uncertainty on the observable will go down by the simulation of additional particles.
[4]: The uncertainty will go down further when the detector's energy resolution is improved.

Systematic Effect	**Parameter**	**Scaling Factor (k)**	**Precision Req.**
Detector Misalignment	$s_{\mathrm{mov.,x}}$	2.6×10^3[1]	10 µm
	$s_{\mathrm{mov.,y}}$	137[2]	1 µm
	s_{Rotation}	9.5×10^{-4}	0.1°
Aperture Dimensions	x_{AA}	10.5	1 µm
	y_{AA}	0.76	10 µm
	x_{AOffset}	62.2	1 µm
	y_{AOffset}	2.3	10 µm
Systematic Effect	**Parameter**	**Uncertainty $\Delta b\psi$**	**Recommendation**
Backscattering	η_{BS}	2.1×10^{-4}	1×10^6 Particles[3]
BS from Aperture	$\eta_{\mathrm{BS,Apt}}$	1.7×10^{-4}	10 keV Resolution[4]
BS from Back Detector	$\eta_{\mathrm{BS,Back}}$	4.3×10^{-4}	Placed 40 cm away from DV

6.10 Proposals for Systematic Effect Investigations by Additional Measurements

Apart from getting a handle on the uncertainties from various systematic effects within the experiment e.g. by precise measurement of the magnetic field profile within the experiment and detector placement, the effect of certain systematic effects can be further understood and as a consequence reduced by conducting additional characterization measurements.

6.10.1 Independent Calibration of Detector Efficiency

Some stringent constraints on the values for detector efficiency could be introduced by the measurement of the detector response with the desired DAQ system with a calibrated particle source. For the case of protons, this can be done in VERA (Vienna Environmental Research Accelerator), where a beam of negative H ions can be shot on the detector to study its response at different energies (in the keV range) and angles. The electrons in the negative H ions would be stripped away in the first few nm of the detector and a response similar to that of a proton will be produced in the detector. Taking multiple measurements can also help provide an independent and alternative measurement of the thickness of the passivation layer as the response of the detector will change with a varying polar angle. Additionally, the detector efficiency can also be understood further by studying the waveforms of impinging particles by conducting in depth TCAD simulations. Lastly, the detector efficiency can also be studied by conducting measurements by varying the kinetic energy of the protons e.g. by change of post-acceleration.

6.10.2 Calibration of Detector Alignment

One approach for reducing misalignment effects within the experiment is to conduct measurements with the detector within the experiment with the help of a well calibrated electron and positron source. One candidate for this purpose could be the aSPECTINO source [125] with appropriate modifications. Coupling the response on the detector with the information of the magnetic field profile, a MC simulation can be performed to see which bins on the detector should see a signal.

6.10.3 Changing Aperture Size

As discussed in Sec. 6.3.1, there are in theory two aperture sizes that can be chosen. If a modular aperture design is used where the opening of the aperture can be changed, aperture-related systematic uncertainties can be investigated by conducting multiple measurements with varying aperture sizes.

6.10.4 Variation of Post-Acceleration

Even though the electrode design is not finalized, which is why the effects arising from $\vec{E} \times \vec{B}$ drifts are not discussed within the course of this work, the variation of the post-acceleration of the electrode can help provide valuable information on the $\vec{E} \times \vec{B}$ effects. It can also help provide an independent check of the detector efficiency models as the efficiency of the detector for the case of protons will change if a post-acceleration voltage of $-15\,\mathrm{kV}$ or $-5\,\mathrm{kV}$ is used.

6.10.5 Variation of Filter Magnetic Field

By varying the magnetic field ratio at the filter, the maximum polar angle θ of a charged particle that overcomes the magnetic filter within the experiment can be lowered or increased. This allows an independent test on certain systematic effects such as the backscattering corrections arising from backscattered electrons reflected from the filter and hitting the drift detector again, and the correction of contributions of backscattered electrons from the back detector at the main drift detector. For the case of the superconducting setup of NoMoS, lowering the magnetic field will allow for an increase in the number of backscattered electrons from the back detector whereas allowing more backscattered electrons from the drift detector to pass through the filter coils, thus reducing their contribution. Coupling this information with Monte Carlo studies will help reduce the associated systematic uncertainties for the experiment.

Chapter 7

Summary and Outlook

The NoMoS experiment aims to do precision measurements of the charged decay products from free neutron beta decay by utilizing the so-called $R \times B$ drift effect, that will disperse the particles in relation to their momentum. A motivation for the experiment is to measure the electron-antineutrino correlation coefficient a, and the Fierz interference term b from the measurement of the proton and electron spectrum respectively. A measurement of a in conjunction with the neutron lifetime will help provide an independent value of V_{ud} to test the unitarity of the CKM matrix, whereas the measurement of b will help probe physics beyond the Standard Model (SM) by looking for left handed scalar and tensor couplings within the decay as explained in detail in Sec. 2.2.

The main goal of this doctoral work was to provide recommendations for the detection technology to be used within the experiment, as well as to investigate various systematic effects that may arise from the detection system and their associated uncertainties. The supplementary detection system i.e. the backscattering detector, back detector, and the active aperture, have been discussed in Chapter 3 and recommendations regarding the detection technology, and their consequent placement are provided.

Due to the small kinetic energy of the protons ($\approx 750\,\text{eV}$) from the decay, along with the stringent requirements of the experiment i.e. a detector with a high spatial resolution in the order of <1 mm covering an area of $4\,\text{cm} \times 5\,\text{cm}$, with a SNR of at least 5, and low backscattering rate (see Sec. 4.1), a novel silicon detector called the Proton Low Gain Avalanche Detector (pLGAD) was designed, patented, and first prototypes manufactured for low-penetrating particles. The technology offers a homogenous linear gain to the signal of particles with $< 1\,\mu\text{m}$ penetration range in silicon with a high detection efficiency at room temperature. A proof of principle of the detection technology is provided in Sec. 4.3.1 with the help of TCT measurements, which showed that the average gain of the diodes was ≈ 15 for a near-UV laser (404 nm) in comparison to ≈ 1.2 for an infrared laser (1064 nm). Furthermore the expected performance of the sensor coupled with different Data Acquisition (DAQ) systems was investigated as can be seen in Sec. 4.4.2.

A previously overlooked detector-related systematic effect called Channeling was discussed in Chapter 5. A detailed study of the influence of channeling on the impinging ion's energy and angle further highlighted the importance of the systematic effect. It was found that ignoring the effect will cause an overestimation of the backscattering rate of the protons, which will consequently cause an underestimation of the detector efficiency. Due to the strength of this effect, a preliminary discussion of how inclusion of this systematic effect can influence the neutron lifetime for beam experiments is also provided in Sec. 5.1.5 and the need for further investigation is highlighted. Furthermore, the detection efficiency of the pLGAD sensor was simulated under various scenarios within NoMoS, and was found to be $99.99\% \pm 0.02\%$ for 15 keV protons.

My investigations also revealed that the superconducting setup of NoMoS needs further optimization, which is outside the scope of this work. Additional changes apart from the optimization of the magnetic field ratios of the superconducting version of NoMoS were suggested and can be found in Sec. 6.3.3. Using the proposed changes, and the analytical mathematical description of the NoMoS apparatus called the transfer function, a thorough investigation of detector related systematic effects and their associated uncertainties was also performed. The recommendations for achieving the desired precision for the electron antineutrino correlation coefficient a and the Fierz interference term b in the experiment are summarized in Sec. 6.9. It should be noted that for the reduction of some systematic uncertainties, an additional fit parameter is suggested. The efficacy of the fit parameter using the transfer function was also demonstrated for the first time within this work and can be seen in Sec. 6.6.1.

From the studies conducted, it can be concluded that the final accuracy goal of NoMoS of 10^{-3} absolute uncertainty in b and 3×10^{-3} relative uncertainty in a can be achieved from uncertainties introduced by the detection side of the experiment. However, in order to do so, further optimization of the magnetic field ratios of the system as well as high accuracy in manufacturing tolerances for the aperture dimensions and detector placement, or usage of additional fit parameters specifically for detector misalignment effects, alongside with computationally intensive simulations for corrections will be required.

7.1 Next Steps for NoMoS

Even though we have shown that the accuracy goals of NoMoS is reachable, the design of the experiment is far from finalized. In the next step, additional systematic effects should be integrated within the transfer function and studied in detail. My personal list of proposals for the next steps for the finalization of the calculation of the systematic error budget for NoMoS is as follows:

- Optimization of the magnetic field ratios and consequently the magnetic field coils of the superconducting version of NoMoS, cf. Sec. 6.3. Subsequently, determination of the systematic error budget with the improved magnetic field setup.

- Final design and characterization of an electrode for the post-acceleration of protons, cf. [58] and Sec. 6.3.

- Integration and study of the following systematic effects:
  - $\vec{E} \times \vec{B}$ effect
  - Tilt of the detector in the x-z or y-z plane, where z is the axis in which the beam propagates
  - Inclusion of edge effects from the aperture thickness
  - Stern-Gerlach effect
  - Doppler shifts of the charged decay particles when NoMoS is not used in its stand alone configuration
  - Electron scattering from the post-acceleration electrode
  - Effects of rest gas
  - Additional magnetic field related systematics, for example, the angular B field gradient in the $\vec{R} \times \vec{B}$ region, Earth's magnetic field, additional magnetic field inhomogeneities. For a comprehensive list I refer to the work of D. Moser [27].

- Study of lateral drift effects of generated e-h-pairs in the pLGAD concept due to the applied magnetic field.

- Manufacturing of pLGAD sensors with a thin entrance window, cf. Sec. 5.2. Additionally the final version of the detector should be tested and characterized with a proton beam such as the one provided at Vienna Environmental Research Accelerator (VERA) cf. Sec. 6.10.

Studies for some of the aforementioned systematics were already conducted using a simplistic Transfer function [27], but for the sake of completeness, these systematics should be introduced in the final version of the transfer function to study any potential correlations between additional fit parameters.

Even though currently there are no concrete plans to construct the experiment, I hope that this work helps curb any doubts about the efficacy of the experiment. Nonetheless, I have extensively discussed detection-related systematic effects of the experiment and shown the precision required to reach the initial desired accuracy of

$\Delta a/a \leq 1\%$ and $\Delta b \leq 6 \times 10^{-3}$ for the measurement of the electron antineutrino correlation parameter a and the Fierz interference term b respectively from the detection side of the experiment. This can then further be reduced to the final accuracy of NoMoS of 10^{-3} for b and 3×10^{-3} for a by performing further Monte Carlo simulations for corrections. It should be noted that these recommendations will get further relaxed with the optimization of the magnetic field ratios of the experiment, and only improve the overall systematic error budget.

Appendices

Appendix A

External Quantum Efficiency Measurement of pLGAD

In order to further study the pLGAD diodes, one chosen diode was used in an Equivalent Quantum Efficiency measurement, where its response was studied when subjected to a laser of varying wavelength from 400 nm to 1100 nm. The measurement was conducted by Miquel Casademont, a Ph.D. candidate at The Nanostructured Materials for Optoelectronics for Energy Harvesting (NANOPTO), a research group at Insitute of Materials Science of Barcelona (University Autónoma de Barcelona).

Figure A.1 shows the gain of the chosen diode obtained by comparison of the deposited charge when subject to the laser of varying wavelengths. The gain of the diode gets smaller as the laser penetrates further into the detector, which is as expected. However, the oscillating behaviour of the gain could not be explained. It may be the consequence of some optical effect introduced by the interaction of the laser with the passivation layer on top of the diode, but further TCAD simulations, which are outside the scope of this work, are required to understand this effect better.

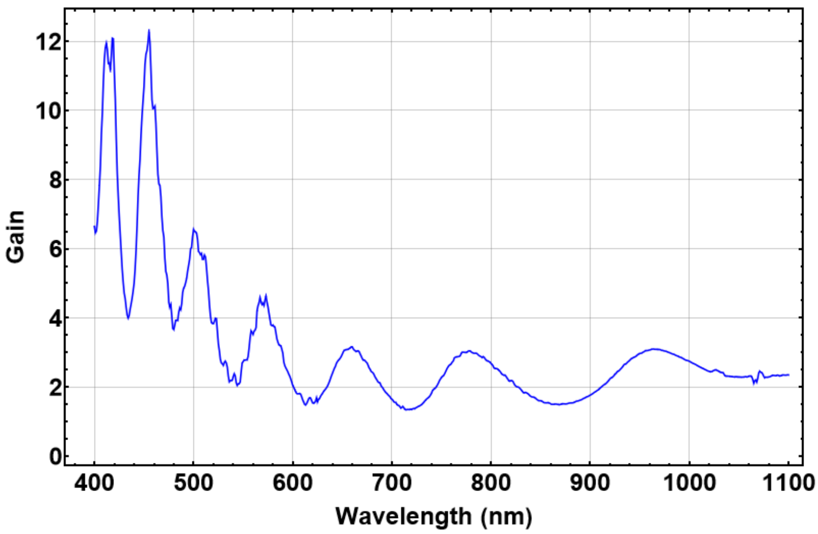

Figure A.1: The gain of the pLGAD when subjected to a laser with varying wavelengths. For details see text.

Appendix B

IMSIL Configuration

The following is an exemplary file used in the IMSIL simulations for a detector with a 1 nm thick Al_2O_3 passivation layer in front of the active silicon. The entries preceded and followed by # are replaced by a bash script on run time with the relevant quantity.

```
Detector Studies - H on Al2O3-Si (1nm window) with varying energies
Energy of the incoming H ion #energy# keV with tilt = #tilt#

&setup    natom=4 nr=2 /
&ions     name='H' energy=#energy# tilt=#tilt# ranrot=true
nion=500000 /
&material region=1 name='Al2O3' xtal='no' /
&material region=2 name='Si' xtal='yes' wafer=1,0,0 vsurf=0,0,1 /
&snpar    ef=10 lstffp=t ffpmax=1000 pmaxmin=2.7 /

&separ    atom1=1 atom2=2 corlin=1.39 /
&separ    atom1=1 atom2=3 corlin=0.593 /
&separ    atom1=1 atom2=4 corlin=1.68 powint=0.81 c0bethe=1.7 c1bethe=3.785
xnl='0.35,0.2' facscr=1.37 /
&separ    straggle='on' estrag=10000 /
&damage   ldam=t lrcoil=f /
&geometry posif='0,10,10000' /
&output   lhisee=t lhise=t lhisb=t lmom=t lhis=t wboxi=30 nbox=1000 /
```

The first 2 lines of the files are comments and can be ignored. The actual file starts from &setup, where the number of atoms and regions of the material are defined. It is then followed by the information regarding the impinging ions, and the two different regions. The first is the amorphous Al_2O_3 region (notice the xtal='no'), followed by the crystalline Si. The next lines are the nuclear and electronic energy loss corrections as discussed in text. The nuclear energy loss corrections are denoted by &snpar whereas the electronic energy loss corrections are preceded by &separ. The damage section describes the damage caused by the ions to the crystal lattice and, the geometry line provides the software with the thicknesses of the 2 regions in Ångstorms. Lastly, the output section is for writing different histograms to file. All of these quantities are explained in detail in the IMSIL manual. The correction value for Lindhardt model and their reasoning is explained in Sec. 5.1.1.

Appendix C

Fitted Electron Backscattering Coefficients

Table C.1 shows the energy-dependent fit parameters for the electron backscattering function according to Eq. 6.19. More values for lower energies $<\psi 61$ keV are selected as electrons in that energy range are more probabilistic in the decay, so that more values within that regime will improve the accuracy of the interpolation.

Table C.1: Energy-Dependent Fit Parameters for the electron backscattering function (see Eq. 6.19)

Energy (keV)	c_1	c_2
0.5	0.201	6.034×10^{-7}
1	0.193	8.156×10^{-7}
5	0.155	1.266×10^{-6}
11	0.148	1.302×10^{-6}
21	0.144	1.338×10^{-6}
31	0.138	1.328×10^{-6}
41	0.110	1.255×10^{-6}
61	0.099	1.203×10^{-6}
121	0.087	1.130×10^{-6}
181	0.080	1.064×10^{-6}
241	0.075	1.042×10^{-6}
301	0.071	9.933×10^{-7}
361	0.072	9.083×10^{-7}
421	0.064	9.826×10^{-7}
481	0.058	9.658×10^{-7}
541	0.049	9.441×10^{-7}
601	0.041	8.991×10^{-7}
661	0.034	8.147×10^{-7}
721	0.028	7.257×10^{-7}

Bibliography

[1] R. L. Workman, et al., Review of Particle Physics, PTEP 2022 (2022) 083C01. doi:10.1093/ptep/ptac097.

[2] J. D. Jackson, S. B. Treiman, H. W. Wyld, Coulomb corrections in allowed beta transitions, Nucl. Phys. 4 (1957) 206.

[3] J. D. Jackson, S. B. Treiman, H. W. Wyld, Possible tests of time reversal invariance in beta decay, Phys. Rep. 106 (1957) 517.

[4] J. C. Hardy, I. S. Towner, Superallowed $0^+ \to 0^+$ nuclear β decays: 2020 critical survey, with implications for V_{ud} and ckm unitarity, Phys. Rev. C 102 (2020) 045501. doi:10.1103/PhysRevC.102.045501.
URL `https://link.aps.org/doi/10.1103/PhysRevC.102.045501`

[5] A. Czarnecki, W. J. Marciano, A. Sirlin, Radiative corrections to neutron and nuclear beta decays revisited, Phys. Rev. D 100 (2019) 073008. doi:10.1103/PhysRevD.100.073008.
URL `https://link.aps.org/doi/10.1103/PhysRevD.100.073008`

[6] K. Shiells, P. G. Blunden, W. Melnitchouk, Electroweak axial structure functions and improved extraction of the V_{ud} ckm matrix element, Phys. Rev. D 104 (2021) 033003. doi:10.1103/PhysRevD.104.033003.
URL `https://link.aps.org/doi/10.1103/PhysRevD.104.033003`

[7] L. Hayen, Standard model $\mathcal{O}(\ )$ renormalization of g_A and its impact on new physics searches, Phys. Rev. D 103 (2021) 113001. doi:10.1103/PhysRevD.103.113001.
URL `https://link.aps.org/doi/10.1103/PhysRevD.103.113001`

[8] C.-Y. Seng, X. Feng, M. Gorchtein, L.-C. Jin, Joint lattice qcd–dispersion theory analysis confirms the quark-mixing top-row unitarity deficit, Phys. Rev. D 101 (2020) 111301. doi:10.1103/PhysRevD.101.111301.
URL `https://link.aps.org/doi/10.1103/PhysRevD.101.111301`

[9] A. Czarnecki, W. J. Marciano, A. Sirlin, Precision measurements and ckm unitarity, Phys. Rev. D 70 (2004) 093006. doi:10.1103/PhysRevD.70.093006.
URL `https://link.aps.org/doi/10.1103/PhysRevD.70.093006`

[10] M. Beck, F. Ayala Guardia, M. Borg, J. Kahlenberg, R. Muñoz Horta, C. Schmidt, A. Wunderle, W. Heil, R. Maisonobe, M. Simson, T. Soldner, R. Virot, O. Zimmer, M. Klopf, G. Konrad, S. Baeßler, F. Glück, U. Schmidt, Improved determination of the $\beta-\overline{\nu}_e$ angular correlation coefficient a in free neutron decay with the aSPECT spectrometer, Phys. Rev. C 101 (2020) 055506. doi:10.1103/PhysRevC.101.055506.

[11] M. T. Hassan, W. A. Byron, G. Darius, C. DeAngelis, F. E. Wietfeldt, B. Collett, G. L. Jones, A. Komives, G. Noid, E. J. Stephenson, F. Bateman, M. S. Dewey, T. R. Gentile, M. P. Mendenhall, J. S. Nico, Measurement of the neutron decay electron-antineutrino angular correlation by the acorn experiment, Phys. Rev. C 103 (2021) 045502. doi:10.1103/PhysRevC.103.045502.
URL `https://link.aps.org/doi/10.1103/PhysRevC.103.045502`

[12] J. Fry, R. Alarcon, S. Baeßler, S. Balascuta, L. B. Palos, T. Bailey, K. Bass, N. Birge, A. Blose, D. Borissenko, J. Bowman, L. Broussard, A. Bryant, J. Byrne, J. Calarco, J. Caylor, K. Chang, T. Chupp, T. Cianciolo, C. Crawford, X. Ding, M. Doyle, W. Fan, W. Farrar, N. Fomin, E. Frlež, M. Gericke, M. Gervais, F. Glück, G. Greene, R. Grzywacz, V. Gudkov, J. Hamblen, C. Hayes, C. Hendrus, T. Ito, A. Jezghani, H. Li, M. Makela, N. Macsai, J. Mammei, R. Mammei, M. Martinez, D. Matthews, M. McCrea, P. McGaughey, C. McLaughlin, P. Mueller, D. van Petten, S. Penttilä, D. Perryman, R. Picker, J. Pierce, D. Počanić, Y. Qian, J. Ramsey, G. Randall, G. Riley, K. Rykaczewski, A. Salas-Bacci, S. Samiei, E. Scott, T. Shelton, S. Sjue, A. Smith, E. Smith, E. Stevens, J. Wexler, R. Whitehead, W. Wilburn, A. Young, B. Zeck, The nab experiment: A precision measurement of unpolarized neutron beta decay, EPJ Web of Conferences 219 (2019) 04002. doi:10.1051/epjconf/201921904002.
URL `https://doi.org/10.1051/epjconf/201921904002`

[13] M. González-Alonso, O. Naviliat-Cuncic, Kinematic sensitivity to the fierz term of β-decay differential spectra, Phys. Rev. C 94 (2016) 035503. doi:10.1103/PhysRevC.94.035503.
URL `https://link.aps.org/doi/10.1103/PhysRevC.94.035503`

[14] X. Sun, E. Adamek, B. Allgeier, Y. Bagdasarova, D. B. Berguno, M. Blatnik, T. J. Bowles, L. J. Broussard, M. A.-P. Brown, R. Carr, S. Clayton, C. Cude-Woods, S. Currie, E. B. Dees, X. Ding, B. W. Filippone, A. García, P. Geltenbort, S. Hasan, K. P. Hickerson, J. Hoagland, R. Hong, A. T. Holley, T. M.

Ito, A. Knecht, C.-Y. Liu, J. Liu, M. Makela, R. Mammei, J. W. Martin, D. Melconian, M. P. Mendenhall, S. D. Moore, C. L. Morris, S. Nepal, N. Nouri, R. W. Pattie, A. Pérez Gálvan, D. G. Phillips, R. Picker, M. L. Pitt, B. Plaster, D. J. Salvat, A. Saunders, E. I. Sharapov, S. Sjue, S. Slutsky, W. Sondheim, C. Swank, E. Tatar, R. B. Vogelaar, B. VornDick, Z. Wang, W. Wei, J. W. Wexler, T. Womack, C. Wrede, A. R. Young, B. A. Zeck, Improved limits on fierz interference using asymmetry measurements from the ultracold neutron asymmetry (ucna) experiment, Phys. Rev. C 101 (2020) 035503. doi:10.1103/PhysRevC.101.035503. URL https://link.aps.org/doi/10.1103/PhysRevC.101.035503

[15] H. Saul, et al., to be published (2019).

[16] D. Počanić, et al., Nab: Measurement principles, apparatus and uncertainties, Nucl. Instr. Meth. Phys. Res. A 611 (2) (2009) 211–215. doi:10.1016/j.nima.2009.07.065.

[17] W. Wilburn, J. Bowman, G. Mitchell, J. O'Donnell, S. Penttila, P. Seo, J. Calarco, F. Hersmann, T. Chupp, T. Cianciolo, K. Rykaczewski, G. Young, R. D. Souza, W. Snow, D. Desai, G. Greene, R. Grzywacz, E. Frlez, D. Pocanic, T. Gentile, V. Gudkov, G. Jones, Measurement of neutron decay parameters - the abBA experiment, Journal of Research of the National Institute of Standards and Technology 110 (4) (2005) 389. doi:10.6028/jres.110.058.
URL https://doi.org/10.6028/jres.110.058

[18] G. Konrad, et al., Neutron decay with PERC: a progress report, J. Phys.: Conf. Ser. 340 (1) (2012) 012048.
URL http://stacks.iop.org/1742-6596/340/i=1/a=012048

[19] X. Wang, G. Konrad, H. Abele, $\vec{R} \times \vec{B}$ momentum spectrometer with high resolution and large phase space acceptance, Nucl. Instr. Meth. A 701 (2013) 254–261. doi:https://doi.org/10.1016/j.nima.2012.10.071.
URL http://www.sciencedirect.com/science/article/pii/S0168900212012211

[20] G. Pelligrini, S. Hidalgo, D. Flores, W. Khalid, M. Valentan, Low-penetrating particles low-gain avalanche detector., Patent (Pending), EP20382836.

[21] F. Halzen, A. D. Martin, Quarks and Leptons: An Introductory Course in Modern Particle Physics, Wiley, 1991.

[22] W. N. Cottingham, D. A. Greenwood, An Introduction to the Standard Model of Particle Physics, Cambridge University Press, 2007.

[23] M. Gonzalez-Alonso, O. Naviliat-Cuncic, N. Severijns, New physics searches in nuclear and neutron β decay, Progress in Particle and Nuclear Physics 104 (2019) 165–223. doi:https://doi.org/10.1016/j.ppnp.2018.08.002.
URL `https://www.sciencedirect.com/science/article/pii/S0146641018300735`

[24] D. Dubbers, B. Märkisch, Precise measurements of the decay of free neutrons, Annual Review of Nuclear and Particle Science 71 (1) (2021) 139–163. arXiv:https://doi.org/10.1146/annurev-nucl-102419-043156, doi:10.1146/annurev-nucl-102419-043156.
URL `https://doi.org/10.1146/annurev-nucl-102419-043156`

[25] R. P. Feynman, M. Gell-Mann, Theory of the fermi interaction, Phys. Rev. 109 (1958) 193–198. doi:10.1103/PhysRev.109.193.
URL `https://link.aps.org/doi/10.1103/PhysRev.109.193`

[26] G. E. Konrad, Measurement of the proton recoil spectrum in neutron beta decay with the spectrometer aspect : study of systematic effects, Ph.D. thesis (2012). doi:10.25358/OPENSCIENCE-1316.
URL `https://openscience.ub.uni-mainz.de/handle/20.500.12030/1318`

[27] D. Moser, Systematic investigation of an RxB spectrometer's magnet system, Ph.D. thesis (2021). doi:10.34726/HSS.2021.38984.
URL `https://repositum.tuwien.at/handle/20.500.12708/17014`

[28] F. Glück, et al., Measurable parameters of neutron decay, Nucl. Phys. A 593 (1995) 125.

[29] T. D. Lee, C. N. Yang, Question of parity conservation in weak interactions, Phys. Rev. 104 (1956) 254–258. doi:10.1103/PhysRev.104.254.
URL `https://link.aps.org/doi/10.1103/PhysRev.104.254`

[30] O. Nachtmann, Relativistic corrections to the recoil spectrum in neutron β-decay, Zeitschrift für Physik A Hadrons and nuclei 215 (5) (1968) 505–514. doi:10.1007/bf01379762.
URL `https://doi.org/10.1007/bf01379762`

[31] F. Glück, Measurable distributions of unpolarized neutron decay, Phys. Rev. D 47 (1993) 2840–2848. doi:10.1103/PhysRevD.47.2840.
URL `https://link.aps.org/doi/10.1103/PhysRevD.47.2840`

[32] F. Glück, Radiative corrections to neutron and nuclear β-decays: a serious kinematics problem in the literature (2022). arXiv:2205.05042.

[33] A. Falkowski, M. González-Alonso, O. Naviliat-Cuncic, Comprehensive analysis of beta decays within and beyond the standard model, Journal of High Energy Physics 2021 (4) (Apr. 2021). doi:10.1007/jhep04(2021)126.
URL `https://doi.org/10.1007/jhep04(2021)126`

[34] P. Herczeg, Beta decay beyond the standard model, Prog. Part. Nucl. Phys. 46 (2) (2001) 413–457. doi:https://doi.org/10.1016/S0146-6410(01)00149-1.
URL `http://www.sciencedirect.com/science/article/pii/S0146641001001491`

[35] D. Wilkinson, Analysis of neutron β-decay, Nuclear Physics A 377 (2) (1982) 474–504. doi:https://doi.org/10.1016/0375-9474(82)90051-3.
URL `https://www.sciencedirect.com/science/article/pii/0375947482900513`

[36] A. Sirlin, General properties of the electromagnetic corrections to the beta decay of a physical nucleon, Phys. Rev. 164 (1967) 1767–1775. doi:10.1103/PhysRev.164.1767.
URL `https://link.aps.org/doi/10.1103/PhysRev.164.1767`

[37] *a*SPECT Collaboration, U. Schmidt, Reanalysis of the of β-ν_e^- angular correlation measurement aspect with new constraints on fierz interference, pSI 2022 (2022).
URL `https://indico.psi.ch/event/11742/contributions/38675/`

[38] D. Dubbers, M. G. Schmidt, The neutron and its role in cosmology and particle physics, Rev. Mod. Phys. 83 (2011) 1111–1171. doi:10.1103/RevModPhys.83.1111.
URL `https://link.aps.org/doi/10.1103/RevModPhys.83.1111`

[39] A. Serebrov, V. Varlamov, A. Kharitonov, A. Fomin, Y. Pokotilovski, P. Geltenbort, J. Butterworth, I. Krasnoschekova, M. Lasakov, R. Tal'daev, A. Vassiljev, O. Zherebtsov, Measurement of the neutron lifetime using a gravitational trap and a low-temperature fomblin coating, Journal of Research of the National Institute of Standards and Technology 110 (4) (2005) 333. doi:10.6028/jres.110.049.
URL `https://doi.org/10.6028/jres.110.049`

[40] F. M. Gonzalez, E. M. Fries, C. Cude-Woods, T. Bailey, M. Blatnik, L. J. Broussard, N. B. Callahan, J. H. Choi, S. M. Clayton, S. A. Currie, M. Dawid, E. B. Dees, B. W. Filippone, W. Fox, P. Geltenbort, E. George, L. Hayen, K. P. Hickerson, M. A. Hoffbauer, K. Hoffman, A. T. Holley, T. M. Ito, A. Komives, C.-Y. Liu, M. Makela, C. L. Morris, R. Musedinovic, C. O'Shaughnessy, R. W. Pattie,

J. Ramsey, D. J. Salvat, A. Saunders, E. I. Sharapov, S. Slutsky, V. Su, X. Sun, C. Swank, Z. Tang, W. Uhrich, J. Vanderwerp, P. Walstrom, Z. Wang, W. Wei, A. R. Young, Improved neutron lifetime measurement with UCNτ, Phys. Rev. Lett. 127 (2021) 162501. doi:10.1103/PhysRevLett.127.162501.
URL `https://link.aps.org/doi/10.1103/PhysRevLett.127.162501`

[41] N. Sumi, K. Hirota, G. Ichikawa, T. Ino, Y. Iwashita, S. Kajiwara, Y. Kato, M. Kitaguchi, K. Mishima, K. Morikawa, T. Mogi, H. Oide, H. Okabe, H. Otono, T. Shima, H. M. Shimizu, Y. Sugisawa, T. Tanabe, S. Yamashita, K. Yano, T. Yoshioka, Precise neutron lifetime measurement using pulsed neutron beams at j-PARC, in: Proceedings of the 3rd J-PARC Symposium (J-PARC2019), Journal of the Physical Society of Japan, 2021. doi:10.7566/jpscp.33.011056.
URL `https://doi.org/10.7566/jpscp.33.011056`

[42] J. S. Nico, M. S. Dewey, D. M. Gilliam, F. E. Wietfeldt, X. Fei, W. M. Snow, G. L. Greene, J. Pauwels, R. Eykens, A. Lamberty, J. V. Gestel, R. D. Scott, Measurement of the neutron lifetime by counting trapped protons in a cold neutron beam, Phys. Rev. C 71 (2005) 055502. doi:10.1103/PhysRevC.71.055502.
URL `https://link.aps.org/doi/10.1103/PhysRevC.71.055502`

[43] M. Klopf, E. Jericha, B. Märkisch, H. Saul, T. Soldner, H. Abele, Constraints on the dark matter interpretation $n \rightarrow \chi + e^+e^-$ of the neutron decay anomaly with the perkeo ii experiment, Phys. Rev. Lett. 122 (2019) 222503. doi:10.1103/PhysRevLett.122.222503.
URL `https://link.aps.org/doi/10.1103/PhysRevLett.122.222503`

[44] A. P. Serebrov, Disagreement between measurements of the neutron lifetime by the ultracold neutron storage method and the beam technique, Physics-Uspekhi 62 (6) (2019) 596. doi:10.3367/UFNe.2018.11.038475.
URL `https://dx.doi.org/10.3367/UFNe.2018.11.038475`

[45] L. J. Broussard, J. L. Barrow, L. DeBeer-Schmitt, T. Dennis, M. R. Fitzsimmons, M. J. Frost, C. E. Gilbert, F. M. Gonzalez, L. Heilbronn, E. B. Iverson, A. Johnston, Y. Kamyshkov, M. Kline, P. Lewiz, C. Matteson, J. Ternullo, L. Varriano, S. Vavra, Experimental search for neutron to mirror neutron oscillations as an explanation of the neutron lifetime anomaly, Phys. Rev. Lett. 128 (2022) 212503. doi:10.1103/PhysRevLett.128.212503.
URL `https://link.aps.org/doi/10.1103/PhysRevLett.128.212503`

[46] D. Dubbers, H. Saul, B. Märkisch, T. Soldner, H. Abele, Exotic decay channels are not the cause of the neutron lifetime anomaly, Physics Letters B 791 (2019) 6–10. doi:https://doi.org/10.1016/j.physletb.2019.02.013.

URL https://www.sciencedirect.com/science/article/pii/S0370269319301066

[47] A. Anirban, Precise measurement of neutron lifetime, Nature Reviews Physics 4 (1) (2021) 9–9. doi:10.1038/s42254-021-00414-2.
URL https://doi.org/10.1038/s42254-021-00414-2

[48] J. Kahlenberg, D. Ries, K. U. Ross, C. Siemensen, M. Beck, C. Geppert, W. Heil, N. Hild, J. Karch, S. Karpuk, F. Kories, M. Kretschmer, B. Lauss, T. Reich, Y. Sobolev, N. Trautmann, Upgrade of the ultracold neutron source at the pulsed reactor TRIGA mainz, The European Physical Journal A 53 (11) (Nov. 2017). doi:10.1140/epja/i2017-12428-9.
URL https://doi.org/10.1140/epja/i2017-12428-9

[49] W. Wei, A new neutron lifetime experiment with cold neutron beam decay in superfluid helium-4, Journal of Physics G: Nuclear and Particle Physics 47 (12) (2020) 125101. doi:10.1088/1361-6471/abacdb.
URL https://dx.doi.org/10.1088/1361-6471/abacdb

[50] W. Wilburn, J. Bowman, G. Mitchell, J. O'Donnell, S. Penttila, P. Seo, J. Calarco, F. Hersmann, T. Chupp, T. Cianciolo, K. Rykaczewski, G. Young, R. D. Souza, W. Snow, D. Desai, G. Greene, R. Grzywacz, E. Frlez, D. Pocanic, T. Gentile, V. Gudkov, G. Jones, Measurement of neutron decay parameters - the abBA experiment, Journal of Research of the National Institute of Standards and Technology 110 (4) (2005) 389. doi:10.6028/jres.110.058.
URL https://doi.org/10.6028/jres.110.058

[51] J. D. Jackson, Classical Electrodynamics, 3rd Edition, John Wiley & Sons, Nashville, TN, 1998.

[52] B. Lehnert, Dynamics of charged particles, 1964.

[53] F. Gluck, AXISYMMETRIC MAGNETIC FIELD CALCULATION WITH ZONAL HARMONIC EXPANSION, Progress In Electromagnetics Research B 32 (2011) 351–388. doi:10.2528/pierb11042108.
URL https://doi.org/10.2528/pierb11042108

[54] F. Glück, (forthe KATRIN Collaboration), Em field, tracking and scattering simulations for the katrin experiment, Journal of Physics: Conference Series 410 (1) (2013) 012039. doi:10.1088/1742-6596/410/1/012039.
URL https://dx.doi.org/10.1088/1742-6596/410/1/012039

[55] M. T. Robinson, The binary collision approximation: Background and introduction, Radiation Effects and Defects in Solids null (1)

(1994) 3–20. arXiv:https://doi.org/10.1080/10420159408219767, doi:10.1080/10420159408219767.
URL https://doi.org/10.1080/10420159408219767

[56] G. Hobler, G. Betz, On the useful range of application of molecular dynamics simulations in the recoil interaction approximation, Nuclear Instruments and Methods in Physics Research Section B: Beam Interactions with Materials and Atoms 180 (1) (2001) 203–208, computer Simulation of Radiation Effects in Solids. doi:10.1016/S0168-583X(01)00418-9.
URL https://www.sciencedirect.com/science/article/pii/S0168583X01004189

[57] The cloud infrastructure platform (CLIP), http://www.clip.science, last visited 2022-01-11.

[58] R. Jiglau, Simulation and design of the high voltage post-acceleration electrode for NoMoS, Master's thesis, Universität Wien (2020).

[59] D. Dubbers, H. Abele, S. Baeßler, B. Märkisch, M. Schumann, T. Soldner, O. Zimmer, A clean, bright, and versatile source of neutron decay products, Nuclear Instruments and Methods in Physics Research Section A: Accelerators, Spectrometers, Detectors and Associated Equipment 596 (2) (2008) 238–247. doi:https://doi.org/10.1016/j.nima.2008.07.157.
URL https://www.sciencedirect.com/science/article/pii/S0168900208011285

[60] G. Konrad, H. Abele, M. Beck, C. Drescher, D. Dubbers, J. Erhart, H. Fillunger, C. Gösselsberger, W. Heil, M. Horvath, E. Jericha, C. Klauser, J. Klenke, B. Märkisch, R. K. Maix, H. Mest, S. Nowak, N. Rebrova, C. Roick, C. Sauerzopf, U. Schmidt, T. Soldner, X. Wang, O. Zimmer, T. P. collaboration, Neutron decay with perc: a progress report, Journal of Physics: Conference Series 340 (1) (2012) 012048. doi:10.1088/1742-6596/340/1/012048.
URL https://dx.doi.org/10.1088/1742-6596/340/1/012048

[61] X. Wang, C. Ziener, H. Abele, S. Bodmaier, D. Dubbers, J. Erhart, A. Hollering, E. Jericha, J. Klenke, H. Fillunger, W. Heil, C. Klauser, G. Konrad, M. Lamparth, T. Lauer, M. Klopf, R. Maix, B. Märkisch, W. Mach, H. Mest, D. Moser, A. Pethoukov, L. Raffelt, N. Rebrova, C. Roick, H. Saul, U. Schmidt, T. Soldner, R. Virot, O. Z. and, Design of the magnet system of the neutron decay facility PERC, EPJ Web of Conferences 219 (2019) 04007. doi:10.1051/epjconf/201921904007.
URL https://doi.org/10.1051/epjconf/201921904007

[62] ILL, Institute laue-langevin homepage, `www.ill.eu`, [Online; Accessed: 13.12.16] (2016).

[63] H. Abele, D. Dubbers, H. Häse, M. Klein, A. Knöpfler, M. Kreuz, T. Lauer, B. Märkisch, D. Mund, V. Nesvizhevsky, A. Petoukhov, C. Schmidt, M. Schumann, T. Soldner, Characterization of a ballistic supermirror neutron guide, Nuclear Instruments and Methods in Physics Research Section A: Accelerators, Spectrometers, Detectors and Associated Equipment 562 (1) (2006) 407–417. doi:https://doi.org/10.1016/j.nima.2006.03.020.
URL `https://www.sciencedirect.com/science/article/pii/S0168900206005328`

[64] M. Berger, J. Coursey, M. Zucker, J. Chang, S. Seltzer, P. Bergstrom, Stopping-powers and range tables for electrons, protons, and helium ions, nist standard reference database 124 (last visited 2023-06-20). doi:10.18434/T4NC7P.
URL `http://www.nist.gov/pml/data/star/index.cfm`

[65] Universite de Sherbrooke, Casino.
URL `https://www.gegi.usherbrooke.ca/casino/download.html`

[66] J. F. Ziegler, J. P Biersack, M. D. Ziegler, Srim - the stopping and range of ions in matter (2013).
URL `http://www.srim.org`

[67] Markus Fuchs, Backscattering of Protons on Detector Materials for the R×B Spectrometer NoMoS, Bachelor Thesis, Universität Wien (2019).

[68] F. Wietfeldt, C. Trull, R. Anderman, F. Bateman, M. Dewey, A. Komives, A. Thompson, S. Balashov, Y. Mostovoy, A backscatter-suppressed beta spectrometer for neutron decay studies, Nuclear Instruments and Methods in Physics Research Section A: Accelerators, Spectrometers, Detectors and Associated Equipment 538 (1) (2005) 574–591. doi:https://doi.org/10.1016/j.nima.2004.08.123.
URL `https://www.sciencedirect.com/science/article/pii/S0168900204020650`

[69] D. Dubbers, L. Raffelt, F. Friedl, B. Märkisch, H. Abele, The point spread function of electrons in a magnetic field, and the decay of the free neutron, Nucl. Instrum. Meth. A 763 (2014) 112–119. arXiv:0812.0347, doi:10.1016/j.nima.2014.06.020.

[70] K. Fehre, D. Trojanowskaja, J. Gatzke, M. Kunitski, F. Trinter, S. Zellser, L. P. H. Schmidt, J. Stohner, R. Berger, A. Czasch, O. Jagutzki, T. Jahnke,

R. Dörner, M. S. Schöffler, Absolute ion detection efficiencies of microchannel plates and funnel microchannel plates for multi-coincidence detection, Review of Scientific Instruments 89 (4) (2018) 045112. doi:10.1063/1.5022564.
URL `https://doi.org/10.1063/1.5022564`

[71] D. Alumot, E. Kroupp, A. Fisher, Examination of the spatial-response uniformity of a microchannel-plate detector using a pulsed high-voltage electron gun, Journal of Instrumentation 9 (05) (2014) P05004. doi:10.1088/1748-0221/9/05/P05004.
URL `https://dx.doi.org/10.1088/1748-0221/9/05/P05004`

[72] W. Leo, Techniques for Nuclear and Particle Physics Experiments : a How-to Approach, Springer, Berlin, Heidelberg, 1994.

[73] J. Kemmer, G. Lutz, New detector concepts, Nucl. Instr. Meth. A 253 (3) (1987) 365–377. doi:10.1016/0168-9002(87)90518-3.

[74] P. Lechner, The Halbleiterlabor of the Max Planck Society, Munich, Germany, private communication (2019).

[75] G. Hobler, Monte Carlo simulation of two-dimensional implanted dopant distributions at mask edges, Nucl. Instr. Meth. B 96 (1995) 155–162. doi:10.1016/0168-583X(94)00476-5.

[76] G. Hobler, K. Bourdelle, K. T. Akatsu, Random and channeling stopping power of H in Si below 100 keV, Nucl. Instr. Meth. B 242 (2006) 617–619.

[77] L. Broussard, B. Zeck, E. Adamek, S. Baeßler, N. Birge, M. Blatnik, J. Bowman, A. Brandt, M. Brown, J. Burkhart, N. Callahan, S. Clayton, C. Crawford, C. Cude-Woods, S. Currie, E. Dees, X. Ding, N. Fomin, E. Frlez, J. Fry, F. Gray, S. Hasan, K. Hickerson, J. Hoagland, A. Holley, T. Ito, A. Klein, H. Li, C.-Y. Liu, M. Makela, P. McGaughey, J. Mirabal-Martinez, C. Morris, J. Ortiz, R. Pattie, S. Penttilä, B. Plaster, D. Počanić, J. Ramsey, A. Salas-Bacci, D. Salvat, A. Saunders, S. Seestrom, S. Sjue, A. Sprow, Z. Tang, R. Vogelaar, B. Vorndick, Z. Wang, W. Wei, J. Wexler, W. Wilburn, T. Womack, A. Young, Detection system for neutron β decay correlations in the UCNB and Nab experiments, Nucl. Instr. Meth. A 849 (2017) 83–93. doi:10.1016/j.nima.2016.12.030.

[78] S. Ramo, Currents induced by electron motion, Proceedings of the IRE 27 (9) (1939) 584–585. doi:10.1109/JRPROC.1939.228757.

[79] G. Pellegrini, M. Baselga, M. Carulla, V. Fadeyev, P. Fernández-Martínez, M. García, D. Flores, Z. Galloway, C. Gallrapp, S. Hidalgo, Z. Liang, A. Merlos, M. Moll, D. Quirion, H. Sadrozinski, M. Stricker, I. Vila, Recent technological

developments on LGAD and iLGAD detectors for tracking and timing applications, Nucl. Instr. Meth. A 831 (2016) 24–28. doi:10.1016/j.nima.2016.05.066.

[80] G.-F. Dalla Betta, L. Pancheri, M. Boscardin, G. Paternoster, C. Piemonte, N. Cartiglia, F. Cenna, M. Bruzzi, Design and TCAD simulation of double-sided pixelated low gain avalanche detectors, Nucl. Instr. Meth. A 796 (04 2015). doi:10.1016/j.nima.2015.03.039.

[81] Synopsys TCAD, Sentaurus workbench, `https://www.synopsys.com/silicon/tcad.html` (last visited 2022-1-11).

[82] A. Doblas, W. Khalid, D. Flores, S. Hidalgo, G. Pellegrini, M. Valentan, Proton Low Gain Avalanche Detector (pLGAD) for low energy particles detection, in: 2021 13th Spanish Conference on Electron Devices (CDE), 2021, pp. 137–140. doi:10.1109/CDE52135.2021.9455752.

[83] W. Khalid, M. Valentan, A. Doblas, D. Flores, S. Hidalgo, G. Konrad, J. Marton, N. Moffat, D. Moser, S. Onder, G. Pellegrini, J. Villegas, First results for the plgad sensor for low-penetrating particles, Nuclear Instruments and Methods in Physics Research Section A: Accelerators, Spectrometers, Detectors and Associated Equipment 1040 (2022) 167220. doi:https://doi.org/10.1016/j.nima.2022.167220.
URL `https://www.sciencedirect.com/science/article/pii/S0168900222005757`

[84] CIVIDEC Instrumentation, TCT AMPLIFIER (2022).
URL `https://cividec.at/index.php?module=public.product&idProduct=35&scr=0`

[85] M. A. Green, Self-consistent optical parameters of intrinsic silicon at 300k including temperature coefficients, Solar Energy Materials and Solar Cells 92 (11) (2008) 1305–1310. doi:https://doi.org/10.1016/j.solmat.2008.06.009.
URL `https://www.sciencedirect.com/science/article/pii/S0927024808002158`

[86] R. Mulargia, R. Arcidiacono, A. Bellora, M. Boscardin, N. Cartiglia, F. Cenna, R. Cirio, G. D. Betta, S. Durando, A. Fadavi, M. Ferrero, Z. Galloway, B. Gruey, P. Freeman, G. Kramberger, I. Mandic, V. Monaco, M. Obertino, L. Pancheri, G. Paternoster, F. Ravera, R. Sacchi, H. Sadrozinski, A. Seiden, V. Sola, N. Spencer, A. Staiano, M. Wilder, N. Woods, A. Zatserklyaniy, Temperature dependence of the response of ultra fast silicon detectors, Journal of Instrumentation 11 (12) (2016) C12013. doi:10.1088/1748-0221/11/12/C12013.
URL `https://dx.doi.org/10.1088/1748-0221/11/12/C12013`

[87] J. Zhang, R. Barten, F. Baruffaldi, A. Bergamaschi, G. Borghi, M. Boscardin, M. Brückner, M. Carulla, M. C. Vignali, R. Dinapoli, S. Ebner, F. Ficorella, E. Fröjj¨dh, D. Greiffenberg, O. H. Ali, J. Heymes, S. Hasanaj, V. Hinger, T. King, P. Kozlowski, C. Lopez-Cuenca, D. Mezza, K. Moustakas, A. Mozzanica, G. Paternoster, S. Ronchin, C. Ruder, B. Schmitt, D. Thattil, Development of lgad sensors with a thin entrance window for soft x-ray detection, Journal of Instrumentation 17 (11) (2022) C11011. doi:10.1088/1748-0221/17/11/C11011. URL `https://dx.doi.org/10.1088/1748-0221/17/11/C11011`

[88] R. Padilla, C. Labitan, Z. Galloway, C. Gee, S. Mazza, F. McKinney-Martinez, H.-W. Sadrozinski, A. Seiden, B. Schumm, M. Wilder, Y. Zhao, H. Ren, Y. Jin, M. Lockerby, V. Cindro, G. Kramberger, I. Mandiz, M. Mikuz, M. Zavrtanik, R. Arcidiacono, N. Cartiglia, M. Ferrero, M. Mandurrino, V. Sola, A. Staiano, Effect of deep gain layer and carbon infusion on lgad radiation hardness, Journal of Instrumentation 15 (10) (2020) P10003. doi:10.1088/1748-0221/15/10/P10003. URL `https://dx.doi.org/10.1088/1748-0221/15/10/P10003`

[89] S. Ayyoub, C. Gee, R. Islam, S. M. Mazza, B. Schumm, A. Seiden, Y. Zhao, A new approach to achieving high granularity for silicon diode detectors with impact ionization gain (2021). doi:10.48550/ARXIV.2101.00511. URL `https://arxiv.org/abs/2101.00511`

[90] F. Cenna, N. Cartiglia, M. Friedl, B. Kolbinger, H.-W. Sadrozinski, A. Seiden, A. Zatserklyaniy, A. Zatserklyaniy, Weightfield2: A fast simulator for silicon and diamond solid state detector, Nucl. Instr. Meth. A 796 (2015) 149–153. doi:10.1016/j.nima.2015.04.015.

[91] S. Onder, Characterization and Simulation of the Proton Low Gain Avalanche Detector (pLGAD) with Weightfield2, Bachelor Thesis, Universität Wien (2020).

[92] T. Bergauer, Design, construction and commissioning of the CMS tracker at CERN and proposed improvements for detectors at the future International Linear Collider, Ph.D. thesis, TU Wien (2008). URL `https://s3.cern.ch/inspire-prod-files-2/290b2b32c9bcd7b9a7bf9e1f3c50c469`

[93] Alibava Systems, The AliVata readout system (last visited 2022-01-11). URL `http://www.alibavasystems.com/products-alibava-systems/research-instruments-alibava-systems/alivata-system.html`

[94] Medipix Collaboration, The Timepix3 chip (last visited 2022-01-11). URL `https://medipix.web.cern.ch/technology-chip/timepix3-chip`

[95] T. Poikela, J. Plosila, T. Westerlund, M. Campbell, M. D. Gaspari, X. Llopart, V. Gromov, R. Kluit, M. van Beuzekom, F. Zappon, V. Zivkovic, C. Brezina, K. Desch, Y. Fu, A. Kruth, Timepix3: a 65k channel hybrid pixel readout chip with simultaneous ToA/ToT and sparse readout, Journal of Instrumentation 9 (05) (2014) C05013–C05013. doi:10.1088/1748-0221/9/05/c05013.

[96] M. Simson, Measurement of the electron antineutrino angular correlation coefficient a with the neutron decay spectrometer aspect, Ph.D. thesis, The Technical University of Munich (9 2010).

[97] A. Bähr, H. Kluck, J. Ninkovic, J. Schieck, J. Treis, Depfet detectors for direct detection of mev dark matter particles, The European Physical Journal C 77 (06 2017). doi:10.1140/epjc/s10052-017-5474-5.

[98] M. J. Bales, R. Alarcon, C. D. Bass, E. J. Beise, H. Breuer, J. Byrne, T. E. Chupp, K. J. Coakley, R. L. Cooper, M. S. Dewey, S. Gardner, T. R. Gentile, D. He, H. P. Mumm, J. S. Nico, B. O'Neill, A. K. Thompson, F. E. Wietfeldt, Precision measurement of the radiative β decay of the free neutron, Phys. Rev. Lett. 116 (2016) 242501. doi:10.1103/PhysRevLett.116.242501.
URL `https://link.aps.org/doi/10.1103/PhysRevLett.116.242501`

[99] J. F. Ziegler, M. Ziegler, J. Biersack, SRIM – The stopping and range of ions in matter (2010), Nucl. Instr. Meth. B 268 (11) (2010) 1818–1823, 19th International Conference on Ion Beam Analysis. doi:https://doi.org/10.1016/j.nimb.2010.02.091.
URL `http://www.sciencedirect.com/science/article/pii/S0168583X10001862`

[100] J. Ziegler, SRIM - The Stopping and Range of Ions in Matter (last visited 2020-05-06).
URL `http://www.srim.org/`

[101] A. T. Yue, M. S. Dewey, D. M. Gilliam, G. L. Greene, A. B. Laptev, J. S. Nico, W. M. Snow, F. E. Wietfeldt, Improved determination of the neutron lifetime, Phys. Rev. Lett. 111 (2013) 222501. doi:10.1103/PhysRevLett.111.222501.
URL `https://link.aps.org/doi/10.1103/PhysRevLett.111.222501`

[102] J. A. Hinks, F. Hibberd, K. Hattar, A. Ilinov, D. C. Bufford, F. Djurabekova, G. Greaves, A. Kuronen, S. E. Donnelly, K. Nordlund, Effects of crystallographic and geometric orientation on ion beam sputtering of gold nanorods, Scientific Reports 8 (1) (2018) 512. doi:10.1038/s41598-017-17424-9.
URL `https://www.nature.com/articles/s41598-017-17424-9`

[103] K. Schlueter, K. Nordlund, G. Hobler, M. Balden, F. Granberg, O. Flinck, T. F. da Silva, R. Neu, Absence of a crystal direction regime in which sputtering corresponds to amorphous material, Phys. Rev. Lett. 125 (2020) 225502. doi:10.1103/PhysRevLett.125.225502.
URL https://link.aps.org/doi/10.1103/PhysRevLett.125.225502

[104] M.L. Swanson, Channeling, in: Handbook of Modern Ion Beam Analysis, Materials Research Society, Pittsburgh, PA, 1995, pp. 231–300.

[105] G. Hobler, Critical angles and low-energy limits to ion channeling in silicon, Radiation Effects and Defects in Solids 139 (1) (1996) 21–85. arXiv:https://doi.org/10.1080/10420159608212927, doi:10.1080/10420159608212927.
URL https://doi.org/10.1080/10420159608212927

[106] D. S. Gemmell, Channeling and related effects in the motion of charged particles through crystals, Rev. Mod. Phys. 46 (1974) 129–227. doi:10.1103/RevModPhys.46.129.
URL https://link.aps.org/doi/10.1103/RevModPhys.46.129

[107] B. Simkin, M. Crimp, An experimentally convenient configuration for electron channeling contrast imaging, Ultramicroscopy 77 (1) (1999) 65–75. doi:https://doi.org/10.1016/S0304-3991(99)00009-1.
URL https://www.sciencedirect.com/science/article/pii/S0304399199000091

[108] K. Kimura, M. Mannami, Dechanneling of electrons at dislocations, Nuclear Instruments and Methods in Physics Research Section B: Beam Interactions with Materials and Atoms 48 (1) (1990) 197–199. doi:https://doi.org/10.1016/0168-583X(90)90103-2.
URL https://www.sciencedirect.com/science/article/pii/0168583X90901032

[109] G. Hobler, K. Nordlund, Channeling maps for Si ions in Si: Assessing the binary collision approximation, Nuclear Instruments and Methods in Physics Research Section B: Beam Interactions with Materials and Atoms 449 (2019) 17–21. doi:https://doi.org/10.1016/j.nimb.2019.04.029.
URL http://www.sciencedirect.com/science/article/pii/S0168583X19302137

[110] A. Simionescu, G. Hobler, S. Bogen, L. Frey, H. Ryssel, Model for the electronic stopping of channeled ions in silicon around the stopping power maximum,

Nuclear Instruments and Methods in Physics Research Section B: Beam Interactions with Materials and Atoms 106 (1) (1995) 47–50, ion Beam Modification of Materials. doi:https://doi.org/10.1016/0168-583X(95)00676-1.
URL http://www.sciencedirect.com/science/article/pii/0168583X95006761

[111] G. Hobler, K. Bourdelle, T. Akatsu, Random and channeling stopping power of h in si below 100kev, Nuclear Instruments and Methods in Physics Research Section B: Beam Interactions with Materials and Atoms 242 (1) (2006) 617–619, ion Beam Modification of Materials. doi:https://doi.org/10.1016/j.nimb.2005.08.181.
URL http://www.sciencedirect.com/science/article/pii/S0168583X05016162

[112] J. Lindhard, On the properties of a gas of charged particles, Kgl. Danske Videnskab. Selskab Mat.-fys. Medd. Vol: 28, No. 8 (1 1954).
URL https://www.osti.gov/biblio/4405425

[113] J. Lindhard, M. Scharff, Energy dissipation by ions in the kev region, Phys. Rev. 124 (1961) 128–130. doi:10.1103/PhysRev.124.128.
URL https://link.aps.org/doi/10.1103/PhysRev.124.128

[114] M. Berger, J. Coursey, M. Zucker, J. Chang, Estar, pstar, and astar: Computer programs for calculating stopping-power and range tables for electrons, protons, and helium ions (version 1.2.3), [Online], Available: http://physics.nist.gov/Star[2020,04,10] (2005).

[115] K. Nordlund, F. Djurabekova, G. Hobler, Large fraction of crystal directions leads to ion channeling, Phys. Rev. B 94 (2016) 214109. doi:10.1103/PhysRevB.94.214109.
URL https://link.aps.org/doi/10.1103/PhysRevB.94.214109

[116] B. Collett, F. Bateman, W. K. Bauder, J. Byrne, W. A. Byron, W. Chen, G. Darius, C. DeAngelis, M. S. Dewey, T. R. Gentile, M. T. Hassan, G. L. Jones, A. Komives, A. Laptev, M. P. Mendenhall, J. S. Nico, G. Noid, H. Park, E. J. Stephenson, I. Stern, K. J. S. Stockton, C. Trull, F. E. Wietfeldt, B. G. Yerozolimsky, aCORN: An experiment to measure the electron-antineutrino correlation coefficient in free neutron decay, Review of Scientific Instruments 88 (8) (2017) 083503. doi:10.1063/1.4996542.
URL https://doi.org/10.1063/1.4996542

[117] J. S. Nico, National Institute of Standards and Technology, USA, private communication (2023).

[118] Recent advances in atomic layer deposition, Chemistry of Materials 28 (7) (2016) 1943–1947. arXiv:https://doi.org/10.1021/acs.chemmater.6b00673, doi:10.1021/acs.chemmater.6b00673.
URL https://doi.org/10.1021/acs.chemmater.6b00673

[119] J. Zhao, X. Liu, Electron microscopic methods (tem, sem and energy dispersal spectroscopy), in: Reference Module in Earth Systems and Environmental Sciences, Elsevier, 2022. doi:https://doi.org/10.1016/B978-0-12-822974-3.00013-6.
URL https://www.sciencedirect.com/science/article/pii/B9780128229743000136

[120] P. Elleaume, O. Chubar, J. Chavanne, Computing 3d magnetic fields from insertion devices, in: Proceedings of the 1997 Particle Accelerator Conference (Cat. No.97CH36167), Vol. 3, 1997, pp. 3509–3511 vol.3. doi:10.1109/PAC.1997.753258.

[121] F. Pitters, N. A. Tehrani, D. Dannheim, A. Fiergolski, D. Hynds, W. Klempt, X. Llopart, M. Munker, A. Nürnberg, S. Spannagel, M. Williams, Time resolution studies of timepix3 assemblies with thin silicon pixel sensors, Journal of Instrumentation 14 (05) (2019) P05022. doi:10.1088/1748-0221/14/05/P05022.
URL https://dx.doi.org/10.1088/1748-0221/14/05/P05022

[122] J. Wüthrich, A. Rubbia, On the depletion behaviour of low-temperature covalently bonded silicon sensor diodes, Journal of Instrumentation 17 (10) (2022) C10015. doi:10.1088/1748-0221/17/10/C10015.
URL https://dx.doi.org/10.1088/1748-0221/17/10/C10015

[123] Jung, Arik S., Sige/si epitaxy and wafer bonding applied to x-ray detectors, Ph.D. thesis (2018). doi:10.3929/ETHZ-B-000275347.
URL http://hdl.handle.net/20.500.11850/275347

[124] C. A. S. Sweden, COMSOL Multiphysics ® (last visited 2023-05-17).
URL http://www.comsol.com/

[125] R. Virot, Development of calibration sources for proton spectroscopy, Ph.D. thesis (07 2017).

Acknowledgements

"If I have seen further, it is by standing on the shoulders of giants."

Issac Newton

This undertaking has been quite a challenge, and time and time again, I was helped to forge a path forward by everyone around me. First and foremost, I would like to thank Karolina Wochocz for her unconditional love, support, and understanding. She was my anchor when I needed one, and kept me going even when I almost gave up. For that, no amount of acknowledgement can ever be enough but this is a start. In the same vein, I would like to thank my mother, and late father for their support throughout my career. I want to say thank you to my direct supervisor Gertrud Konrad as well, who apart from being an amazing mentor and supervisor, helped me see this project through.

I want to thank my university and DKPI supervisor, Johann Marton who encouraged me every step of the way and helped me focus on what mattered the most. I also want to thank Eberhard Widmann and the entire Stefan Meyer Institute for providing me the resources required to finish this dissertation. A special thanks goes out to Johann Zmeskal, and Martin Martischini for helping me do measurements at VERA even though they did not pan out. I also wish to thank Peter, Julia, Fiona, and Carolina for all their help handling the administrative side of things, and planning celebrations within the institute, which were always a welcomed distraction. I also want to thank all of my colleagues, especially but not limited to, Amit, Alina, Marlene, Vicktoria, Andreas, and Markus, who made working at the institution all the more fun.

I want to give a special thanks to Daniel Moser, who not only proof read this thesis but also provided me with interesting discussions, his invaluable advise, and his company on conferences and retreats.

I want to thank Manfred Valentan, Raluca Jiglau, and Sebastian Onder for not only making the working group extremely fun but also for the great memories and interesting discussions.

I wish to thank all my colleagues at IMB-CNM-CSIC who made my 3 months of stay in Barcelona all the more fun. I especially want to thank Giulio Pellegrini, Neil

Moffat, and Jairo Villegas for not only hosting me but also taking the time to teach me. Similarly, I also want to thank my colleagues in Siegen who made my second secondment all the more fun. I especially want to thank Prof. Ivor Fleck, who agreed to my stay with only 2 days of notice. Similarly, I want to thank Kaveh, Arpan, and Amriteya, along with the other PhD students in Siegen for making my stay fun.

Even though I couldn't join N$ab\not\nu$ for a secondment, I nonetheless want to express my gratitude towards Stefan Baeßler who helped shape parts of this thesis, and provided invaluable comments regarding the investigation of channeling effects. Similarly, I want to thank Torsten Soldner as well who provided his insight regarding my investigations many a times. I also want to Gerhard Hobler, who not only provided me with the software IMSIL but also helped me with his valuable insights so I could make appropriate adjustments to the program.

I also want to thank the DKPI, who not only funded my Doctorate studies but also hosted great retreats where I learnt a lot of new things. In that regard, I also want to thank Andreas Ipp, Anthon Rebhan, and the remaining faculty for the brilliant environment for students they managed to create. Likewise, I would also like to thank the CLIP cluster [57] support team, who always answered all my questions and even let me run some simulations as a courtesy after my contract with the SMI had ended.

I want to thank all my friends who helped me with much needed distractions, motivation and provided me with joy throughout my life. I also want to apologize if I missed someone, and want to state that it was not out of malice but rather my own forgetfulness, and I honestly am thankful to you for your kindness.

Finally, I want to thank you dear reader for reading this. Have a wonderful day.